

Comparative Evaluation of Embedded Heating Elements as Electrothermal Ice Protection Systems for Composite Structures

Alexandre Laroche

A thesis
In the Department
Of
Mechanical and Industrial Engineering

Presented in Partial Fulfillment of the Requirements
For the Degree of
Master of Applied Sciences (Mechanical Engineering) at
Concordia University
Montreal, Quebec, Canada

August 2017

©Alexandre Laroche, 2017

CONCORDIA UNIVERSITY

School of Graduate Studies

This is to certify that the thesis prepared

By: Alexandre Laroche

Entitled: Comparative Evaluation of Embedded Heating Elements as Electrothermal
Ice Protection Systems for Composite Structures

and submitted in partial fulfillment of the requirements for the degree of

Master of Applied Sciences

complies with the regulations of the university and meets the accepted standards with respect to originality and quality.

Signed by the final Examining Committee:

Chair

Dr. Ida Karimfazli

Examiner

Dr. Martin Pugh

Examiner

Dr. Fariborz Haghighat

Co-Supervisor

Dr. Ali Dolatabadi

Co-Supervisor

Dr. Suong V. Hoa

Approved by

Chair of Department or Graduate Program Director

2017

Dean of Faculty

Abstract

Comparative Evaluation of Embedded Heating Elements as Electrothermal Ice Protection Systems for Composite Structures

Alexandre Laroche

Since the development of modern aviation, the formation of ice on aerodynamic surfaces has been an important topic of study. It has been most critical in aviation because icing accidents have a high probability of being fatal. In energy production applications, such as wind turbines, blade icing can reduce power production efficiency and increase structural loads. Active ice protection systems have thus been developed using mechanical, thermal, or chemical methods. The thermal method is the only one that can both prevent and remove ice formations. Nowadays, hot air (i.e., bleed air from engines) thermal ice protection is used for commercial aircraft primary structures that are composed of metals. Composite structures are more suited to electrothermal ice protection systems than to hot air technology because bleed air is too hot and can cause structural damage to the composite. Design criteria for electrothermal systems heavily stand or fall on heating elements' properties. Thus, within this work a study was conducted on the thermal efficiency, and temperature uniformity with consideration for manufacturability, availability, and potential impact of physical properties of three different heating element materials: constantan, carbon fiber, and carbon nanotube networks. Tests were performed on flat heater coupons in an icing wind tunnel. Infrared surface temperature measurements and de-icing time measurements revealed that the performance of the different materials did not differ considerably if all were driven by the same nominal power. Rather, the line spacing between the heating elements was the dominant influencing factor.

Acknowledgements

I would like to express great appreciation to the technical and research staff at Concordia University, without whom much of this work would have been impossible. Notably, the efforts of Dr. Iosif Daniel Rosca, Hani Jazaerli, Maria Jose deGrasso, and Navid Sharifi in their assistance during experiments and in the preparation of experimental equipment is greatly appreciated.

I would also like to thank the Natural Sciences and Engineering Research Council, the Fonds de Recherche du Québec Nature et Technologies, Dr. Stephen Yue through the AeroCREATE Competitive Manufacturing for the Aerospace Industry: Technology and Design, Concordia International, and the Concordia University Department of Mechanical and Industrial Engineering for their financial support.

A special thanks is given to Dr. Elmar Bonnacurso and Vittorio Vercillo from Airbus Group Innovations for their efforts, expert advice, much needed encouragement, and overall dedication to helping me complete this thesis. To my family and friends as well for their relentless encouragement. And finally, to my academic supervisors for consistently giving me opportunities to explore the world, dive into the scientific community, giving me the resources to explore my own scientific curiosity, and always challenging me to think of the bigger picture.

Table of Contents

List of Figures	viii
List of Tables	xiii
Abbreviations	xiv
Chapter 1 - Introduction	1
1.1. Motivation	4
1.2. Review of In-Service IPS for Aerodynamic Applications	5
1.2.1. Small A/C	7
1.2.2. Large A/C	11
1.2.3. Wind Turbines	13
1.2.4. R/C	14
1.3. Composite Materials in Icing Conditions	15
1.4. Review of Novel Electrothermal Systems for Composite Structures	18
1.5. Rationale for Proposed Work	21
1.6. Objectives	23
1.7. Thesis Organization	23
Chapter 2 - Materials & Methods	25
2.1. Heater Coupon Design	25

2.1.1.	Governing Heat Transfer Equations	27
2.1.2.	Embedding Material.....	30
2.1.1.	Selection of Three Heating Element Materials.....	32
2.2.	Manufacturing Process.....	40
2.2.1.	Preform Fabrication (I)	42
2.2.2.	Lead Connections (II)	46
2.2.3.	Composite Layup (III)	47
2.2.4.	Sample Finishing (IV).....	50
2.3.	Icing Wind Tunnel Set-Up.....	51
2.3.1.	On-Line Measurement Equipment.....	56
2.3.1.	Icing Conditions.....	61
2.3.2.	De-Icing Test Procedure	62
2.4.	Data Analysis Tools	66
2.4.1.	IR Images Post-Processing	66
2.4.2.	De-Icing Time Measurement	67
2.4.3.	Finite Element Model	69
Chapter 3 -	Results	73
3.1.	Dry Surface Temperature Measurements.....	74
3.1.1.	Line Spacing Effects on Dry Surface Temperature	75

3.1.2.	Heating Element Material Effects on Dry Surface Temperature.....	76
3.1.3.	Dry Surface Temperature Uniformity.....	78
3.2.	De-Icing Time Measurements.....	80
3.2.1.	Line Spacing Effects on De-Icing Time.....	81
3.2.2.	Heating Element Material Effects on De-Icing Time.....	83
3.2.3.	De-Icing Uniformity.....	84
3.3.	Summary of Results.....	86
Chapter 4 - Discussion.....		87
4.1.	Surface Temperature Measurements.....	87
4.2.	De-Icing Time Measurements.....	94
4.3.	Evaluation of Heating Element Materials.....	95
4.3.1.	Thermal Efficiency.....	95
4.3.2.	Temperature Uniformity.....	97
4.3.3.	Comments on Repairability.....	98
4.4.	Recommended Applications.....	99
Chapter 5 - Conclusion and Outlook.....		102
Chapter 6 - Contributions.....		104
Chapter 7 - References.....		107

List of Figures

Figure 1-1: Evolution of coefficient of drag over modern airfoils with respect to time of glaze ice accretion [4]	2
Figure 1-2: Estimated loss of Annual Energy Production (AEP) for a wind turbine with a 22% chord-length thickness of rime ice on its leading edge [5]	3
Figure 1-3: Rime ice left-over on a wing leading edge after de-icing boot (black component) activation [9]	8
Figure 1-4: Hybrid thermal and electromechanical expulsive de-icing system (TMEDS) presented by [11].....	9
Figure 1-5: Weeping wing ice protection system [13].....	10
Figure 1-6: Hybrid mechanical-electrothermal IPS on an A/C propeller [8]	11
Figure 1-7: Example of a hot air IPS concept [8]	12
Figure 1-8: Typical electrothermal laminated system design for commercial A/C [8]	13
Figure 1-9: Manufacturing of flame-sprayed heating element using robot arm [47]	19
Figure 1-10: Carbon fiber heater concepts from (a) 1987 using graphite fibers as a HE in a Glass/epoxy composite and with nickel foil electrical contacts [38], (b) 2013 using single carbon fiber tows as HE in a glass/epoxy composite [42], and (c) 2013 using carbon fiber ribbon as HE in a glass/epoxy composite small scale wind turbine blade [41]	21

Figure 2-1: Schematic of heater coupon with LS as “a” and HE width as “b”with dimensions in mm	26
Figure 2-2: Conduction Shape Factor for isothermal cylinder in the mid-plane of an infinite plane wall for a HE length of 1 meter and varying cylinder diameters; diameters used in [52] are indicated by large circle markers	34
Figure 2-3: CSF calculated based on $L = 1\text{ m}$ $Z = 0.2\text{ mm}$, $D = 0.127\text{ mm}$, and for varying LS, with the CSF per wire and the CSF multiplied by 9 wires, 5 wires and 3 wires respectively	35
Figure 2-4: Microscope image of glass/epoxy/CNT laminate cross-section showing accumulation of CNT at one surface	37
Figure 2-5: Cross-section schematic of glass/epoxy/CNT heater laminate with (a) first successful iteration with conductive surface, and (b) sequence with insulated heater layer and copper wires to conduct electrical current to HE	37
Figure 2-6: Failed attempt at producing Glass/Epoxy/CNT heater with (a) viscous epoxy/CNT mixture, (b) dry fiberglass layers with through-thickness copper wires, and (c) tool-side of the resulting laminate with dry (unwetted) patches	38
Figure 2-7: (a) Microscope image of electrical bridging due to fiber fraying, (b) the macroscopic image, (c) infrared image of bridging element, (d) improved sewing pattern, and (e)infrared image of improved pattern testing [60].....	43
Figure 2-8: Embroidering Style with (a) weaving of HE, and (b) embroidering of HE [61]	44
Figure 2-9: Dry Preform of embroidered heating elements with LS of 1.5mm (top), 3mm (middle), and 6mm (bottom).....	45
Figure 2-10: Cure cycle used for AI-Technology silver two-part epoxy.....	47
Figure 2-11: Vacuum bag layup schematic	48
Figure 2-12: Laminate layup sequence 0/905Glass0HE0/90Glass	49

Figure 2-13: Cure cycle used for wet layup of Epon 862 with Curing Agent W	50
Figure 2-14: Cured composite plates showing three heaters per plate with (left) 3K CF HE backside, (center) Buckypaper HE, and (right)3K CF HE frontside	50
Figure 2-15: Concordia University Icing Wind Tunnel [61]	51
Figure 2-16: Sample holder with sample installed in IWT test section	52
Figure 2-17: Concordia University IWT Spray Control Panel	53
Figure 2-18: Pneumatic and Water Spray System Diagram	54
Figure 2-19: Wind tunnel test section speed calibration showing 15 m/s point	55
Figure 2-20: Schematic of IWT heater surface temperature measurement setup showing angle and distance of camera w.r.t. test section and substrate.....	58
Figure 2-21: Surface temperature measurement setup showing location of sample holder, IR camera, polymer window, and compressed air for fog prevention.....	59
Figure 2-22: De-Icing Set-Up in IWT with (Camera 1) front view camera, (Camera 2) side view camera, (Fog Protection) compressed air, and (Thermocouple) static air temperature sensor.....	60
Figure 2-23: Method of voltage selection based on desired power density and heater resistance	63
Figure 2-24: IR Image of buckypaper heater with Bx1 as the measurement box and Sp1 on the thermocouple inside the test section	66
Figure 2-25: Optical camera images of Set 30 with views (a) Camera 2 at t = 0 seconds, (b) Camera 1 at t = 0 seconds, (c) Camera 2 at t = 6 seconds, (d) Camera 1 at t = 6 seconds, (e) Camera 2 at t = 9 seconds, and (f) Camera 1 at t = 10 seconds	68
Figure 2-26: Schematic of portion of heater used as the simulation domain with glass/epoxy shown in gray and heating elements as blue-filled squares	69

Figure 2-27: Domain used for finite element analysis showing boundary conditions used and location of HE	70
Figure 2-28: Portion of the mesh showing highlighted HE domain and with mesh density of 100 elements / mm	71
Figure 2-29: Typical finite element temperature contour plot of solution.....	72
Figure 3-1: Average Temperature for all samples grouped together	74
Figure 3-2: Average Temperature sorted by LS	75
Figure 3-3: Average Temperature sorted by HE material	76
Figure 3-4: Simulation results for different material position and sizes embedded in glass/epoxy	77
Figure 3-5: Images of energized heaters in IWT with dry wind (15 m/s, -10°C) taken by IR camera	79
Figure 3-6: De-Icing Time for all samples grouped together	80
Figure 3-7: De-Icing Time grouped by LS	81
Figure 3-8: Time-dependant simulation results at different LS; times shown are the time for the minimum surface temperature to reach 4°C	82
Figure 3-9: De-Icing Time vs. electrical power for the three materials used	83
Figure 3-10: Images of heaters with approximately 20% of their original ice formation remaining (vertical dimension of heaters in images is 17 mm)	85
Figure 4-1: Schematic showing the apparent LS as viewed by the IR camera at an angle of 40° relative to the heater surface, and the pixel resolution size in relation to the apparent HE LS	89

Figure 4-2: Effect of pixel discretization on average temperature measurement of 1.5-mm LS heater based on a dimensionless temperature profile from simulation data 90

Figure 4-3: Microscope images of heater cross sections of the 6-mm LS samples with (a) buckypaper, (b) CF 1K, (c) CF 3K, and (d) constantan..... 91

Figure 4-4: Illustration of heater cross-section optical microscope images with (a) HE thickness, (b) HE width, and (Z) distance from HE mid-thickness to surface of laminate 92

Figure 4-5: Comparison of maximum surface temperature from simulation with experimental measurements with respect to the calculated thermal conduction resistance of each HE 93

List of Tables

Table 2-1: Embedding Material Mechanical Properties	31
Table 2-2: Embedding Material Physical Properties	32
Table 2-3: Heating Element Material Physical Properties.....	39
Table 2-4: Heating Element Materials Mechanical Properties	39
Table 2-5: Steps in sample manufacturing.....	41
Table 2-6: Optical camera technical specifications	60
Table 2-7: Experiment Matrix	65
Table 2-8: Infrared Image parameters.....	67
Table 3-1: Test Conditions.....	73
Table 4-1: HE measurements taken from microscope images of heater cross-sections	92
Table 4-2: Estimated cost of HE made from buckypaper, CF, or constantan wire for a heater of 1 m x 1 m	100

Abbreviations

A	Effective surface or cross-sectional area
A_{TS}	Cross-Section Area of test section
A/C	Aircraft
CF	Carbon Fiber
CNT	Carbon Nanotube
CSF	Conduction Shape Factor
ε	Emissivity of a material
GF	Glass Fiber
h	Convective heat transfer coefficient
HE	Heating Element
IPS	Ice Protection System
IR	Infrared
IWT	Icing Wind Tunnel
k	Thermal conductivity of a material

LS	Line Spacing
LWC	Liquid Water Content
MVD	Median Volume Diameter
MWCNT	Multi-Walled Carbon Nanotubes
\dot{Q}_{Total}	Sum of Conduction, Convection and Radiation heat transfer rates
$\dot{Q}_{conduction}$	Heat transfer rate through a medium
$\dot{Q}_{convection}$	Heat transfer rate through motion of a fluid
$\dot{Q}_{radiation}$	Heat transfer rate through electromagnetic waves
R/C	Rotorcraft
ρ_{Water}	Specific Mass of Water
σ	Stefan-Boltzmann constant
$T_{surface}$	Average surface temperature of the substrate, on the surface exposed to icing conditions
T_{air}	Temperature of the air flowing over the heater
$T_{surrounding}$	Average temperature of surfaces surrounding the radiation-emitting surface of the substrate
∇T	Temperature gradient with respect to length
U_{air}	Velocity of Airstream in test section of icing wind tunnel
\dot{V}	Volume Flow Rate

Chapter 1 - Introduction

Ice is the solid phase of water. At atmospheric pressure, it begins to form at 0°C. The phase change occurs gradually. Depending on environmental conditions, like temperature, and on the volume size of the water, ice nucleation growth rate varies considerably. Complete freezing may occur in less than a minute for the case of single water droplets, or may take several hours for the case of a liter of water. Liquid water may also exist at sub-zero temperatures if no ice nucleation takes place. Often this is the case in distilled or deionized water, which is extremely pure and contains very few impurities that act as nucleation sites. The phase change from liquid to solid of supercooled water may occur almost instantly, especially for small volumes. Unlike most other materials, the density of water decreases during the liquid-solid phase change. This behavior can be a nuisance in macroscopic volumes of water, for example, when water-carrying pipes freeze. Expansion has been known to cause pipe failure, or burst, due to excessive outward pressure. On the other hand, freezing of microscopic droplets, although visually unnoticeable and harmless when isolated, could be deadly; such as is sometimes the case for aircraft icing accidents, where gradual ice formation altered the aerodynamic characteristics of the aircraft and led to a stall and impact shortly after.

Liquid water that impacts a surface may freeze by three mechanisms: conduction from a sub-zero surface, convection from surrounding cold air, or because the water was in a supercooled state, in which case it freezes on impact. The first two mechanisms are responsible for ice formations known as *glaze ice*. Glaze ice is transparent, dense, and adheres well to the surface on which it has formed. The reason it has these properties is because of the gradual freezing that occurs. Liquid water has time to fill any voids or gaps on the surface or on already formed ice. Its interfacial strength is high because water that has filled micropores in the surface material

expands, and forms a mechanical grip. When supercooled droplets impact a surface, they freeze nearly instantly. They exist in their supercooled state only when there are no nucleation sites for the liquid-solid phase transition to occur. Impact energy contributes to the initiation of ice nucleation, after which freezing time is seemingly instantaneous. Ice formations due to impacting supercooled droplets is known as *rime ice*. Rime ice is opaque, porous, and less dense than glaze ice because it encloses many microscopic air pockets. The danger rooting from rime ice is that it grows rather quickly and the shape it forms is aerodynamically disadvantageous.

Supercooled water is commonly found in high altitude clouds. Such clouds pose a threat to aircraft (A/C), whose surface upon contact with the droplets act as ice nucleation sites. Ice growth on the surface of certain A/C components may be detrimental. If devices such as pitot tubes become enveloped with ice, they can completely lose their functionality. For example, three fatalities occurred in 2007 due to Pitot tube icing [1]. One of the most severe cases was the Air France Flight 447 which, over the Atlantic Ocean in between Brazil and France in June 2009, resulted in 238 fatalities [2]. Strongly bonded ice shapes change the aerodynamic characteristics of the A/C, reducing its performance margins and could lead to a fatal stall. Figure 1-1 shows how ice accumulation can increase the coefficient of drag over an airfoil. Between 1988 and 2003 NASA conducted a review of A/C accidents and incidents caused by icing encounters [3]. The report shows that 11,218 fatalities occurred from these accidents over the 16-year period.

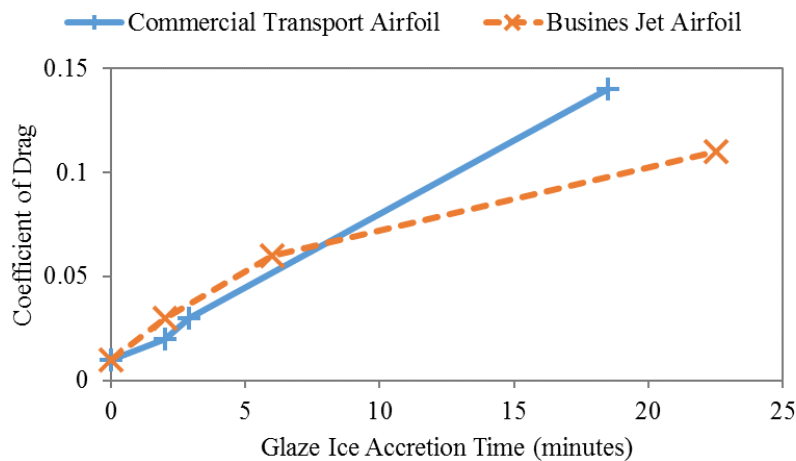


Figure 1-1: Evolution of coefficient of drag over modern airfoils with respect to time of glaze ice accretion [4]

Rotorcraft (R/C) are also affected by icing conditions. It is extremely difficult for a R/C to recover from a stall, unlike fixed-wing A/C which may use the speed gained from lost altitude to regain aerodynamic lift. That is why for R/Cs without any ice protection system (IPS) it is extremely high risk to fly into known icing conditions. For this reason, flight restrictions are extremely severe for R/C without IPS operating in icing conditions.

On the other hand, ice accretion on wind turbine blades is far less likely to lead to fatality. The ice compromises the airfoils' aerodynamics, and causes some loss in efficiency, as estimates show in Figure 1-2. Ice that clings on the surface of turbine blades increases their weight, causing an increase in load on supporting components and the gearbox. Increased loads may reduce the lifetime of these components, which increases the maintenance time and thus reduces the time spent producing electrical power.

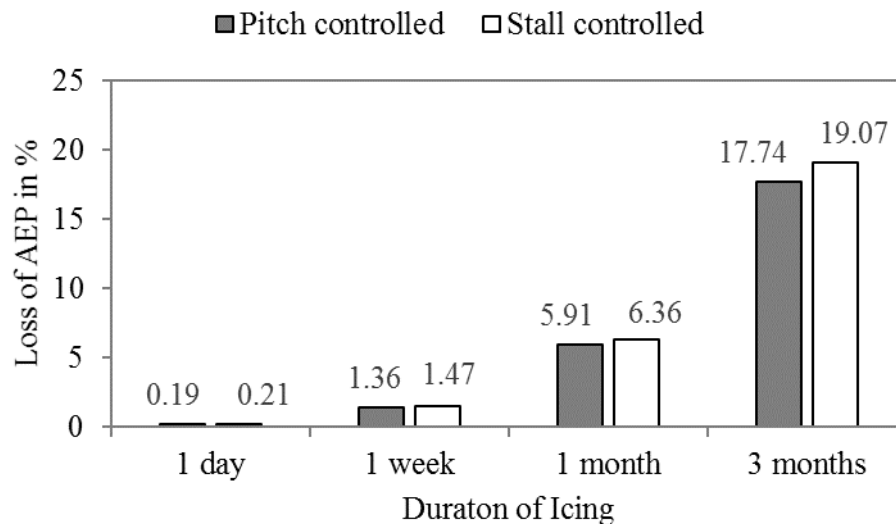


Figure 1-2: Estimated loss of Annual Energy Production (AEP) for a wind turbine with a 22% chord-length thickness of rime ice on its leading edge [5]

1.1. Motivation

The certification process for any A/C is long, expensive and requires many interactions between air framers and certification agencies. It is quite common for A/C equipped with IPS to be certified with IPS but not for flight into known icing conditions. That is, the IPS serves the A/C solely to exit icing conditions safely. Even with a technological safety precaution and a regulatory precaution, incidents can occur whose cause is related to A/C icing.

Even though most A/C accidents are caused by human error, technological advancements generally reduce the number of fatal accidents. Icing encounters are never identical, since ice formations are natural occurrences and their size and shape depend on environmental conditions, A/C size, shape, speed, and angle of attack.

The National Transportation Safety Board (NTSB) and the National Aeronautics and Space Administration (NASA) have surveyed A/C icing incidents over the past few decades [3]. In their report, it was shown that non-scheduled Part 135 operations show the highest percentage of icing accidents to overall incidents. This means that it is most common to have A/C damage or fatalities when icing conditions occur. The relatively small A/C addressed by Part 135 typically carry from four to eight passengers. Most accidents occur due to the pilot's attempt to minimize ice accretion by descending rapidly to a lower altitude, but is hampered by air traffic control requirements.

Meteorological conditions can be forecasted with a certain degree of accuracy. On occasion, however, conditions may change suddenly or information could be incomplete. Sometimes, strict deadlines or other motivating factors may force pilots to attempt to fly through known icing conditions. Human behavior can only be controlled to a certain extent by regulations. It is therefore desirable to develop IPS that are full proof, or that may be certified for flight into known icing conditions. Such systems would reduce any A/C's vulnerability and would help to reduce the urgency felt by pilots to avoid stalling or breaking out of a stall.

Fixed-wing A/C may make a controlled descent to warmer air if ice accretion occurs. The same may not be said of R/C. In laboratory tests of ice-contaminated rotor blades, it has been shown that a loss in lift with constant control collective may reach 15%, as well as a 50% increase in torque [6]. Once R/C blades have stalled, recovery is nearly impossible; especially, because they normally fly at much lower altitude than fixed-wing A/C. Certain operational fields are more susceptible to icing, such as search and rescue, or operations in cold climate. In these cases, it is often necessary to enter into known icing conditions to complete a mission. IPS are mandatory for these R/C.

Energy-producing wind turbines are also located in harsh climates because of the favorable wind. Icing clouds are common in these areas. It is difficult to quantify the effect of ice contamination on wind turbine efficiency because many other influential variables contribute. Power losses between 0.005% and 50% have been reported. Qualitatively, it is known that changes in surface roughness caused by ice contamination will decrease the aerodynamic efficiency of wind turbine blades. Added weight, even if it is symmetric, will cause increased loading on the wind turbine structure and cause pre-mature wear of the gearboxes. Moreover, maintenance workers regularly inspecting the structures have a 1 in 10 chance of being struck by thrown ice released from the rotor blades [7].

In summary, for the above-mentioned aerodynamic applications, icing conditions are at times unavoidable. Technical solutions have been developed since the ice formation problem has first been encountered. The most prominent technical ice protection solutions that are or have been in service are presented in the following section.

1.2. Review of In-Service IPS for Aerodynamic Applications

Today, the primary method of icing prevention is flight planning and icing cloud avoidance. Secondary measures include the use of IPS. Said systems consist of detection and actuation parts. As in most A/C systems, reliability is the most critical aspect considered during icing protection selection.

Ice may be removed mechanically, chemically, or thermally [8]. Mechanical IPS are currently used only for de-icing, i.e. they do not prevent ice formation. Chemical systems refer to de-icing fluids that lower the freezing point of impinging water droplets such that ice cannot form or is melted in case it has already accreted on the A/C structures. Thermal systems have the versatility of either providing anti-icing or de-icing functions. The ice-surface interface is heated and a thin water interlayer thus forms. When the adhesion force of ice slab to the water interlayer is overcome by the aerodynamic drag force, ice is shed off the heated surface.

The FAA has outlined critical A/C components that require icing protection. Primary structures include wing leading edge, engine inlet lips, propellers and spinners, and R/C rotors and hubs. Secondary structures include radomes and antennas, intakes and vents, wing fences, stabilizer mass balance horns, tip tanks, and wheel covers.

Wing leading edges or slats have several options for IPS. The selection of the type of system is mostly influenced by the energy available on the A/C. For example, commercial A/C, with large turbofan engines are almost exclusively equipped with thermal IPS on their wing leading edges. Smaller turboprop A/C often use mechanical low-power systems.

In order to prevent a liquid-solid phase change of impinging water on the surface of a structure, enough heat flux must be supplied to counter that of forced convection occurring over the structure. In order to operate a solid-liquid phase change of, such as is the case for de-icing, an even higher heat flux is required. It is desired to quickly heat the surface to allow shedding the ice instead of gradually melting it. Complete melting takes a longer time and creates a run-back flow of melted water, which will refreeze on unprotected surfaces aft the protected area. Large commercial A/C carry equipment capable of storing and delivering electrical power to satisfy these requirements, but most smaller civil aviation A/C lack this reserve of electrical power.

1.2.1. Small A/C

Propeller-driven A/C simply do not produce the necessary power for purely thermal IPS. Rather, a combination of mechanical, thermal, and sometimes chemical systems is used on certain parts. For example, on the leading edges of propeller blades, an electrothermal heater is commonly used. On the leading edges of large fixed components such as wings, a mechanical or chemical system is used. And on small components such as pitot tubes and carburetors, an electrothermal heater is used.

Mechanical

Mechanical IPS mainly work on destroying the physical bond at the ice-structure interface. The problem is that different icing conditions yield different ice adhesion strengths and bonding mechanisms. Variation in ice adhesion strength is one of the reasons mechanical de-icing systems sometimes do not work as required.

The most common mechanical de-icing system is an inflatable leading edge membrane known as a “boot”. As the boot expands, ice formations fracture suddenly and violently. This system is most commonly found on the leading edge of A/C wings, for example in Figure 1-3, or on the leading edge of propeller blades. The required power consumption is relatively low, since all that is needed is an air compressor for inflation of the membrane [8]. The boot is one of the most efficient systems for smaller A/C, and particularly for those of the size found in FAA Part 135 operations. The drawback of the boot is that significant ice needs to build up before it can be removed. The pilot must decide on when to activate the boot based on visual identification of ice build-up either on the windshield or on the wing, depending on visibility. In addition, ice chunks that are broken off are at risk of being ingested by the engines. If large enough ice chunks find their way into the engine, they may cause what is known as foreign object damage (FOD) – an occurrence even more dangerous than icing. Lastly, the effectiveness of the boot is at the centimeter scale, meaning small residues of ice may remain attached to the wing even after boot actuation. Aerodynamic performance remains somewhat deteriorated in this case leading to a reduced stall speed that may only be estimated by the pilot.



Figure 1-3: Rime ice left-over on a wing leading edge after de-icing boot (black component) activation [9]

Electro-Impulse

When a sizeable ice layer has been formed on the leading edge of an A/C wing, electromagnetic coils are energized. An impulsive force is exerted on the metallic skin, and the sudden deflection expels ice formation from the surface. This system may be used on composite wings as well, since a metallic erosion shield on the leading edge is required anyway. The system requires relatively high current peaks, which may lead to electrical arcing if used improperly. The system is limited to de-icing functions, meaning that a layer of ice must already have formed before it can be operated. In addition, it may not always function to the extent that it needs to – similar to the “boot” IPS. In case of high interfacial strength between ice and surface, a significant amount of ice may stay stuck to the A/C skin [10]. An advantage of impulse de-icing is that it is virtually instantaneous. A hybrid system has also been developed where an electromechanical expulsive de-icing system (EMEDS) was used in conjunction with a heater [11]. This type of thermo-mechanical IPS is undergoing certification procedures with the Federal Aviation Administration (FAA). The schematic in Figure 1-4 helps to visualize the placement of the actuators on the leading edge of an airfoil. A running wet heater is used to weaken the ice/surface bond, and the EMEDS actuators provide the final push to delaminate ice.

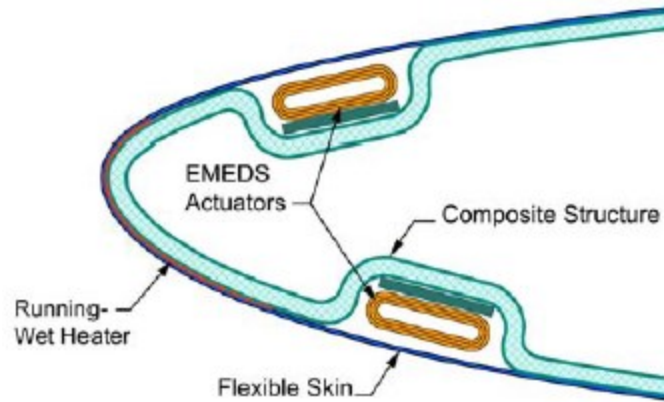


Figure 1-4: Hybrid thermal and electromechanical expulsive de-icing system (TMEDS) presented by [11]

Chemical

Freezing point depressants are chemicals that, when mixed with water, will lower its solid phase transition temperature. Glycol formulas are most commonly used during ground de-icing operations. Prior to take-off, ice is melted and shed from an A/C surface using high-pressure spray of a mixture of water and ethylene glycol. It is the most cost- and time-effective method for ground de-icing to date. A system developed in the second world war consisted of an in-flight chemical de-icing system, which use stored liquid chemicals in the A/C [12]. The chemical seeps out of the A/C's skin and forms a freezing-point-depressant film. A disadvantage of this in-flight icing protection method is the need to repeatedly re-coat the protected surface and refill the de-icing fluid tank. Where the chemical seeps out, complex surface porosities are required, such as shown in Figure 1-5, which raise the cost of maintenance and of A/C materials significantly. In addition, there has been some concern over the release of chemicals into the environment. The advantage of this method is that it consumes very little power.

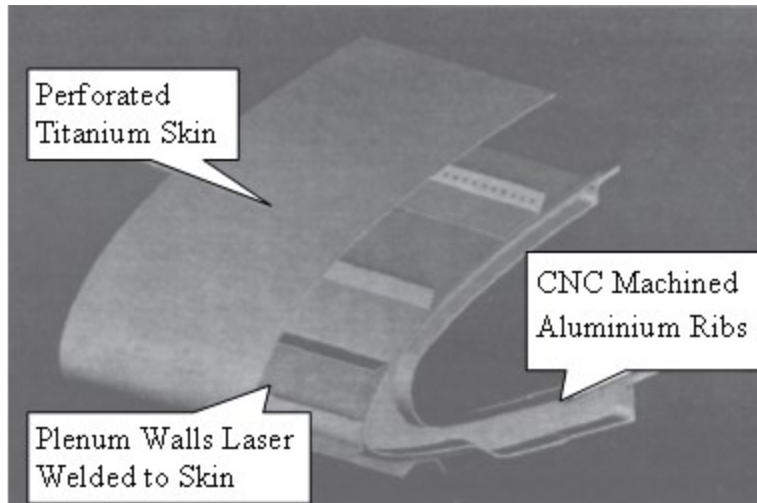


Figure 1-5: Weeping wing ice protection system [13]

Electrothermal

Joule heating devices convert electrical energy into thermal energy via the forced flow of electrons (electrical current) through a resistive medium. Electron mean-free-paths decrease, and the frequency of collisions increases, leading to an increase in particle temperature. Generally, electrical energy may be almost entirely converted into thermal energy (close to 99% efficiency) [14]. Conventional electrothermal IPS consist of a thin metallic heating element laminated between glass fiber sheets and epoxy. The glass fabric and epoxy are used as electrical insulation for the metallic heating element. Figure 1-6 shows a typical hybrid system used on propeller airfoils. A de-icing boot is present for low-power de-icing cycles. The boot's function is complemented by that of the heater, which serves to remove left-over ice, or to act in continuous anti-icing mode.

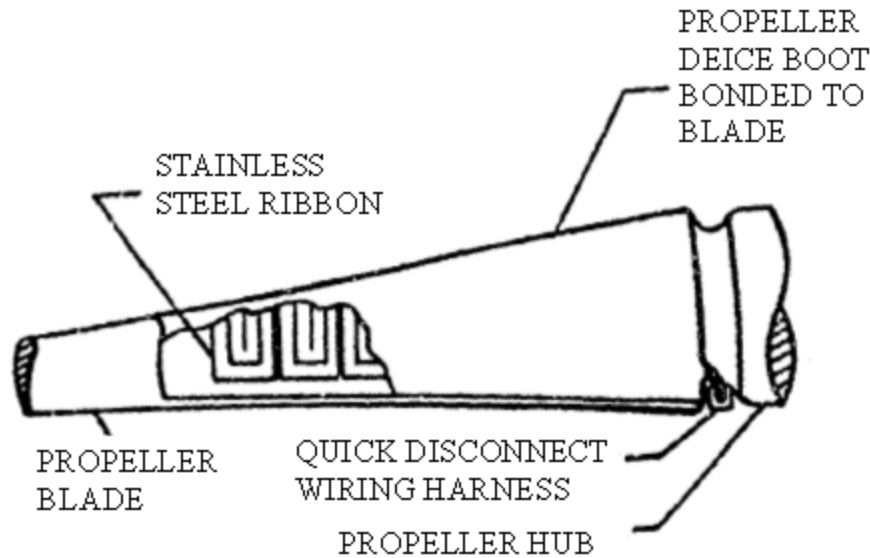


Figure 1-6: Hybrid mechanical-electrothermal IPS on an A/C propeller [8]

1.2.2. Large A/C

The principle of thermal de-icing/anti-icing systems is to cause a local phase change at the interface between ice and substrate using thermal energy. Two possibilities of doing this are to use engine bleed air or Joule heaters.

Engine Bleed Air

Air in the hot section of turbofan engines can reach in excess of 1,000 °C. Even at the exhaust of the engine, the air maintains a temperature on the order of 850 °C [15]. Since engines produce large amounts of hot pressurized air, the natural inclination of A/C system engineers was to use it to heat wing leading edges. In terms of electrical energy, engine bleed-air consumes very little. The extraction of air from the hot section of turbofan engines does, however, greatly decrease their overall performance, which results in greater fuel consumption. Delivery of the hot air to the wing leading edges requires long and complex piping systems with switches and vents. Figure 1-7 shows an example of a leading edge slat cross section equipped with a hot air ice protection system. In larger A/C, the installation and maintenance of these systems is feasible.

However, there is a minimum size for which the system is practical. That is, engine bleed-air is difficult to extract for anti-icing purposes in single-engine A/C, piston A/C, unmanned A/C, and is up to now not feasible for R/C and future all-electric A/C. Even for modern commercial A/C, engine bleed anti-icing systems are ill-advised for the efficiency penalty and because polymer composite structures are not only sensitive to high temperatures (glass transition temperatures around 180 °C), but they are also thermally insulating.

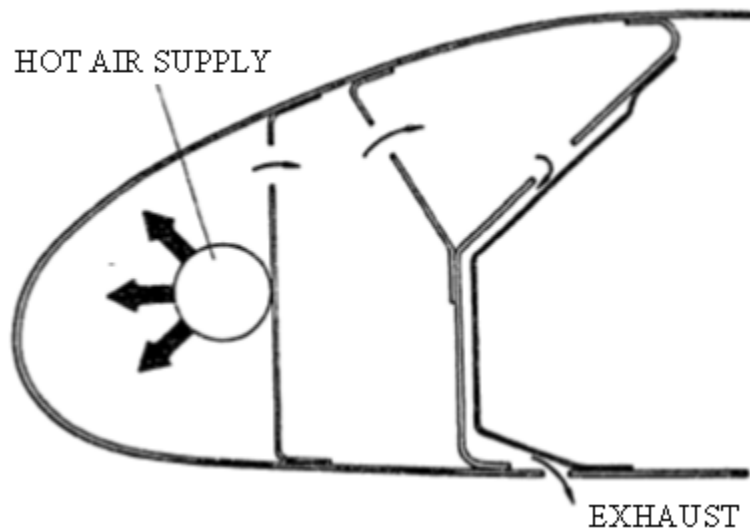


Figure 1-7: Example of a hot air IPS concept [8]

Electrothermal

The Boeing 787 is the only large commercial A/C that has been certified with an electrothermal IPS. The need for such a system stems from the use of fiber reinforced polymer composite materials in some primary structures of the A/C. The advantages and limitations of composite materials is discussed in Section 1.3. In short, composite materials stand lower temperatures than metals and could be easily damaged by a hot bleed-air IPS. The drawback is that composite heaters require electrical insulation and an erosion shield. A typical cross-section of an electrothermal ice protection heater is shown in Figure 1-8.

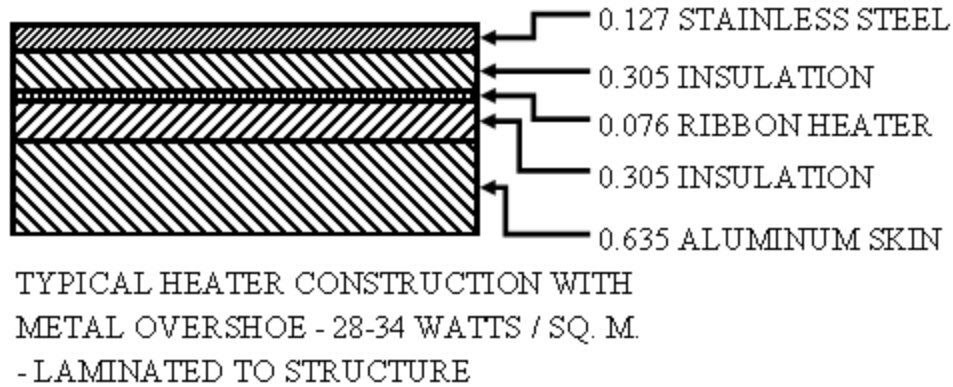


Figure 1-8: Typical electrothermal laminated system design for commercial A/C [8]

1.2.3. Wind Turbines

Current active IPS for wind turbine blades are limited to thermal systems. Chemical systems would require prohibitive amounts of fluids, and vibrational systems have not been implemented yet. Employed thermal systems today are either the flow of hot air within the blade structure or electrothermal heating.

Electrothermal systems in wind turbine blades consume large amounts of electrical energy, especially in continuous anti-icing mode. There is a range of ice accretion thickness that is acceptable for different span regions of the turbine blades. The most critical span area, that is the one where the tolerable ice thickness is the smallest, is at the tip of the blades. On some wind turbine blades, only that critical tip region is heated electrothermally. On others, the electrothermal tip system is complemented by a pneumatic inflating boot between the root and where the electrothermal system begins.

Hot air has also been used as an IPS for wind turbine blades. This system also requires large amounts of electrical energy. The high speeds of the blades result in high convection losses, and much energy is spent to heat the air that flows inside the blades. The low thermal conductivity of the glass/polyester composite structure helps to insulate the inside of the blades, but increases the amount of energy required to heat their outer surface [7].

A self-sufficient passive ice-phobic coating has yet to be developed. Many studies have proposed novel coatings with extraordinary ice repellent properties but they are unable to prevent the formation of ice altogether. They must be accompanied by some sort of active IPS, whose energy consumption would be reduced by the presence of the passive coating.

1.2.4. R/C

The most critical components that require icing protection on R/C are the rotor blades. Blades are commonly made from carbon fiber reinforced epoxy composites. Their shape, weight balance, and internal structure are highly important factors that influence the performance of the R/C. Ice accreted on the leading edges of rotor blades is subject to high centrifugal forces and therefore, high shear stresses at the ice-blade interface. If the shear strength of the interfacial bond is decreased, ice removal can be eased.

Slip rings are used to provide electrical contact between two plates which are spinning at different speeds. These mechanisms are useful in R/C for transporting electrical current into the blades for heating.

Electrothermal IPS for R/C have appeared in five different forms: etched metal foil, sprayed metal grid, knitted metal wire/glass fabric, pierced expanded metal grid, and wires embedded in rubber. The last showed evident failures: extreme wire temperatures would cause charring to the rubber and result in short circuits to blades and the erosion shield. Sprayed metal grids and wires embedded in glass fibers both experienced frequent short-circuits and burnouts during their service life equipped to the CH-46 R/C. These failures have been attributed to failures in the erosion shield. Pierced expanded metal foil showed satisfactory performance, as well as the etched metal grid [16].

Ultrasonic

Vibrations induced in the skin of the A/C wing cause enough shear stress in the ice-wing interface that the ice delaminates [17]. This method is highly sensitive to the adhesion strength

of ice to the wing. Other factors include ice density and ice type, which are also influenced by particle impact speed, temperature, and humidity, among others. The difference in ice adhesion strength between rime ice and glaze ice, for example, is sizeably different. All these factors are a challenge for ultrasonic de-icing systems, which are thus not equally effective in all icing conditions. The limited predictability of this technique means it may not be used as a standalone IPS, but it must be combined with a thermal IPS and help reducing the overall electrical power used for A/C ice protection.

1.3. Composite Materials in Icing Conditions

Composite materials are a heterogeneous composition of two (or more) materials, which are referred to as matrix and reinforcement. The reinforcement component is the primary load carrier while the matrix acts to distribute that load among the reinforcements. Fiber reinforced composites are materials whose reinforcing component have a high length-to-girth aspect ratio. They may be short fibers or long fibers. Long fiber reinforcements may be used to provide directional stiffness and strength to a composite part, while short fibers are often mixed and non-directional, and are used to provide some anisotropic properties. When carbon, glass, or Kevlar fibers are used as reinforcement, the resulting composite typically carries a much more favorable strength-to-weight ratio than bulk metals such as aluminum or steel.

For aerodynamic applications, weight is a critical determinant for required energy input. A/C need less fuel if they carry less mass because they require less lift, and therefore less thrust. Wind turbines blades carry less inertia when their weight is optimized, and move with less wind power. Weight reduction is the primary driver to incorporate polymer composite materials into aerodynamic applications. Other factors include corrosion resistance, electrical and thermal insulation, and fatigue resistance.

Continuous fiber reinforced polymer composite materials are anisotropic by nature. Several layers are stacked and cured in different orientations to give the materials the desired mechanical properties in many directions. The variations of the type of matrix is also virtually limitless. It

has been difficult for the aerospace industry to justify the use of composite materials in primary structures due to certification issues, engineering complexity, or poor warning before failure. Secondary and tertiary structures have long been made of composite materials, however. Many R/C are typically equipped with carbon fiber reinforced polymer rotor blades. Likewise, many small A/C use carbon fiber propeller blades. It is also standard in the wind turbine industry to fabricate blades from glass fiber reinforced polymer.

It is not surprising that in their various outdoor applications, composite materials are subjected to icing conditions. The methods of icing protection mentioned earlier are not necessarily directly transferable between structural materials. Vibrational characteristics differ, as well as erosion resistance and temperature range. One of the conceptually simplest icing protection solutions, to heat the exposed surface, is challenging in composites because of the temperature limitation of their polymer matrix. Fibers themselves are generally stable over a wide temperature range. Carbon fibers are synthesized at over 2000 °C, but may be susceptible to oxidation if kept at 450 °C for an extended time [18]. The softening point of typical boron-containing E-glass fibers is between 830 °C and 860 °C [19]. The reinforcement part of polymer composite materials is capable of tolerating relatively high temperatures. The matrix, however, is the weak point. Epoxies are cured up to temperatures of 200 °C, with their glass transition temperature (T_g) between 10 °C and 20 °C lower than their cure temperature, and their maximum operational temperature approximately 30 °C below that [20]. Polyester-resin matrices, often used in wind turbine blades, begin to chemically dissociate at temperatures above 150 °C [21]. Thermoplastic resins can handle higher temperatures, such as 400 °C for polyimide [22]. The major drawback of fiber reinforced thermoplastic composites is their extraordinarily high viscosity at high temperatures. The wetting of fibers with thermoplastic matrices involves high temperature and pressure press machines. In addition, since thermoplastic material is already polymerized, heat only serves to reduce its viscosity, but it also resets its crystal structure. Thermoplastic materials sometimes have a partial crystalline structure which is dictated by the cooling rate. Processing of thermoplastic composites is associated with high-cost tooling and onerous process control [23]. Since aerospace mainly deals with high part variability and low quantity, the use of thermoplastic composites requires strict justification. The wind turbine industry does not require the added benefits of thermoplastic composites, on the other hand.

As a consequence of their limited operational temperature, thermal IPS need to be carefully designed for composite structures. The hot bleed-air system, for example, is not controllable enough for A/C, and poses risks of overheating the composite structures. For this reason, electrothermal systems are preferred to protect composite structures from icing.

Fiber reinforced polymer composites have been the material of choice for electrothermal IPS long before their use in the new generation of Boeing 787 A/C. In fact, the supplier of the wing IPS for that specific A/C, GKN Aerospace, uses a technology based on a patent filed in 1957 [24]. With several improvements on the original idea, GKN flame sprays a metallic conductor onto a glass-fabric reinforced thermoplastic and laminates it with more layers of glass/polymer [25]. Glass reinforced polymer materials are required in A/C IPS as electrical insulation to the conductive heating element. Numerous patents exist which are variations of laminated heaters [26-36]. Some of them use metallic conductors while others rely on materials like carbon nanotubes or expanded graphite [37]. Carbon fibers have been used as heating elements as well [38-42].

One could certainly work on the optimization of the current flame-spraying process. However, the scarcity of research publications on the specific application means that any independent work done in an academic setting is years behind that currently in use by industry. Flame spray has been shown to be one of the more scalable thermal spray processes. It may be difficult, however, and much like many other thermal spray methods to control the thickness, porosity, micro structure, modulus, and macroscopic shape of the deposited material. Through their experience, inventors have presented solutions to a few of these shortfalls, such as the use of a mask to control the in-plane pattern and to obtain a grid, or the use of post-processing to make the edges of the shape uniform.

Metallic conductors are available as thin film heating elements on polyimide or Kapton sheets. Kapton sheets, however, act as crack initiation sites in polymer composites. Thicker metallic conductor heating elements may also be employed; however, they may be difficult to form to an airfoil shape. If there are kinks and form defects in the metallic heater, they may affect the quality of the laminated structure. Even though IPS are not meant to be structural, structural defects are still undesirable in critical aerospace applications.

One of the most successful uses of advanced materials in an IPS is that of Kelly Aerospace's Thermawing heater [29]. This heater consists of an expanded graphite film that is protected by a polyimide film. Graphene, or expanded graphite, carries many of the desirable properties of carbon nanotube networks such as high thermal diffusivity, and low density. These powerful heaters are so effective that they run the risk of overheating and damaging the underlying wing structure. If properly controlled, however, their temperature response is quick¹. The system is available for general aviation A/C, and normally for single-engine propeller airplanes. Installation requires proper alignment and flattening of the heater, and thus relies on the skills of the technician. Erosion protection shields are normally required for any non-metal IPS with the secondary requirement of lightning protection. The mechanical and dielectric properties of polyimide, though, have been shown to be unstable under prolonged exposure to ultraviolet radiation [43].

1.4. Review of Novel Electrothermal Systems for Composite Structures

It is possible to use a low-temperature thermal spray process, such as flame spray, to coat cured composite parts [44-46]. Flame spray is one of the most economical and easy to use thermal spray processes, requiring the lowest capital equipment costs. It is an uncomplicated system involving fewer safety hazards than other processes such as plasma spray. A flame spray gun may be handled by a human operator. For components measuring on the order of up to 1 meter, a highly skilled operator may produce a uniform coating. This practice is convenient for fabrication of electrothermal IPS because of the resulting porous heating element and without the complications associated with drapability onto double-curved features.

¹ In the example described in [29], under static conditions and with an ice block over their wing-mounted heater, a power density of 10 462 W/m² raised the wing/ice interface temperature from 0°C to 30°C in one minute with a halftime temperature of 23°C.

For larger scale components, it becomes more difficult even for the most skilled operator to produce the same uniformity in the coating [47]. Multi-axis robots may be used to operate the flame spray gun to produce higher quality coatings over larger areas, such as in Figure 1-9. Such a system may be impractical, however, for much larger scales such as on wind turbine blades. Conceptually, the process is the same as on medium scale components, where a robot is placed on a linear track to cover the entire span. On larger scales, the track gets longer and the capital equipment costs increase. It should also be mentioned that precise multi-axis robots can be expensive and, depending on the complexity of the component, their programming is not always trivial.

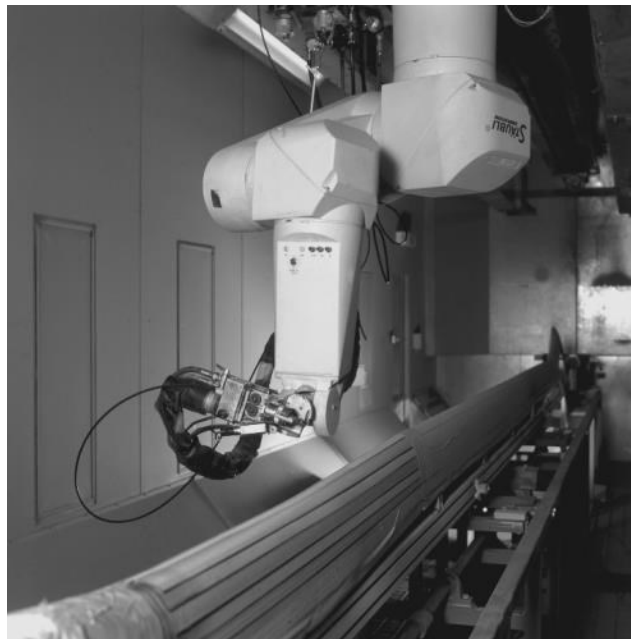


Figure 1-9: Manufacturing of flame-sprayed heating element using robot arm [47]

Like any thermal spray process, several parameters need to be tuned to obtain an optimal result. These parameters, such as standoff distance, torch temperature, overlap of passes, number of passes, speed of travel, spray angle, and others need to be determined empirically. Therefore, the cost of research and process development must also be considered. From the above considerations, the flame spray technique to produce metallic heating elements on cured composite materials would make sense if the set-up costs are leveraged by high quantity demand. Otherwise, in aerospace for example, where part variability is high and part quantity is low,

flame spray may not be the most economical solution. In addition, when bonded to load-bearing aerodynamic structures such as wings, helicopter rotors, and wind turbine blades, fatigue loading of the heating element needs consideration. Under fatigue loading, flame-sprayed coatings have been known to have issues with debonding between the substrate and the coating.

As an alternative to metallic conductors, carbon nanotubes have risen to fame as a sort of revolutionary material and as inherent candidates for any electrical, structural, or thermal applications [37]. Appropriately, carbon nanotube networks have been shown to have low thermal resistance, and may be tailored to have the desired electrical properties. Unfortunately, carbon nanotube heaters have not been taken past the proof-of-concept phase. Many forms of carbon nanotube heaters have been presented but the results have been presented sporadically and without showing intent or parallelism to A/C icing protection applications. Specifically, most studies convolutedly show that some power or power density may raise the temperature of the surface of the heater to some temperature in some amount of time [48]. This data is critical to a proof of concept but it is all specific to lab or experiment conditions which are not representative of the needs of IPS. One potential reason that this material has remained in laboratory settings is because of the relatively high production costs and processing challenges. Challenges include the exponential increase in viscosity when the nanomaterials are added to a liquid polymer matrix, and subsequently the sustain of their uniform dispersion throughout the matrix. Contact resistance is a paramount factor in the use of carbon nanotubes for electrical purposes [49-51]. A common solution is to use a silver-doped epoxy over the carbon nanotube-enhanced structure. Silver epoxy is hardly a scalable solution due its high cost and the need for an independent cure cycle. A post cure may modify the properties of a composite structure if high temperatures are used, and alternately a room-temperature cure would delay production lead-time of the IPS.

Three authors have presented an IPS using carbon fibers as the heating element. Hung et al. showed the heating capability of a graphite fiber fabric in a glass fabric composite (Figure 1-10 (a)), and described many of the challenges in manufacturing and operating the heater [38]. Maheri presented single tows of carbon fibers arranged in a parallel circuit in a 4-layer glass fiber and epoxy laminate (Figure 1-10 (b)) [42]. Chang used a 2-inch woven carbon fiber tape as

the heating element (Figure 1-10 (c)) [41]. The two latter authors found that significant heating occurred on the surface of the laminate but mainly directly in the shadow of the heating element. Chang developed a fuzzy logic controller for the heater and tested it on a small-scale wind turbine rig. Maheri developed a genetic algorithm to determine the optimal position and location of heating elements. All of the carbon fiber heaters mentioned here were simply included in the layup of the composite as an additional layer.

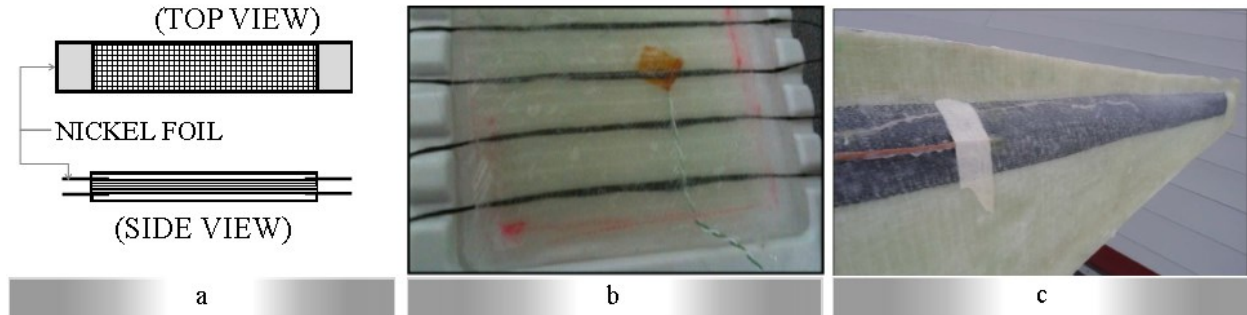


Figure 1-10: Carbon fiber heater concepts from (a) 1987 using graphite fibers as a HE in a Glass/epoxy composite and with nickel foil electrical contacts [38], (b) 2013 using single carbon fiber tows as HE in a glass/epoxy composite [42], and (c) 2013 using carbon fiber ribbon as HE in a glass/epoxy composite small scale wind turbine blade [41]

1.5. Rationale for Proposed Work

Recent research has been based on the development on novel heaters which are more energy efficient than conventional ones. Many studies present the use of novel materials such as carbon nanotube networks or inter-fiber spacing as heating elements that heat faster or with less energy than metals [37, 39, 40]. They have so far neglected to directly compare two different HE materials under the same conditions. The advantage of a direct comparison would be to conclude whether a certain HE material performs better than another and therefore merits some investment for further development. It is the purpose of this thesis to look at different materials as heating elements and to analyze their performance systematically when they are subjected to identical operating conditions. Questions to be answered include: does a certain material yield

superior thermal efficiency or temperature uniformity? And more specifically, is one heating element material more suitable for in-flight ice protection purposes?

In addition, recently developed heaters, and flame sprayed heaters possess challenges with scalability. It is therefore desired to develop a method to manufacture a heater with a well-defined shape using a scalable process. Embroidery of a heating element onto a di-electric medium is one such process. Embroidery of heating elements has been presented in the past for heating of clothing or for use as antennas. It is presented for the first time here as a solution for the fabrication of an IPS.

Textile processes are relatively easily scalable. The repetitiveness of sewing and stitching is such that machines are capable of completing a product at relatively high speed. Using automatic embroidery processes, long heaters may be processed and rolled onto a spool to be unraveled during final IPS fabrication at much lower cost than that of thermal spray.

Quality inspection may also be performed more easily on textile or embroidered heaters than on thermally sprayed heaters. The characterization of thermal spray coatings is a technical and therefore financial challenge in itself. A textile heater may be examined using an optical microscope and, once energized, using an infrared camera. These inspection methods are less costly and less complex than those used for thermal spray coatings.

It is hypothesized that if different HE materials embroidered into a heater are able to achieve the same temperature uniformity and thermal efficiency, then embroidery is a viable technique for the fabrication of electrothermal IPS in composite materials. The other aspects of the heating element materials are therefore of primary importance for the design of electrothermal heaters, and should be considered during electrothermal IPS design without regard for impacts on thermal efficiency or temperature uniformity. Manufacturability, fatigue resistance, and coefficient of thermal expansion are examples of factors outside of heating performance that are heavily influential on material selection of electrothermal IPS. If the anti-hypothesis is correct, that is, if one HE material performs better than the others, then it is the preferred material for embroidered HE. In that case, an investigation into the governing parameters should be done to eventually lead to the selection of an optimal material.

1.6. Objectives

- Develop a standard heater for comparing embroidered heating element materials at coupon scale for small-scale icing wind tunnel testing.²
- Determine if advanced materials, such as carbon nanotube films, show better thermal efficiency as heating elements in composite structures than do conventional metal wires or carbon fiber tows.
- Identify manufacturing challenges of the different heating element materials in their supporting structure and develop mitigating solutions.

1.7. Thesis Organization

This thesis is ordered in the following way:

Chapter 1 – Introduction

The problem of ice accretion is introduced and its impact on aerodynamic structures is discussed. A review of existing ice protection systems that are currently used in-service is presented. This review is followed by a review of novel ice protection systems that are still under development. Justification is given for the work presented in this thesis, and the objectives are listed.

Chapter 2 – Materials and Methods

Based on questions asked in the objective section of the introduction, targeted data is described; input and output variables are identified and selected. Justification and reasoning are provided for the materials used in the study. The test rig is described with details about measurement and

² The term heater is used in this thesis to describe the structure in which a heating element is embedded and which includes a heating element, embedding material such as fiberglass/epoxy, and electrical connectors.

data collection systems. With consideration for the available equipment and their capabilities, ranges for input variables are selected and an experimental matrix is provided. A method of analyzing raw data is detailed.

Chapter 3 – Results

The analyzed data is presented in the form of figures. Mean values with ranges are presented to focus on one input variable at a time. An explanation is provided with each figure to facilitate the reader's comprehension.

Chapter 4 – Discussion

Scientific reasoning is provided here for the results presented in Chapter 3. Some sources of experimental error are identified as input variables that were either uncontrolled or moderately controlled. Some meaning is extracted from the results by extrapolating certain material's use in specific applications mentioned in Chapter 1. The questions asked in Chapter 1 are formally answered.

Chapter 5 – Conclusion and Outlook

The report is summarized here, and attention is given to the meaning of the results. Future studies are proposed.

Chapter 6 – Contributions

A list of useful findings from the results of this thesis is presented here.

Chapter 2 - Materials & Methods

This section will present the design and fabrication of samples, experimental equipment, test procedures, and analysis tools. Details include justification for materials selection, identification of heater manufacturing challenges and development of mitigating solutions, capabilities of equipment, a sample testing matrix, determination of testing conditions, and description of data analysis processes.

2.1. Heater Coupon Design

The design of the heater shape was based on the available testing facility, the Concordia University Icing Wind Tunnel (IWT). The test section has a width and height of 100 mm and is ideal for a cylindrical specimen. Manufacturing of a cylindrical composite heater would merit a study on its own, so a cylindrical sample holder (Figure 2-16) was designed to support a flat composite heater. Past characterisation of the IWT test section revealed that a maximum diameter of 25.4 mm could be tested without significantly disturbing the flow. Thus, the usable area in the test section is roughly 25.4 mm x 100 mm. In order to fit a flat coupon to the leading edge of a 25.4 mm-diameter cylinder, a 17-mm sample height was found to be suitable. The chosen heating element pattern for this rectangular area was a parallel lengthwise grid. If applied to an airfoil, span-wise heating elements provide ice delamination sites. Delamination may propagate chord-wise and remove all ice formations on the airfoil. If chord-wise heating elements are used, then fewer heated portions would remain contaminated due to lack of aerodynamic anchoring for the shedding of ice. Figure 2-1 shows a diagram of the span-wise

heater with the position and size of the embedded HE. Line spacing (LS) was either 1.5 mm, 3 mm, and 6 mm, and the heating element width was dependant on the material format.

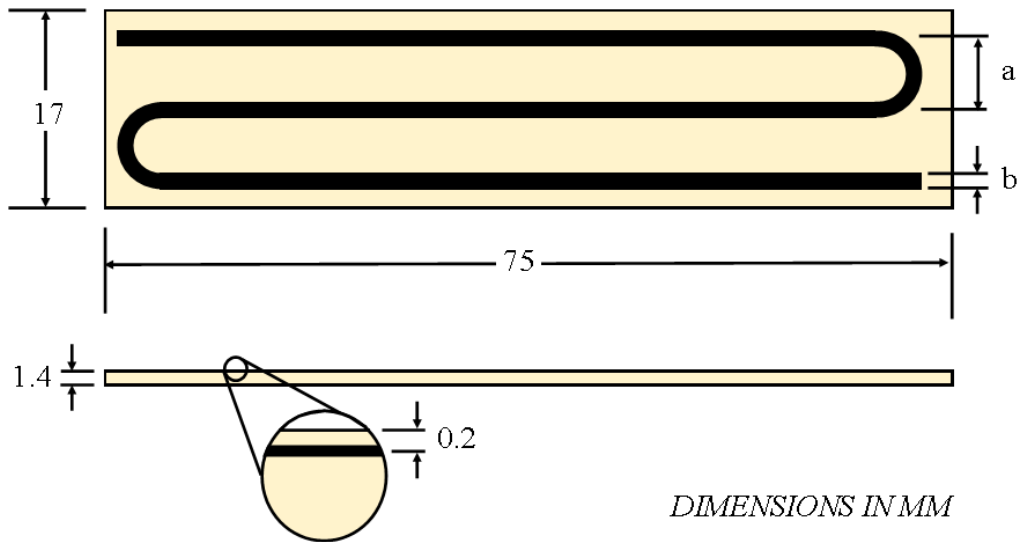


Figure 2-1: Schematic of heater coupon with LS as “a” and HE width as “b” with dimensions in mm

A detailed review of electrothermal IPS for R/C applications, by [16], has identified five types of heating elements currently in service:

1. Etched metal foil grid;
2. Sprayed metal grid;
3. Expanded perforated metal grid;
4. Metal wire embedded in glass/epoxy; and
5. Metal wire embedded in rubber.

The same review provided some criteria for the development of an advanced heater. The criteria emphasized compatibility of mechanical properties of the heating element with the supporting structure. Although that aspect is inarguably important, it has not yet been shown that different heating element materials will yield the same icing protection performance. It would be of interest to compare all types of HE side-by-side, however such a study would be impractical for the following reasons:

- The etched element was not evaluated here because it involves the use of hazardous chemicals and some level of training for the photochemical mask.
- Sprayed metal was not used because of a lack of flame spray equipment and experience, and because the heating element material would be limited to metals.
- Expanded perforated metal grid was not used because of manufacturing complexity.
- Wire embedded in rubber was not evaluated because of its poor performance record and the need for design and fabrication of tooling.
- The wire embedded in glass fabric was the heating element configuration of choice for this study. Specifically, different types of wires (i.e. constantan wires, carbon fiber tows, and buckypaper strips) will be embedded in a glass/epoxy composite.

2.1.1. Governing Heat Transfer Equations

The comparison of the performance of several candidate heating element materials must include their behaviour in the final application, such as in icing conditions, and a more fundamental one such as in dry conditions. The most basic heater test is one where steady-state temperature is monitored versus input power. It is expected that all heating element materials show the same temperature-power response if they are in the same conditions. Equations (2-1)-(2-4) are the heat transfer rate equations for total heat transfer (\dot{Q}_{Total}), heat transfer by conduction ($\dot{Q}_{conduction}$), heat transfer by convection ($\dot{Q}_{convection}$), and heat transfer by radiation ($\dot{Q}_{radiation}$), respectively [52].

$$\dot{Q}_{Total} = \dot{Q}_{conduction} + \dot{Q}_{convection} + \dot{Q}_{radiation} \quad (2-1)$$

$$\dot{Q}_{conduction} = -kA\nabla T \quad (2-2)$$

$$\dot{Q}_{convection} = hA(T_{surface} - T_{air}) \quad (2-3)$$

$$\dot{Q}_{radiation} = \varepsilon\sigma A(T_{surface}^4 - T_{surrounding}^4) \quad (2-4)$$

where k is the thermal conductivity of a solid material (in W/m K), A is the effective cross-sectional area through which heat is passing (in m^2), ∇T is the temperature gradient across a length of material perpendicular to the cross-sectional area (in K/m), h is the coefficient of thermal convection (in W/m²K), T_{surface} is the temperature of the surface exposed to convective heat transfer (in K), T_{air} is the temperature of the surrounding convective airflow (in K), ε is the emissivity of a surface, σ is the Stefan-Boltzmann constant (5.67×10^{-8} W/m²K⁴), and $T_{\text{surrounding}}$ is the surface temperature of a surrounding surface exposed to radiation heat transfer from the surface under study (in K).

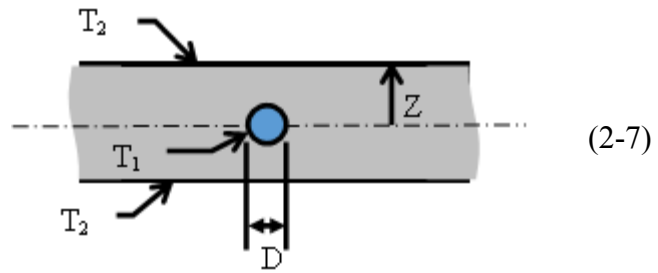
Despite that convection is the dominant heat transfer mechanism in an IPS, conduction heat transfer occurs within the system, and is the main resistance between where energy is input and where it is meant to go – to the protected surface. In embedded-wire electrothermal IPS, the steady-state heat conduction equation can be written as Equation (2-5) and the thermal conduction resistance as Equation (2-6).

$$\dot{Q}_{\text{conduction}} = Sk(T_1 - T_2) \quad (2-5)$$

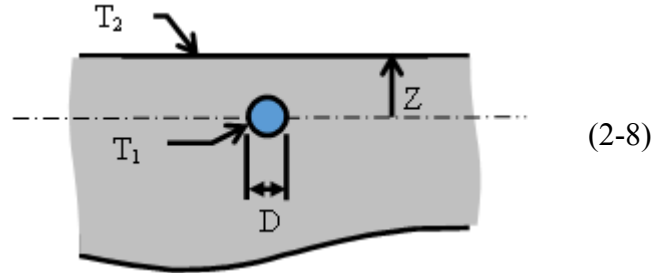
$$R_{\text{thermal}} = \frac{1}{Sk} \quad (2-6)$$

where $\dot{Q}_{\text{conduction}}$ is the conduction heat transfer rate between the wire and the surface of the embedding material, S is known as the conduction shape factor (CSF), k is the thermal conductivity of the embedding material, and R_{thermal} is the thermal conduction resistance defined by the CSF and the thermal conductivity of the material through which conduction heat transfer occurs. R_{thermal} is useful as an electrical analog of the thermal conduction problem and is useful for intuitively understanding one-dimensional heat transfer problems. The CSF has been defined for many conduction scenarios [52]. Those most closely related to electrothermal IPS are written and illustrated in Equations (2-7) through (2-9).

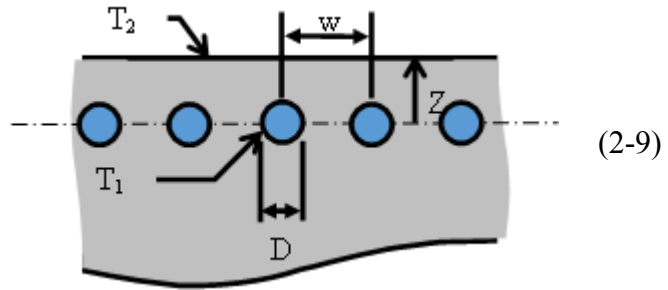
$$S = \frac{2\pi L}{\ln(4Z/D)}$$



$$S = \frac{2\pi L}{\ln(8Z/\pi D)}$$



$$S = \frac{2\pi L}{\ln\left(\frac{2w}{\pi D} \sinh \frac{2\pi Z}{w}\right)}$$



where S is the CSF in meters, L is the length of the cylinder, Z is the distance between the center of the cylinder and the surface of the embedding material, D is the cylinder diameter, w is the distance between centers of adjacent cylinders, T_1 is the isothermal cylinder temperature, and T_2 is the isothermal surface temperature. Equation (2-7) is the CSF for an isothermal cylinder in the mid-plane of an infinite plane-wall medium. Equation (2-8) is the CSF for a single isothermal cylinder buried in a semi-infinite medium. Equation (2-9) is the CSF for many parallel isothermal cylinders buried in a semi-infinite medium, and should be multiplied by the quantity of buried parallel cylinders. The selection of CSF equation is important for an accurate model of a heat transfer problem.

HE materials and embedding materials were selected based on the existing body of work in the field of electrothermal IPS. It would not be practical to test hundreds of conductors as heating elements so three categories were chosen: a metal, a carbon fiber, and a carbon nanotube network. The embedding material was not the objective of this study. The selection of embedding material is first discussed. Then justification is given for the selection of three HE materials.

2.1.2. Embedding Material

In any electrical IPS, the conductive heating element must be electrically insulated. Candidate dielectric materials include thin Kapton films or some form of glass fiber reinforced polymer. Kapton film thicknesses are typically on the order of less than 10 micrometers. These thin films provide very little thermal conduction resistance to the heating element. The advantage of low thermal resistance, as well as mass, is that heat is not trapped within the insulating material, and the half-time to reach a steady temperature is short. The disadvantage of such a thin electrical insulation is that it has poor mechanical properties and does not protect the heating element from impact damage, erosion, or deformation. Glass/epoxy composites, on the other hand, provide more mechanical stability. The trade-off is that these composites have a higher thermal resistance to the heating system than Kapton films.

History of electrothermal IPS show that the use of glass/epoxy as an insulating material is quite common. In wind turbine blades, the heating element may be directly embedded into the structure since the structure itself is a glass/epoxy composite.

For IPS, it is necessary to insulate the HE both electrically and thermally. Electrical insulation is needed to prevent short-circuiting of the HE and to protect surrounding conductors from high currents and voltages. Thermal insulation is needed to direct heat flux toward the surface to be protected. Glass/epoxy composites are ideal for both electrical and thermal insulation. One layer of glass/epoxy is sufficient for electrical insulation, but thermal insulation can be increased by using more layers of glass/epoxy. It is possible to use several layers of glass/epoxy on the back

side of a HE and only one layer on the front side such that the front will be electrically insulated and only slightly thermally insulated, whereas the back side will be both electrically insulated and significantly more thermally insulated than the front side. In addition, preforms may be easily made using fiberglass in the form of a fabric. Epon 862 epoxy resin with Curing Agent W was selected as a low-viscosity resin for easy wettability of the different heating element materials. Low-viscosity resin is also suitable for resin infusion, a manufacturing process commonly used on large composite parts for naval and wind turbine applications. Typical properties of glass fibers, Epon 862 resin, and the resulting composite are shown in Table 2-1 and Table 2-2.

Table 2-1: Embedding Material Mechanical Properties

Property	Unit	Glass Fibers [19]	EPON 862³ w/ Curing Agent W [20]	Cured Glass/Epoxy Composite⁴
Young's Modulus	GPa	76 – 78	4.1	48
Elongation at break	%	4.5 – 4.9	8.5	-
Tensile Strength	MPa	3100 – 3800	83	2100

The transient and steady performance of electrothermal IPS depend largely on their embedding materials. Electrical heating elements should not be embedded directly into carbon/polymer composite structures. Electrical current passing through the heating element would be transmitted to the carbon fibers in an uncontrolled fashion. Instead, heating elements are embedded into glass/polymer composites, who may then be layed up into a carbon/polymer composite structure. For this study, the support material was the commonly used glass/epoxy composite. Some thermal and electrical properties of the composite and its constituents are found in Table 2-2.

³ Diglycidyl ether of bisphenol-F

⁴ 60% fiber volume fraction

Table 2-2: Embedding Material Physical Properties

Property	Unit	Glass Fibers [19]	EPON 862 w/ Curing Agent W [20]	Cured Glass/Epoxy Composite
Density	kg/m ³	2480	1200	1860
Thermal Conductivity	W/m-K	1.3	0.15	0.3 ⁵
Electrical Resistivity	Ω-cm	10 ²⁵	1.53 x 10 ⁸	6 x 10 ²⁴
Coefficient of Thermal Expansion	10 ⁻⁶ K ⁻¹	4.9 – 6.0	55	7.2

2.1.1. Selection of Three Heating Element Materials

This sub-section provides details on the final selection of the HE materials. Constantan was selected based on previous studies by a different author. Carbon fiber was selected as an alternative HE, and a low-cost solution. Buckypaper was selected to represent CNT HE, and for easiness of fabrication compared to CNT/epoxy.

Constantan Wire

Constantan wire was chosen as a baseline material for this study since it closely resembles the cylinders used in the CSF models; it was used also by Mohseni in [53]. It is a copper alloy (55% Cu, 45% Ni) whose most common application is as a thermocouple wire. Metal wires are

⁵ Experimentally determined using a Netzsch© LFA Nanoflash thermal diffusivity analyzer with data from a TA Instruments© Modulated Differential Scanning Calorimeter (MDSC®)

manufactured using industry standard metal forming techniques with relatively high diameter uniformity along their length. Metal wires are also homogeneous, relatively non-porous, and with an isotropic modulus of elasticity. The advantage of such properties is that the HE wire shape is not expected to deform considerably under the force of vacuum used in the composites manufacturing process. [53] proposed that the diameter of the metal HE does not affect its temperature/power performance. The study showed a more uniform temperature distribution across the lines of the heater for a thicker wire HE, with lower average temperature at a higher power input. Another data set in the same study was a direct comparison of the temperature change of thin and thick HE at varying input power, which showed little difference between the two sizes. The thicker HE was chosen because it was easier to manipulate during heater fabrication.

Figure 2-2 shows the trend of shape factor for an isothermal cylinder in the mid-plane of an infinite medium plotted against increasing HE diameter and for different distances between the center of the cylinder and the surface of the plane wall, Z [52]. The difference in shape factor between the two HE diameters tested in [53] for a mid-thickness of 0.8 mm is only 1 for a cylinder length of 1 meter. For a thinner plane wall ($Z = 0.2$ mm) the difference in shape factor caused by HE diameter is more pronounced. For the case in [53], the HE diameter did not show significant effect when their temperature/power performance was compared side-to-side, however, it cannot be said that the heating element diameter will yield the same heating performance for all heater thicknesses.

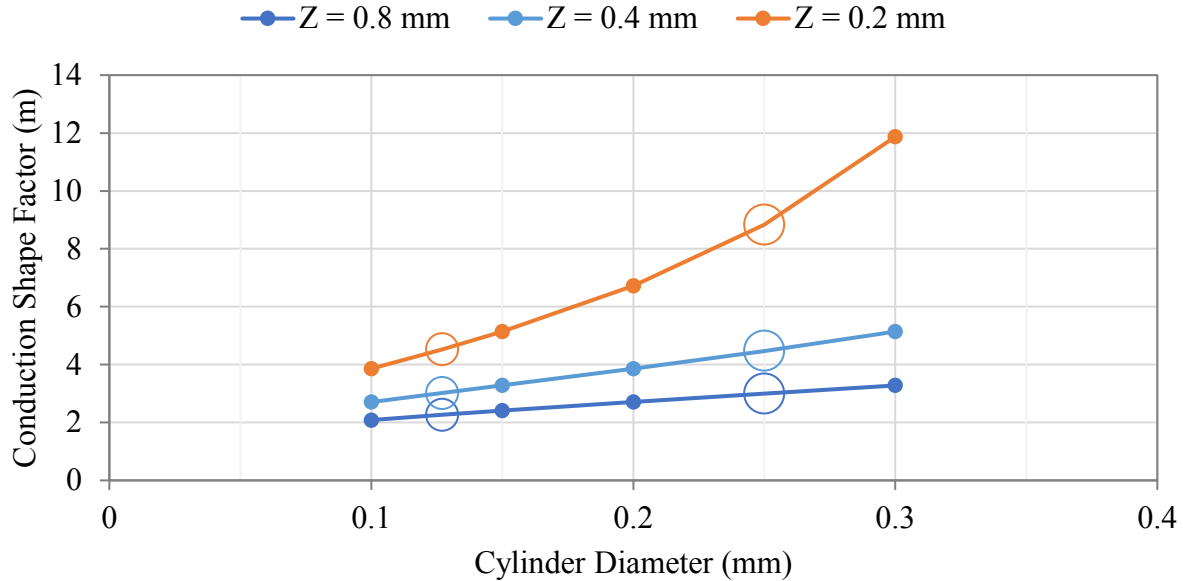


Figure 2-2: Conduction Shape Factor for isothermal cylinder in the mid-plane of an infinite plane wall for a HE length of 1 meter and varying cylinder diameters; diameters used in [53] are indicated by large circle markers

The conduction shape factor plotted in Figure 2-2 is accurate for a case where heat loss occurs on both surfaces of the plane wall in which a cylinder is embedded, as illustrated beside Equation (2-7). The resulting CSF is deceptively high compared to that calculated for an isothermal cylinder buried in a semi-infinite plane wall. The word, “deceptively”, is used here to mean that the CSF is attractive as a high number, however for the case of heating for ice protection in aerodynamic applications, it is desired for heat transfer to occur only on one surface, the surface exposed to icing conditions. A more appropriate CSF for an aerodynamic surface heating scenario is that for an isothermal cylinder buried in an semi-infinite medium, shown in Equation (2-8). The calculation of such a CSF is limited by the relation of cylinder center distance to the medium’s surface and the cylinder diameter ($Z > 1.5 D$). Meaning for a wire-HE with a diameter of 0.25 mm, the minimum Z for CSF calculation is 0.375 mm.

Except in the case of a parting strip heater, a single-wire heating HE element is rarely used; rather, wires are arranged in parallel to form a heated grid area. The CSF for a row of equally space parallel isothermal cylinders in a semi-infinite medium (Equation (2-9)) is more

appropriate for a heater grid. This CSF gives insight into the effect of heater line spacing. The CSF per cylinder slightly decreases with decreasing line spacing, however when multiplied by the increased number of cylinders that can fit in a more compacted area, the total CSF greatly decreases with increasing line spacing, as shown in Figure 2-3 for a 17-mm heater where 9 wires can fit at a LS of 1.5 mm.

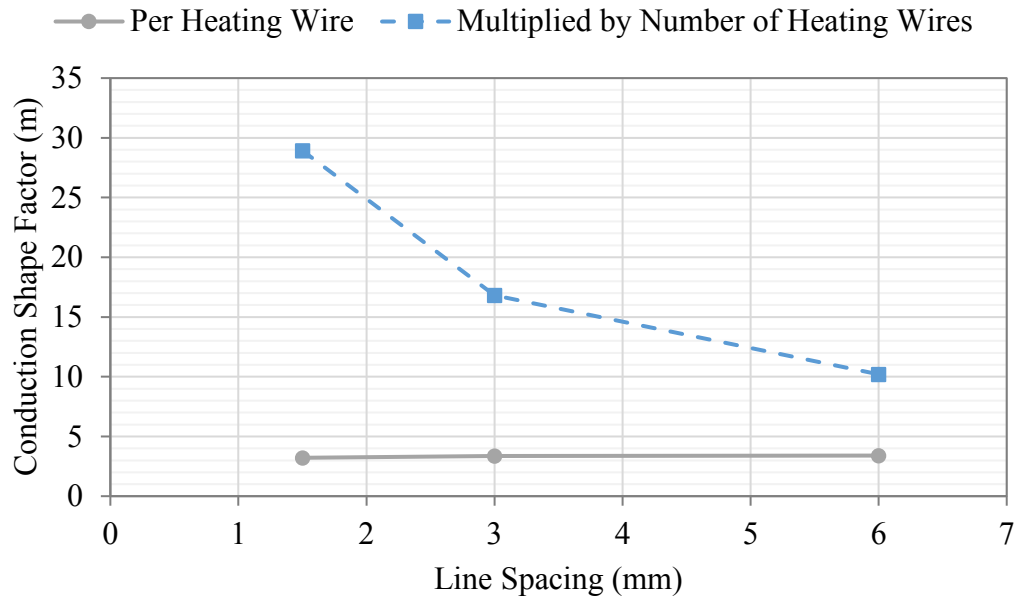


Figure 2-3: CSF calculated based on $L = 1 \text{ m}$, $Z = 0.2 \text{ mm}$, $D = 0.127 \text{ mm}$, and for varying LS, with the CSF per wire and the CSF multiplied by 9 wires, 5 wires and 3 wires respectively

For the present study, the constant HE diameter was 0.127 mm because it was readily available and the CSF calculations would be more accurate using a 0.127-mm wire than a 0.25-mm wire for a surface-to-wire distance of 0.20 mm. Since, [53] has already studied changes in a metal wire HE diameter, it was preferred to study changes in a deformable CF-tow HE diameter.

Carbon Fiber Tow

The advantage of a carbon fiber heating element can be viewed as follows. If a potential difference across a resistor causes an electrical current to flow through it, heat generation will occur equal to the electrical power delivered. If one would like to decrease the heat generation in that resistor but would like to maintain the electrical resistance value, a current or voltage divider

may be used. The current divider may appear as several resistances in parallel, and the voltage divider would be several resistors in series. Composite materials, especially glass/epoxy composites are thermally insulating and limited in operating temperature. It is therefore desirable to avoid concentrated heat sources as the heat would not be easily diffused throughout the structure. The interface between the heat source and the composite may overheat before the desired point on the surface reaches the target temperature. A superior strategy would be to divide the same input power over a larger area of the structure. If the same resistance is to be used as with the single source heater, a more electrically resistive material ought to be used. Carbon fibers represent this superior alternative in relation to thin film metal heaters, carbon nanotube heaters, and metal wire heaters.

Carbon fibers were chosen because they add mechanical strength to composite materials and blend in relatively well with glass/epoxy; or at least more so than constantan wires. Carbon fiber tows are bundles of individual filaments. Bundles of filaments are a sort of variation on the idea of embedded wire HE in that they are many wires in parallel. The bundle may be treated as a wire HE which is porous, permeable, and deformable in the transverse direction. The HE-wire shape is expected to deform under the force of vacuum.

Carbon Nanotube Buckypaper

Carbon nanotubes were chosen to represent a novel HE material. Studies have suggested that carbon nanotubes have superior heating performance than other materials, [37, 48, 54, 55, 56], and part of the objective of this study is to test that hypothesis. Carbon nanotubes were used in the form of buckypaper. Initially, a heater was made where the nanotubes were mixed with epoxy resin. The resin became extremely viscous and had the consistency of a thick paste (Figure 2-6 (a)). Layers of dry glass fiber fabric were laid over a layer of the nanotube/epoxy resin and cured as a composite. The first trial was successful; however, the heater side of the composite was conductive (Figure 2-4).

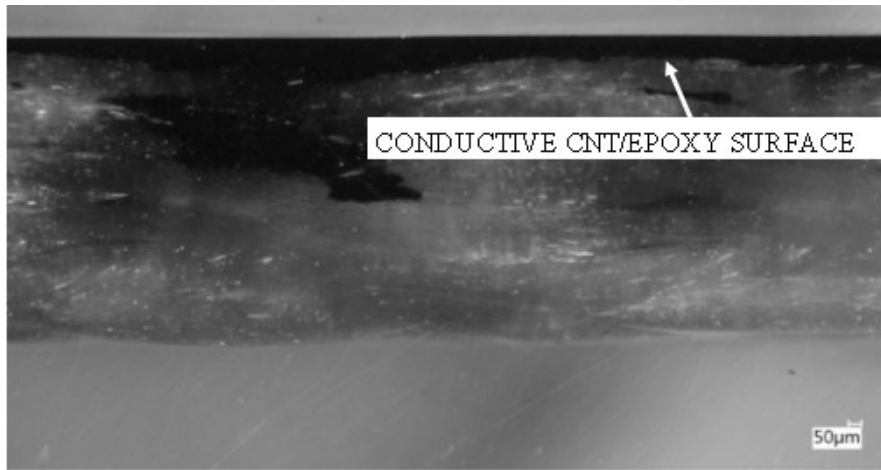


Figure 2-4: Microscope image of glass/epoxy/CNT laminate cross-section showing accumulation of CNT at one surface

One of the design criteria of the heaters is to be entirely insulated electrically. To meet that criteria, further attempts were made to first place a layer of dry fabric, spread the epoxy over that first layer and then the other five layers with copper wires passing through (Figure 2-5 (b)) to be used as electrical terminals; shown schematically in Figure 2-5.

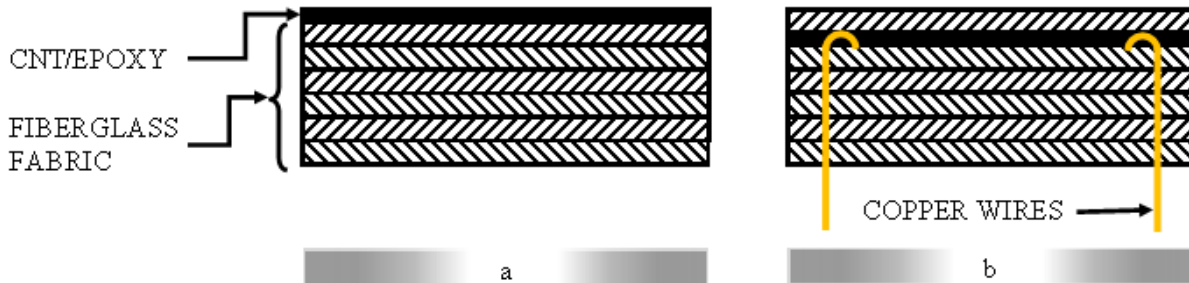


Figure 2-5: Cross-section schematic of glass/epoxy/CNT heater laminate with (a) first successful iteration with conductive surface, and (b) sequence with insulated heater layer and copper wires to conduct electrical current to HE

These attempts were unsuccessful because the resulting laminate had many large patches of dry fiberglass fabric (Figure 2-6 (c)). The patches were dispersed such that no heater sample could be cut out from the larger square without major defects.

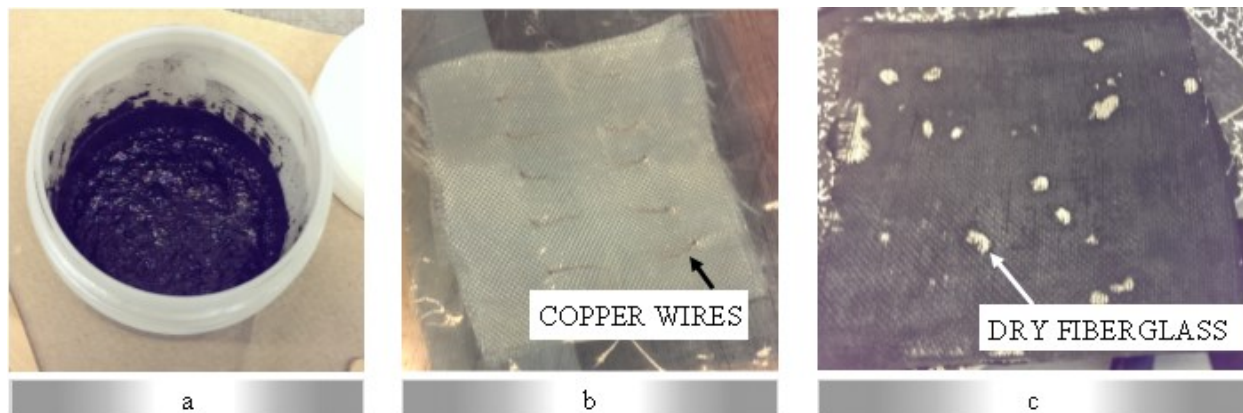


Figure 2-6: Failed attempt at producing Glass/Epoxy/CNT heater with (a) viscous epoxy/CNT mixture, (b) dry fiberglass layers with through-thickness copper wires, and (c) tool-side of the resulting laminate with dry (unwetted) patches

A buckypaper form was preferred because it is easily manipulated and could be embroidered into the fabric. The buckypaper format was an acceptable match for comparability with the other embedded heaters. As opposed to the constantan and CF HE, those made from buckypaper retained the shape of a film rather than a wire. An attempt was made to reduce the aspect ratio of buckypaper HE by cutting narrow strips, however, the smallest aspect ratio of width to thickness obtained was on the order of 22; the target aspect ratio was 1 like for constantan, or 5 for vacuum-cured CF tows. For comparison, the physical and mechanical properties of the chosen HE materials are listed in Table 2-3 and Table 2-4 respectively.

Table 2-3: Heating Element Material Physical Properties

Property	Unit	Constantan [57]	Carbon Fiber [18]	Carbon Nanotube Buckypaper [58]
Form	-	Wire	Tow	Sheet
Thermal Conductivity	W/m-K	21	10.5	0.4
Density	kg/m ³	8900	1760	200
Volume Electrical Resistivity	μΩ-cm	50	1650	25-50 x 10 ³
Thermal Diffusivity	m ² /s	-	7.48	106 x 10 ³
Coefficient of Thermal Expansion	μm/mK	15	-0.4	-
Temperature Coefficient of Resistance	10 ⁻⁶ K ⁻¹	20	247 – 308 [58]	-

Table 2-4: Heating Element Materials Mechanical Properties

Property	Unit	Constantan [57]	Carbon Fiber (fiber direction) [18]	Carbon Nanotube Buckypaper [59]
Form	-	Wire	Tow	Sheet
Young's Modulus	GPa	165	228	0.4
Elongation at break	%	32	1.6	1
Tensile Strength	MPa	380 – 930	1650	4

The chosen HE materials vary in terms of electrical, mechanical, thermal and chemical properties. One thing they have in common, though, is that they are able to conduct electrical

current. Another commonality is that they are all solid, flexible, and they could all be easily embroidered; an essential requirement for the sample fabrication process.

2.2. Manufacturing Process

Four steps are used to describe the fabrication process of heater sample. The steps are summarized in Table 2-5 and listed below:

- I - Preform Fabrication: the dry joining of heating element material to a fiberglass fabric base.
- II - Lead Connections: permanent joining of heating element ends to copper wires.
- III - Composite Layup: wet layup of glass/epoxy laminate with preform and preparation of terminal wires.
- IV - Finishing: cutting of samples, electrical connections, and electrical repairs.

Table 2-5: Steps in sample manufacturing

I Preform Fabrication	II Lead Connections	III Composite Layup	IV Finishing
Cut Materials: CF Constantan Buckypaper FG Thread FG fabric	Cut Materials: Copper Wire Aluminum Foil	Cut Materials: Bleeder Breather Peel Ply Vacuum Bag FG fabric	Cut Materials: Cured samples
Straight embroidering	Mix two-part Silver Epoxy	Release Agent on Tool	Repair damaged HE
Cross embroidering	Wetting of Aluminum Foil with Silver Epoxy	Mix epoxy resin using vacuum centrifugal mixer	Solder electrical wires
	Closing of Aluminum Foil	Wetting of layup sequence	Application of silicone
	Oven Cure under Compression	Copper wire masking and looping	Adhesion of magnetic strip
		Vacuum bagging	
		Curing in oven under vacuum	

2.2.1. Preform Fabrication (I)

A preform is used to describe the layer of fiberglass fabric with a HE fixed to it. The preform was inserted into the composite layup of the heater just like any of the other fiberglass layers. HE materials were mechanically joined to a fiberglass base fabric by means of embroidering. This section contains a process description and justification for using embroidering as opposed to weaving. The fabrication of preforms with CF HE is presented first because it was the basis for the decision to use an embroidering technique rather than weaving.

Development of Preform Fabrication Method based on CF Preform

An earlier generation of samples was made by passing carbon fiber tows directly through gaps in woven glass fabric. When viewed under a microscope, fraying of the woven HE was observed. Fraying occurred because of friction glass filaments in the base fabric. Since only one continuous carbon fiber tow was used as the heating element, fraying intensified as weaving progressed. It was especially problematic with long heating elements and with densely packed heating lines. For a better understanding of the effects of fraying, the temperature profile of sewn heaters was observed with an infrared (IR) camera.

Heating and IR Imaging for Quality Check of HE Preform

Fabric heaters were placed over a cement brick to insulate them from one side, and reducing heat loss to natural convection from the exposed top. Results showed mostly non-uniform heating over the entire area of the grid (Figure 2-7-c). Heat concentration zones occurred where fraying of the carbon fibers was most visible. In addition, where frayed fibers from different heating lines made contact, (Figure 2-7-a), a heat concentration zone appeared. The zone reduced heat generation in a greater portion of the circuit due to the creation of a parallel resistance [60]. The sewing pattern shown in Figure 2-7 (d) was an improvement of the first. The distance between grid lines was increased by passing the heating element through alternate faces of the fiberglass fabric base. Further improvement on the fraying problem was achieved by using an embroidering technique rather than weaving, as shown in Figure 2-8. Embroidering a fiber glass

“sewing thread” through the fiber glass fabric transferred the fraying problem from the HE to the sewing thread; hence the fraying problem was mitigated by embroidering.

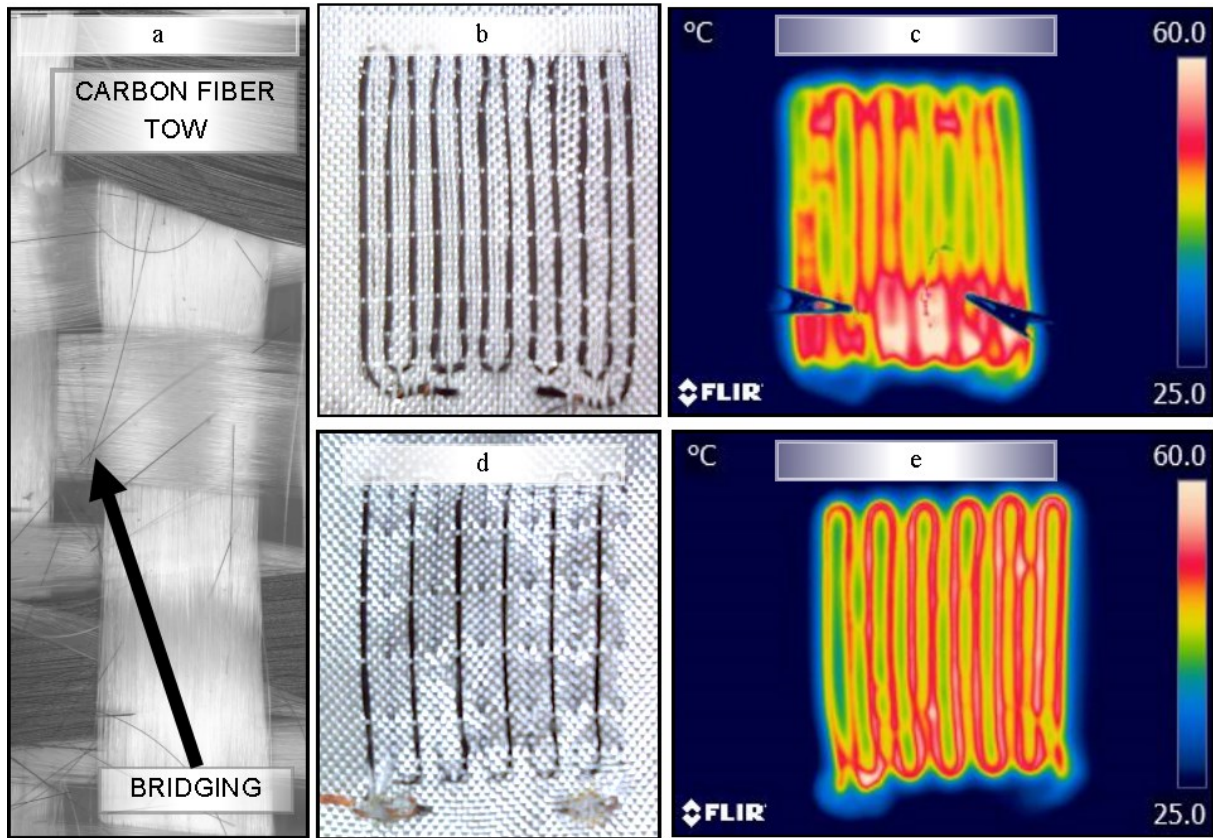


Figure 2-7: (a) Microscope image of electrical bridging due to fiber fraying, (b) the macroscopic image, (c) infrared image of bridging element, (d) improved sewing pattern, and (e)infrared image of improved pattern testing [60]

Final Solution to Fraying Problem

Samples were fabricated whose heating element was embroidered instead of woven into the base fabric. Results from previous experiments showed that tighter heating element spacing could result in faster heating response and overall better performance [61]. The purpose of embroidering was to prevent fraying in the heating element and facilitate a decreased LS. However, fraying occurred on the sewing thread, in this case fiberglass tow, when it was passed through the fabric multiple times. Embroidering transferred the fraying effect to a benign

fiberglass tow, allowing a lower minimum distance between heating element lines and less overall likelihood of electrical bridging between heating lines. The embroidered preforms were checked for frayed filaments using a microscope. Corners were especially susceptible to breaking because of the brittleness of carbon fibers. Extra fiberglass thread was used to further consolidate corner areas as an attempt to mitigate fraying. A 3K⁶-tow fiberglass fabric was chosen as the base material as a compromise between positional precision of the heating lines and friction with sewing thread. A denser fabric allows for more precise control of the position of each embroidered element, and therefore permits a tighter heating element pattern.

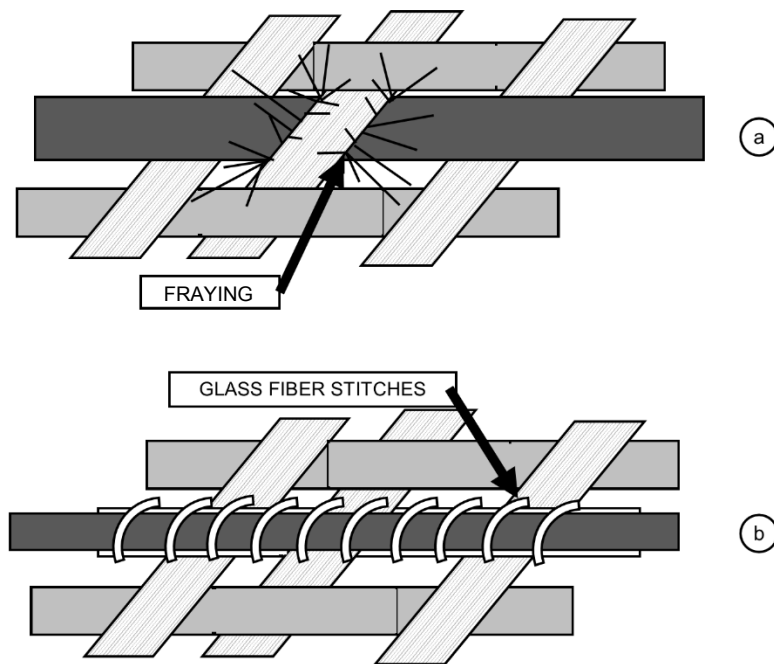


Figure 2-8: Embroidering Style with (a) weaving of HE, and (b) embroidering of HE [61]

Fiberglass fabric was cut in squares of 152 mm side length. A fiberglass 1K-tow (1000-filament bundle) to serve as sewing thread was cut to lengths of 1 – 2 meters. HE were embroidered into fiberglass fabric, with three heating elements per fabric square such as in Figure 2-9. The

⁶ 3K-tow signifies a bundle of 3000 parallel continuous filaments.

heating element was embroidered only on one side of the fabric. The ends of the heating element were passed through to the back of the fabric. They were then passed through an additional layer of fiber glass which would serve as electrical insulation between the HE and the electrical connections described hereafter.

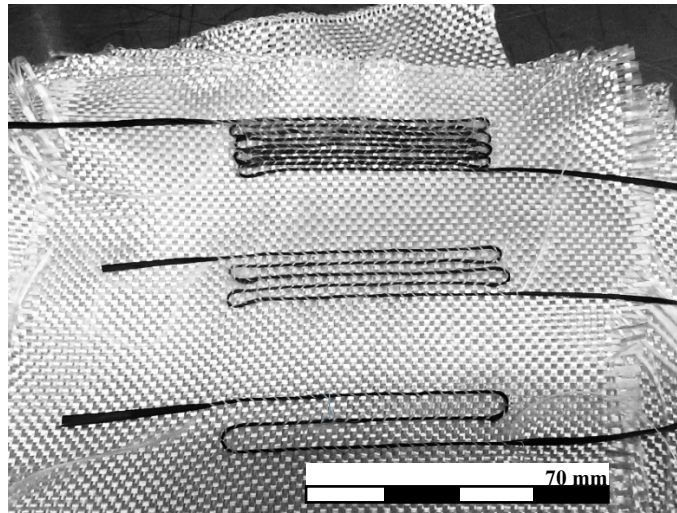


Figure 2-9: Dry Preform of embroidered heating elements with LS of 1.5mm (top), 3mm (middle), and 6mm (bottom)

Constantan Wire HE Preform

Wire heating elements were cut from rolls to lengths of 0.3 - 0.5 meters depending on LS. As warned in [53], the small diameter wire was difficult to manipulate. There was very little friction between the HE wire and the fiberglass fabric, and sometimes the wire would slip out from beneath the embroidering thread. This problem was solved by loosely embroidering the first HE line and then when the wire was bent to create the next parallel heating line, the embroidering thread was tightened. Once the first bend was embroidered wire slippage was no longer a problem. Three constantan HE were embroidered into 3K plain weave fiberglass fabric using the same procedure as described for CF.

Buckypaper HE Preform

Buckypaper HE were cut from an existing buckypaper sheet of 152 mm x 152 mm into smaller rectangles of 17 mm x 80 mm. Two of the three buckypaper rectangles were then cut into smaller strips of 1 mm width, which was the smallest manageable cutting width using conventional scissors. One rectangle (17mm x 80 mm) was used to make a continuous HE. The border of the continuous HE was embroidered into the FG fabric. The short edges of the continuous heater were scored and passed through to the opposite face of the FG fabric for electrical connection. The thin buckypaper strips were embroidered into the FG as described for CF, except they were individual strips instead of one continuous element. The short ends of the strips were passed through to the opposite face of the FG fabric for electrical connection. As opposed to constantan and CF tow HE, buckypaper HE lines were connected in parallel (rather than in series to create one continuous element). The strips were used to make 3-mm LS and 6-mm LS heaters.

2.2.2. Lead Connections (II)

Copper wires were wrapped around the exposed ends of the heating elements. A compromise was made for the wire diameter. Larger wire was desired to prevent breaking of the wire after repeated bending, and for low electrical resistance. Smaller wire was needed to prevent large defects in the composite. The junction between heating element and copper wire was enveloped in a folded square of aluminum foil. The foil was perforated using a needle. Two-part silver-filled epoxy (AI Technology EG8020) was applied to the junction inside the aluminum foil envelopes. Release film was placed over the junction and the dry heater was placed in an oven for the silver epoxy to cure. The cure cycle, shown in Figure 2-10, lasted 1 hour at 250 °C in a pre-heated oven. A steel block was placed over the junctions as a weight to prevent volumetric expansion of the epoxy. After 1 hour of cure, the oven was switched off, the block was leaned on a wall of the oven (it was too hot to remove), and the heater preform was removed. Electrical

resistance across each HE was tested to ensure acceptable contact resistance with the copper wires. At this point in the process, the preform was ready to be used in the composite layup.

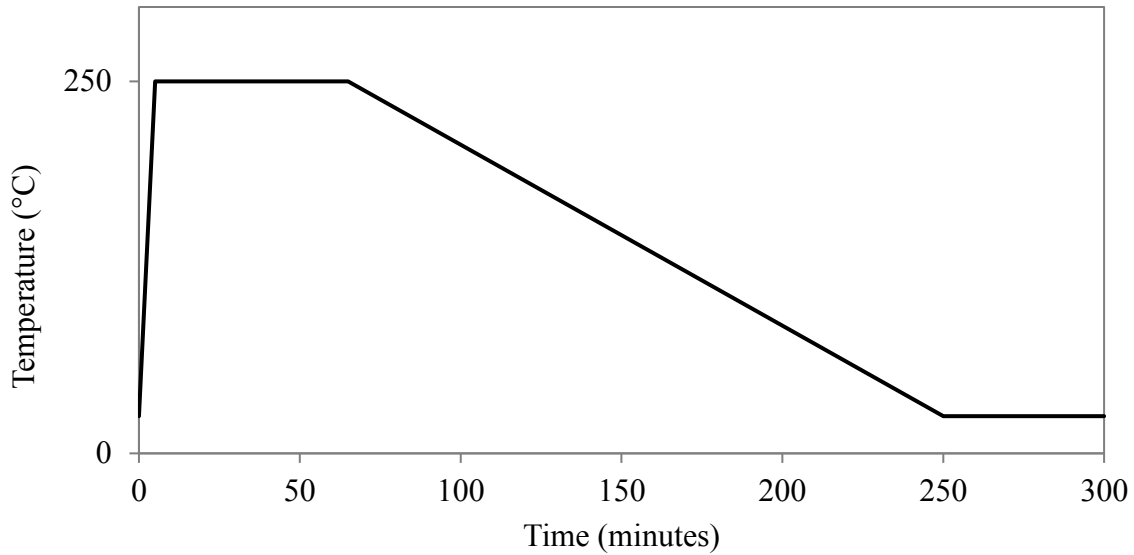


Figure 2-10: Cure cycle used for AI-Technology silver two-part epoxy

2.2.3. Composite Layup (III)

The composite was made using wet layup. An aluminum flat plate was used as the tool, and conventional layup materials were used in the order specified in Figure 2-11. Once the bagging materials were prepared by cutting to size, four additional layers of fiberglass fabric were prepared in squares of 153 mm side length. Release film was placed directly on the tool to prevent sticking of the composite after cure. EPON 862 epoxy resin was measured into a vacuum flask and Curing Agent W was poured into the same flask at a ratio of 100:26.4 [62]. The two components were mixed using a centrifugal vacuum mixer.

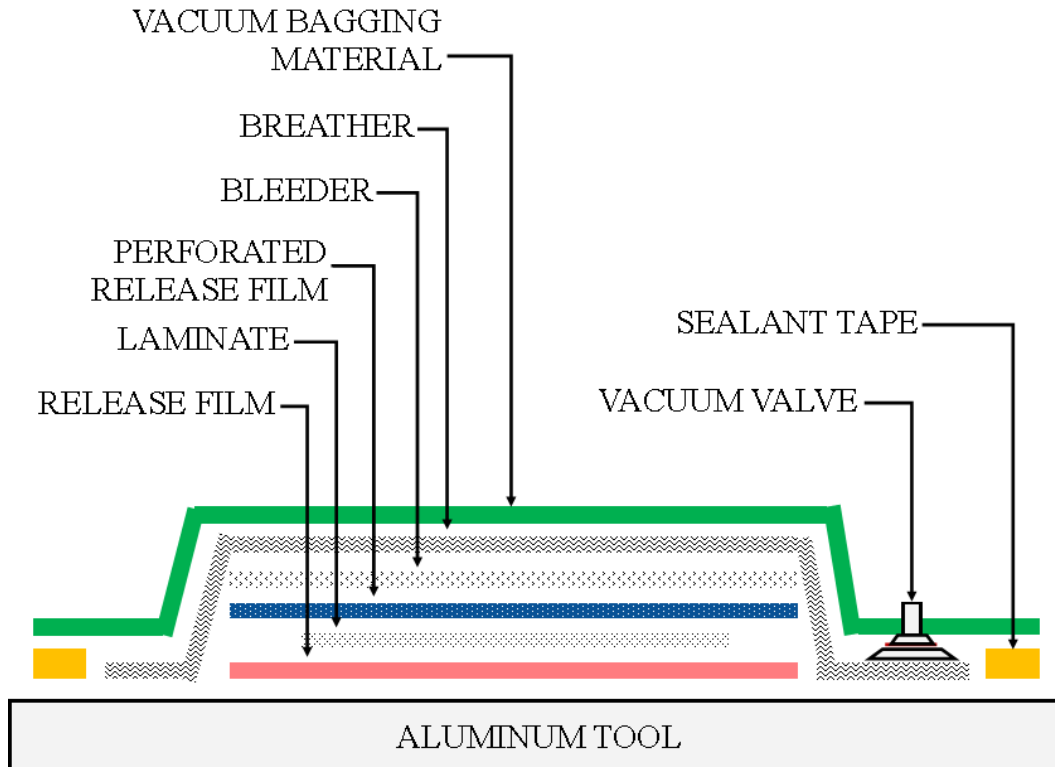


Figure 2-11: Vacuum bag layup schematic

The layup was then started with one layer of fiber glass, followed by the heater face-down with the electrical contacts facing up. The rest of the fiber glass layers were placed on top sequentially while passing the electrical contacts through them. Figure 2-12 shows a schematic of the layup sequence with the copper wires. Once the final fiberglass layer was in place and wetted with epoxy resin, each copper wire was passed through a piece of pierced release film. The free end of each copper wire was passed through a second hole in the same piece of release film and re-entered into the fiberglass layup. The purpose of the release film was to ensure separation of the copper wire from the composite laminate. Separation was necessary for soldering electrical leads, which will be explained in the following sub-section. Re-entry of the copper wires was to prevent excessive bending of the wires, which in previous-generation heaters, led to irreparable breakage of the wires [61].

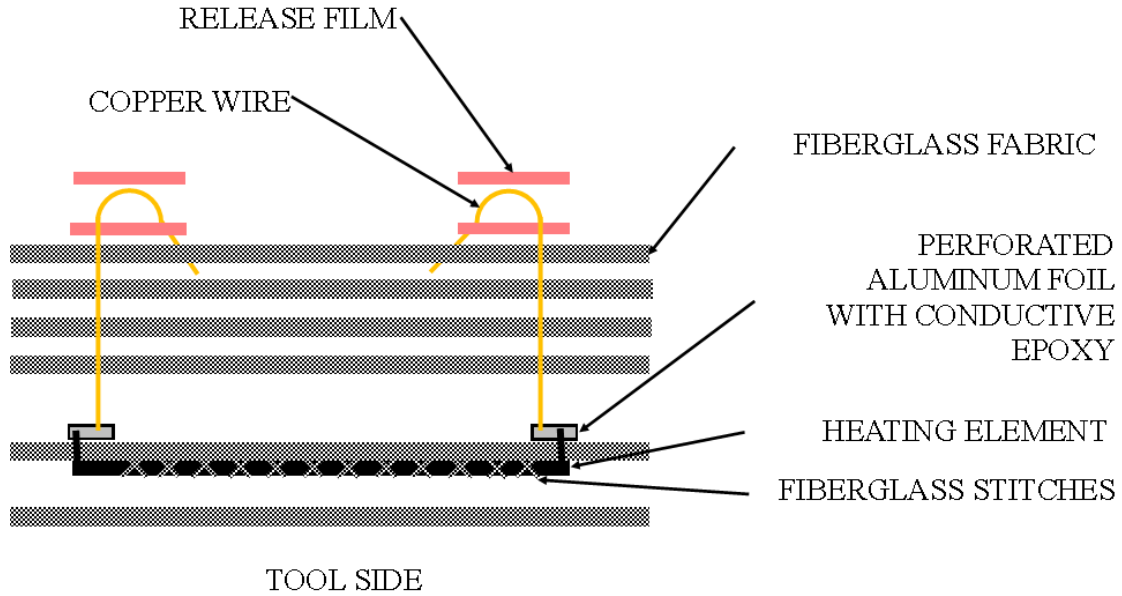


Figure 2-12: Laminate layup sequence $[0/90]_5^{Glass} [0]^{HE} [0/90]^{Glass}$

Peel ply, bleeder, breather, and a vacuum bag completed the layup sequence. The vacuum valve was placed on top of a short aluminum tube (spacer) such that excess resin would not be able to flow directly into the vacuum line. Such precautions were necessary because of the decrease in viscosity of EPON 862 epoxy resin at temperatures above 70 °C; from close to 2100 cP at 25 °C to 50 cP at 70 °C [62]. The cure cycle, shown in Figure 2-13, was a ramp up to 177 °C for 55 minutes (3 °C/minute ramp rate), held for 2 hours and left to cool overnight.

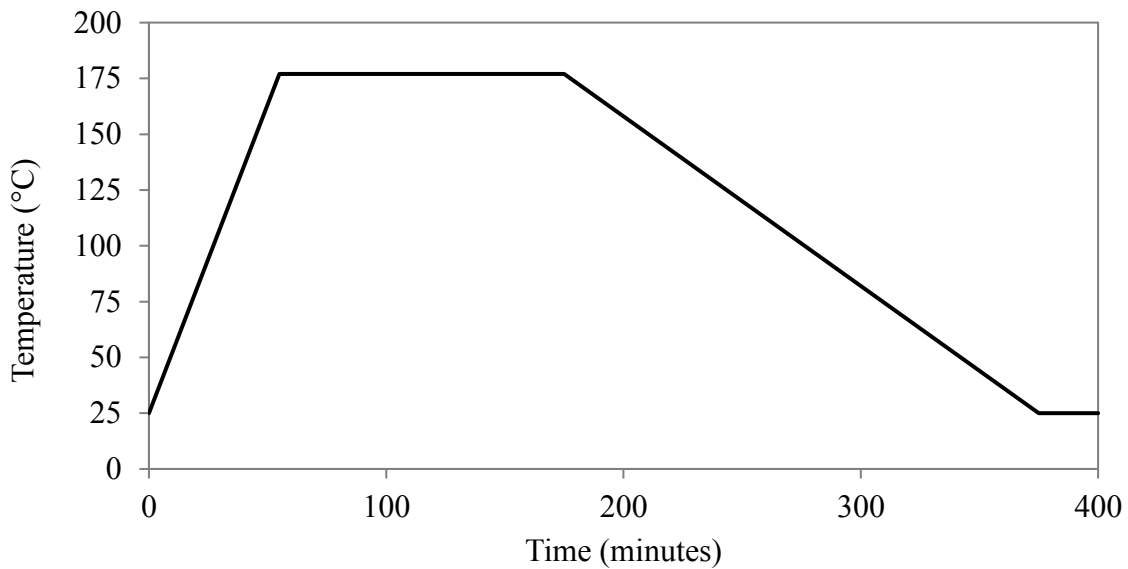


Figure 2-13: Cure cycle used for wet layup of Epon 862 with Curing Agent W

2.2.4. Sample Finishing (IV)

Cured flat plates as shown in Figure 2-14 were separated into individual heaters using a circular diamond saw. Fine adjustments to the size were made by filing. Copper Clad Aluminum wires were soldered to the exposed copper contacts on the heaters. The soldered connections were covered with silicone to protect them from moisture and to relieve mechanical stresses caused by wire manipulation.

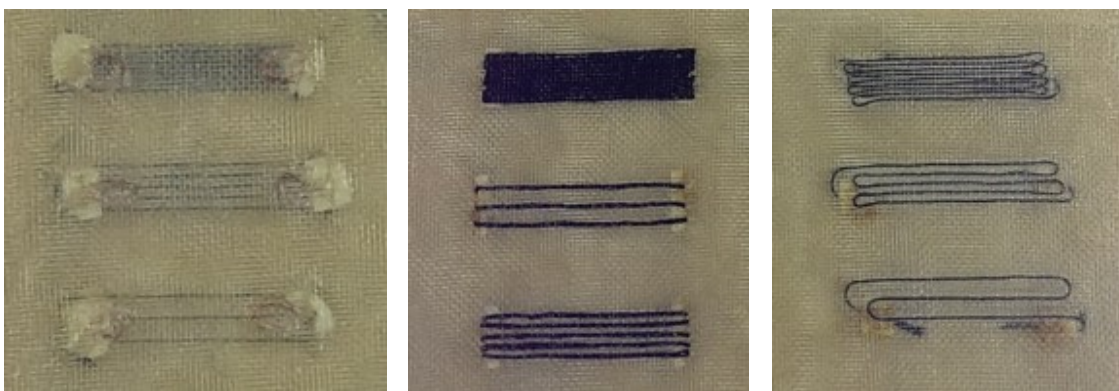


Figure 2-14: Cured composite plates showing three heaters per plate with (left) 3K CF HE backside, (center) Buckypaper HE, and (right) 3K CF HE frontside

2.3. Icing Wind Tunnel Set-Up

The Concordia University Icing Wind Tunnel was used to produce icing conditions in which to test the heaters. Specifications for the wind tunnel may be found in [63]. The layout of the IWT is shown in Figure 2-15. The spray bar was located immediately after the fan outlet. All ducts were rectangular and made from galvanized steel. The ducts were surrounded by special insulation material composed of bubble wrap and metal foil to insulate against radiation heat transfer.

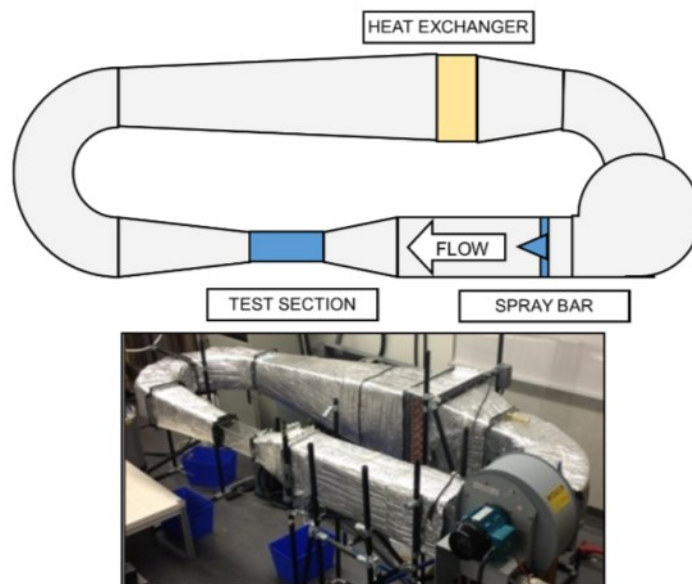


Figure 2-15: Concordia University Icing Wind Tunnel [61]

The test section of the IWT was modular. Test sections were pre-made as rectangular prisms with one face hinged, such that it would act as a quick-opening top lid. A test section was selected that had holes through the centers of the side walls and additional holes close-by for wires to pass through. A cylindrical sample holder was used to minimize aerodynamic disturbance while retaining a simple and robust fixture. The installed sample holder is shown in Figure 2-16. Two steel threaded studs pass through the entire span of the sample holder. Square permanent magnets were placed in designated grooves of the sample holder and held in place by their attraction to the studs. A short strip of magnetic tape was adhered to the back of each

sample. The sample was held in place by the magnetic force between the magnetic strip and the permanent magnet.

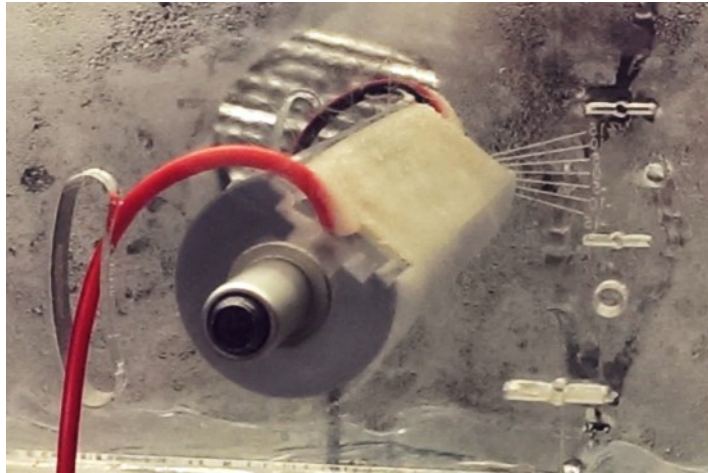


Figure 2-16: Sample holder with sample installed in IWT test section

An air atomizing nozzle was used to generate a cloud of liquid water droplets inside the IWT. The nozzle internally mixed pressurized air and pressurized water. The nozzle sprayed a circular cross-section spray. The air and water pressures were controlled using features on the panel shown in Figure 2-17.

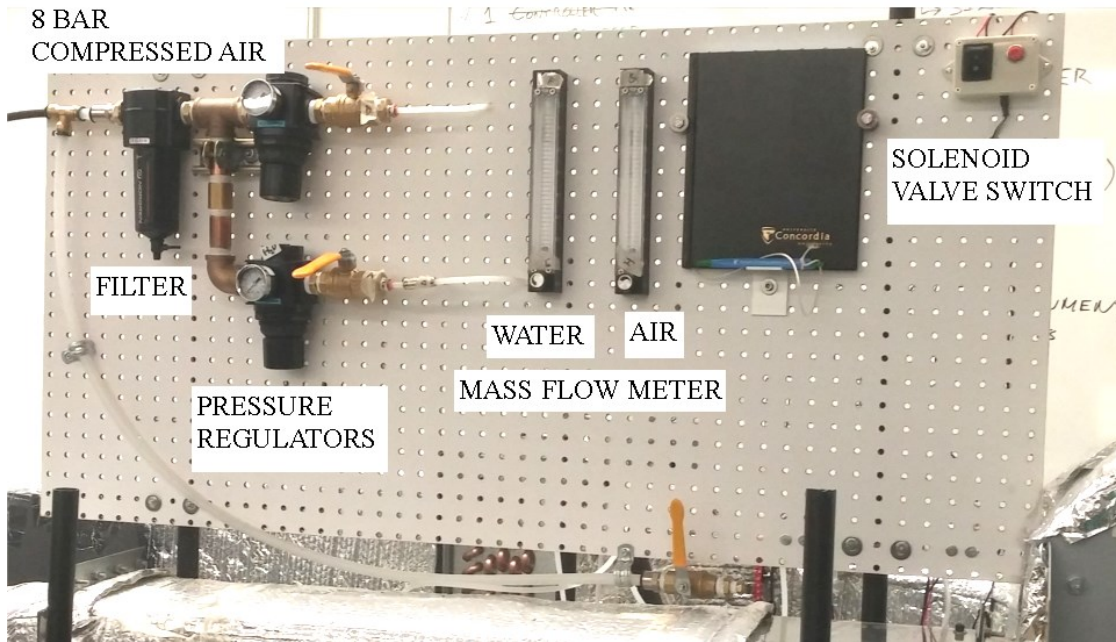


Figure 2-17: Concordia University IWT Spray Control Panel

The connections not shown in Figure 2-17 are illustrated in Figure 2-18. Air pressurized to 8 bar passes through an air filter and gets split into two pressure regulators. The topmost pressure regulator in Figure 2-18 leads to a mass flow meter and to the air inlet of the air atomizing nozzle. Air from the bottommost pressure regulator gets split into a pressure vessel containing deionized (DI) water and directly into the water inlet of the air atomizing nozzle. Pressurized water leaves the pressure vessel into a mass flow meter and into the water inlet of the air atomizing nozzle. Normally closed (N/C) solenoid valves interrupt the flow of either air or water into the water inlet of the air atomizing nozzle. The air-line into the water inlet of the air atomizing nozzle is only to purge the nozzle, as a technique to prevent freezing of stagnant water inside the nozzle when the water flow is off. A red button switch activates the purge air solenoid valve, only while the button is being pressed. A rocker switch activates the pressurized water feed into the nozzle, and remains on or off without any spring-back. The advantage of a solenoid valve instead of a ball valve was the response time of the water spray.

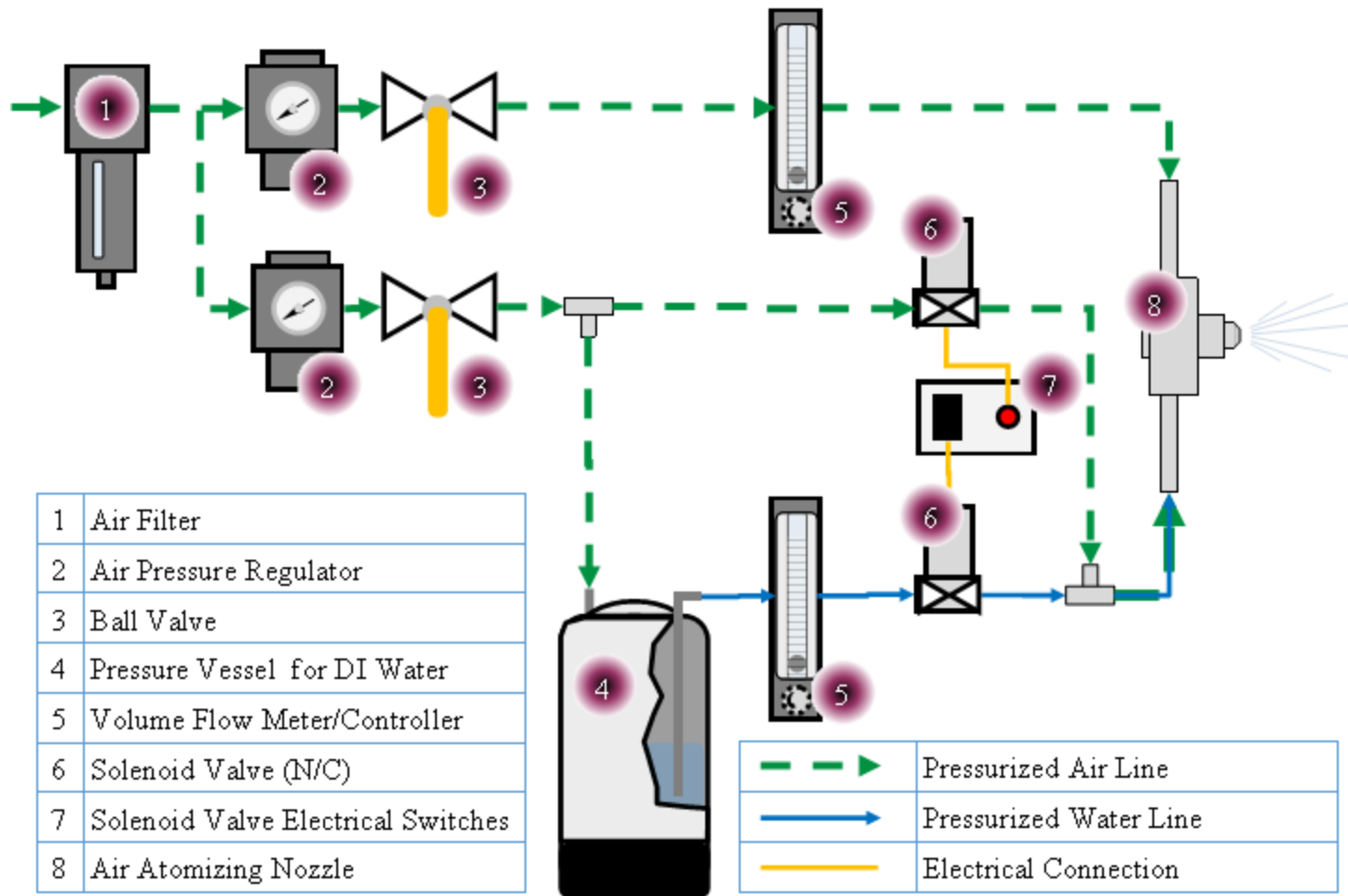


Figure 2-18: Pneumatic and Water Spray System Diagram

Wind Speed Calibration and Control

PIV and manometer measurements in a closed loop configuration and with an empty test section revealed that the relation of test section air speed and fan motor inverter frequency was nearly 1:1. U-tube manometer measurements were also performed. The results of the two tests are shown in Figure 2-19. With a partially obstructed test section (i.e. with the sample installed), it is supposed that a slight decrease in this trend would exist. The 1.5-HP centrifugal fan from Continental Fan was controlled by a three-phase ABB ACS 150 frequency inverter.

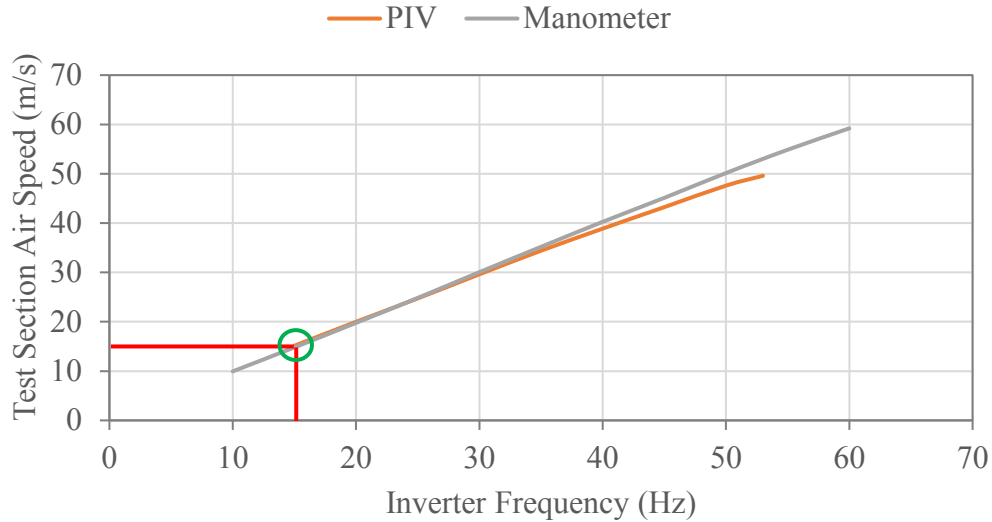


Figure 2-19: Wind tunnel test section speed calibration showing 15 m/s point

PIV measurements were analyzed by comparing two consecutive images of spray droplets flowing through the IWT test section. It was assumed that the droplets were moving at the same speed as the air. Their mean volumetric diameter (MVD) was measured as 25 μm . At that size, water droplets have little inertia. Drag forces from the air flow accelerates them in the direction of the airflow. The agreement between manometer measurements and PIV measurements in Figure 2-19 validates this assumption. The deviation between measurement methods at higher speeds is attributed to shorter residence times of the droplets in the airstream. They appear to be slower in the PIV measurements because they do not have enough time to accelerate fully to the speed of surrounding air.

Liquid Water Content (LWC) Calculation

Due to the lack of available equipment for LWC calibration, a simple calculation was used to estimate the amount of water in the cloud entering the test section. The setting on the flowmeters indicated the volume flow rate of water into the nozzle. All the water enters the cloud, but only 30% enters the test section. This assumption has been validated by PIV measurement in in [63]. In addition, it is assumed that the cloud is uniform over the entire test section cross sectional

area. The water is also assumed to carry the same velocity as the airstream. The LWC (g/m³) could therefore be calculated as:

$$LWC = \frac{\dot{V} \times \rho_{Water}}{U_{air} \times A_{TS}} \quad (2-10)$$

where \dot{V} is the volume flow rate of water passed into the air atomizing nozzle in m³/s; ρ_{Water} is the specific mass of water, which is 1000 kg/m³; U_{air} is the speed of the airflow in the center of the test section in m/s; and A_{TS} is the cross-sectional area of the test section in m². To adjust for the loss of LWC mentioned earlier, the value calculated in Equation (2-10) is multiplied by 70%. The accuracy of LWC is not critical for this study, since the conditions are not chosen to reflect a specific in-flight condition. Rather, it is more important to control the precision of LWC in this study so that the condition remains consistent for all test runs.

Temperature Control

A 1.5 HP condensing unit from Tecumseh, using R404 refrigerant, provided the cooling power. It was controlled using a closed loop system. The temperature feedback provided to the controller was a T-type thermocouple probe at the end of the second diffuser, and just upstream of the heat exchanger. The probe was located there because of length restrictions to the sensor cable and for the feedback temperature to be the warmest in wind tunnel; considering the distance for air to travel and gain heat from the outside environment. The condensing unit was controlled by a Boolean on/off method and with a 60-second minimum delay between switching.

2.3.1. On-Line Measurement Equipment

Passive monitoring equipment was used to maintain test conditions between experiment runs. All the equipment used was commercially available, and was paired by the manufacturer's software. Equipment was needed to monitor air temperature, substrate surface temperature, and real-time ice coverage on the heaters.

Temperature

Air temperature was monitored using a T-type thermocouple probe placed in the end of the first diffuser. Another T-type thermocouple was adhered to the bottom of the inside of the test section. The thermocouples were connected to a National Instruments USB interface. National Instruments Signal Express software was used to log temperature data from the thermocouples.

IR Camera

Accurate IR imaging is largely dependent on well calibrated input values, such as the emissivity of the target. When an IR-transparent window is used, complexity is increased by the influence of the temperature of the window and its transmissivity. The preferred method to measure some of the parameters is, for example, to place thermocouples directly on the surface of the heater; however, those may affect the heat transfer to the surface under inspection. Alternatively, thermocouples could be placed on the rear of the heaters, however information such as temperature uniformity, maximum, and minimum temperatures would not have been available.

A FLIR A320 thermal camera was used for surface temperature measurements. It was equipped with a 10-mm focal length lens. A distance of 50 cm between the camera lens and the substrate was used for the surface temperature measurements, as depicted in Figure 2-20. At this distance with the 10-mm lens, images were taken with a resolution of 1.69 mm/pixel. For heat uniformity measurements, the camera was placed 30 cm away from the substrate, as is shown in Figure 2-21. At this distance, the resolution was less than 0.56 mm/pixel, however it was close to the minimum distance for the focal range of the lens, and it was desired to be away from the lens's limitations. Black electrical tape was placed over the thermocouple adhered to the bottom of the test section. The thermocouple with tape was used as a reference for the thermal images.

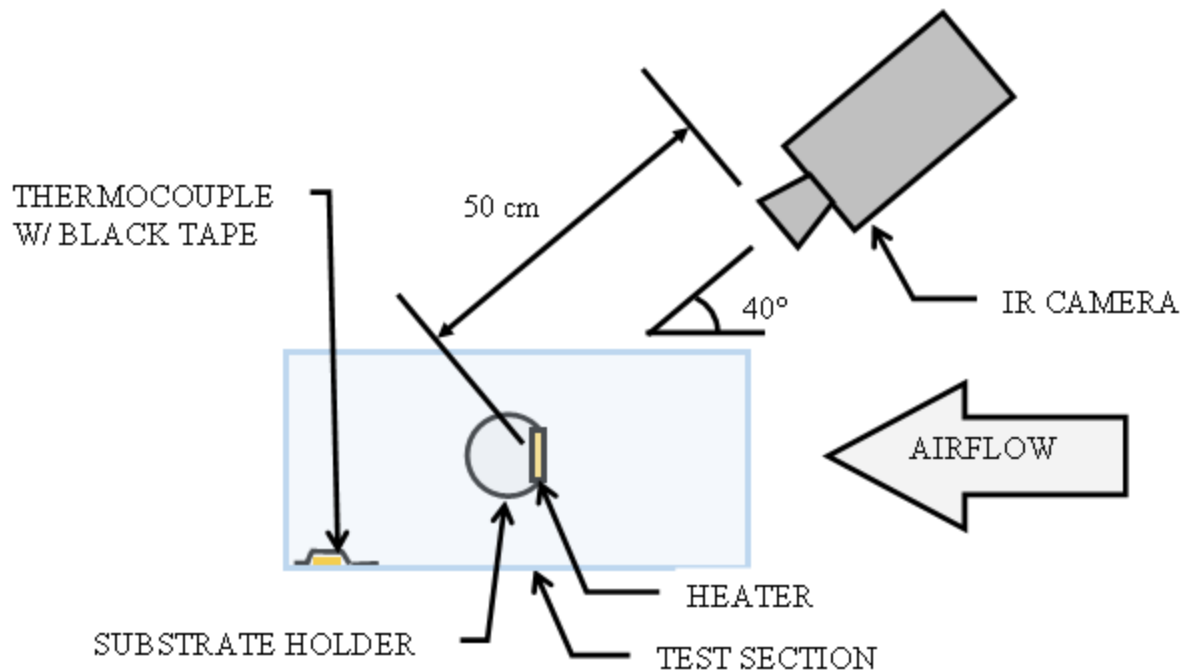


Figure 2-20: Schematic of IWT heater surface temperature measurement setup showing angle and distance of camera w.r.t. test section and substrate

The top cover of the test section was replaced by an IR polymer which had a relatively high transmissivity of infrared wavelength, as suggested in [53]. Due to high relative humidity outside the wind tunnel and low temperatures within, fog would form on the outside surface of the IR polymer window. It was therefore necessary to use a flow of dry compressed air over the window and the walls of the test section for the duration of the experiments. As the air flow was increased, the test section wall temperature would also increase. It was necessary to keep the air flow to a minimum to keep the IR polymer window temperature constant. The window had a 64% transmittance of the desired wavelength, so the temperature reading of the sample surface was highly sensitive to the window temperature. A thermocouple monitored the window temperature throughout the experiments.

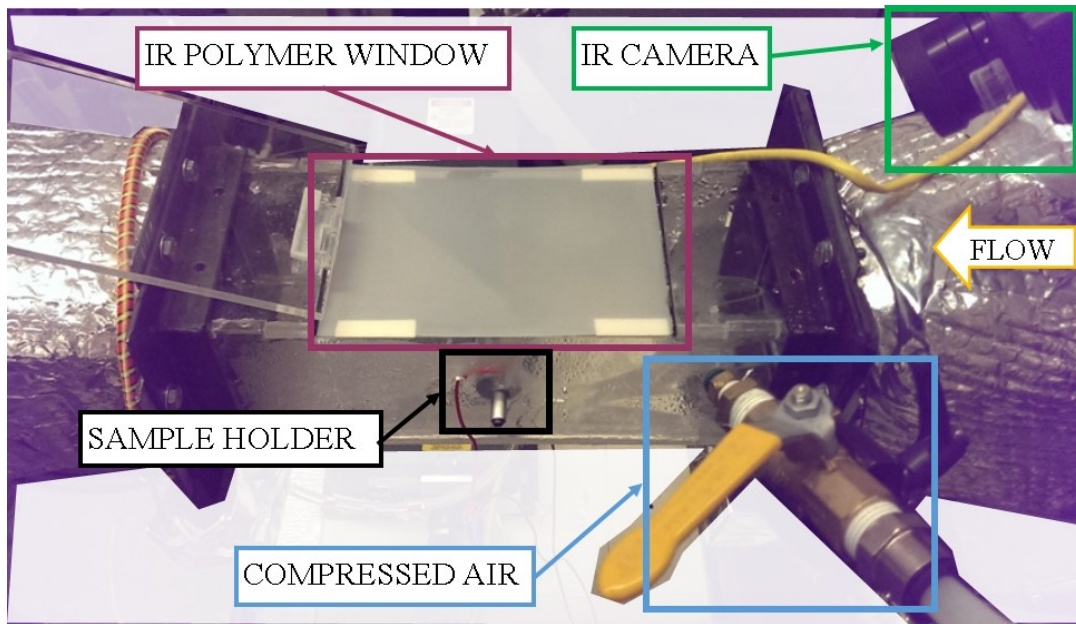


Figure 2-21: Surface temperature measurement setup showing location of sample holder, IR camera, polymer window, and compressed air for fog prevention

De-Icing Time Measurement Cameras

Two cameras were used simultaneously to compensate lighting effects and dropped frames. Compressed air blown onto test section was a means of fog prevention. Details of the two cameras are listed in Table 2-6. Their configuration with respect to the IWT test section is shown in Figure 2-22.

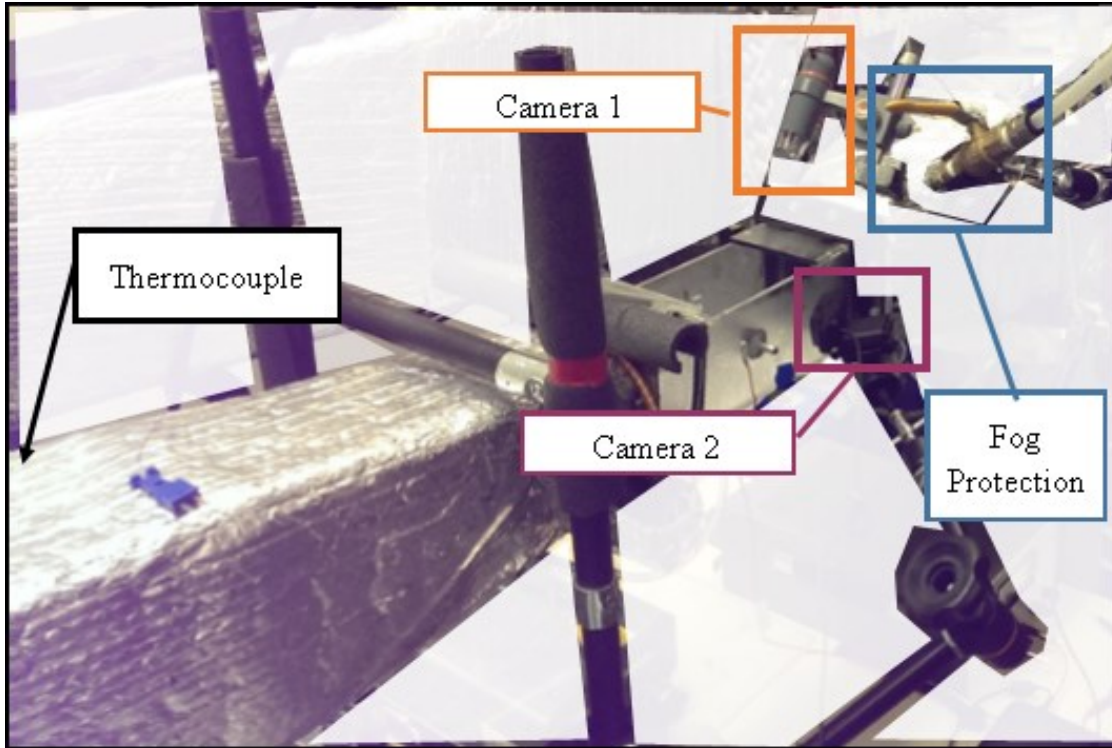


Figure 2-22: De-Icing Set-Up in IWT with (Camera 1) front view camera, (Camera 2) side view camera, (Fog Protection) compressed air, and (Thermocouple) static air temperature sensor

Table 2-6: Optical camera technical specifications

Property	Camera 1 [64]	Camera 2 [65]
Brand and Model	Celestron Handheld Digital Microscope	Logitech C920 Webcam
Imaging Sensor	5 MP CMOS	3 MP
Pixel Resolution	1600 x 1200	1920 x 1080
Effective Focal Length	15.8 mm	3.67 mm
Image Distortion	0.10 %	Unknown
Field of View	13.0°	78°
Frame Rate at Max Resolution	30 fps	30 fps

2.3.1. Icing Conditions

For sub-sonic aerodynamic applications, the dominant heat transfer mechanism is convection. As apparent in Equation (2-3), material physical properties do not directly affect the magnitude of convective heat transfer. The determining factors are the convection coefficient, the temperature of the surface of the heater and of the air. For this reason, the surface temperature of the heaters should be measured in forced convective conditions with a constant convection coefficient; i.e. constant free-stream air temperature and speed. Since the final goal is icing protection, a de-icing time measurement should also be performed. The temperature measurements may serve to help explain the de-icing tests results if any anomalies are found.

Parameters such as LWC, droplet size, wind speed, air temperature, and spraying time were kept constant for all de-icing and thermography tests. Since the objectives of the study entail comparison of heaters at the coupon level, aerodynamic scaling factors were not a point of focus. The priority in testing conditions was to produce repeatable ice formations for which to compare the different HE materials. The conditions were selected such that they would produce repeatable rime ice formations which would cover as much surface area of the sample as possible, without occluding optical properties of the test section side walls.

Optical cameras were used to record the progression of ice melting during tests. Glaze ice is characteristically transparent and would be difficult to track with a visible-spectrum camera. Rime ice on the other hand, is white and feathery, which makes it easily visible by optical cameras. It was also desired to cover the entire surface of the samples with ice to exploit their capabilities or limitations.

Coarse speed selection was done in the interest of producing rime ice. The wind tunnel's condensing unit could cool the test section air down to -10 °C comfortably, and so that was the chosen temperature for the tests. With that constraint, another influential parameter for the type of ice was the speed of the air. Higher speeds are more likely to lead to the formation of glaze ice, and lower speeds, rime ice. The reason is at lower speeds, water droplets exiting the spray nozzle have more dwell time in the cold air and therefore more time to exchange heat with the air

and to become supercooled. The last influential parameter was the balance of water and air pushed through the Spray System Co. 1/8JJ air atomizing nozzle. With an external mix fluid cap and air cap combination, the manufacturer gave some recommended air and water flow rate values for the nozzle. To produce the desired ice type, it was necessary to inject far more air than was recommended. The best flow rate values found were 171317 cubic centimeters per minute (6.05 standard cubic feet per minute) for air, and 10 cubic centimeters per minute for water.

The LWC selection and fine wind speed adjustments were made such that the greatest area of the sample would be covered with ice while the minimizing the area of the test section walls that would become obstructed. The tendency was that more water fed into the nozzles would result in larger droplets, higher LWC, greater sample area covered, but more ice on the walls of the test section. Higher speed resulted in covering of narrower sections of the samples but less ice on the walls of the test section. The icing time was chosen such that the maximum surface area of the sample would be noticeably covered by rime ice.

2.3.2. De-Icing Test Procedure

To determine the power necessary for de-icing, calibration tests were carried out inside the IWT. Individually, the heaters were placed in the sample holder and the wind tunnel fan was set to 15 Hz, corresponding to a test section velocity of 15 m/s. The air static temperature was set to -10 °C.

The steady-state surface temperature measurements were used as guidelines for the de-icing tests to ensure that the samples would not be overheated. Power densities were selected such that a range of settings could be explored within reason and safely below the temperature limits of the epoxy matrix. A minimum temperature would be needed to remove ice, such as above 0 °C. Some degrees above 0 °C were selected because it was not known a-priori how much lower the temperature of the surface would be with ice accreted on it. Likewise, it was necessary to remain well below the upper temperature limit of the epoxy due to potential insulating effects of the ice.

Ice has a relatively low thermal conductivity, and as such behaves as a thermal insulator, preventing heat loss by convection from the surface of the heater. This change in heat transfer conditions from non-insulated to insulated means that the dominant heat transfer mechanism is conduction between the heater surface and the ice. The temperature gradient across a medium increases with decreasing thermal conductivity. As mentioned in Section 1.3, thermoset epoxies have a relatively lower operating temperature than most metals. At elevated temperatures, thermoset epoxies begin to degrade, along with their mechanical properties. Operation at high temperature poses a risk for structural and di-electric failure of a polymer-composite.

Electrical voltage or current settings were selected depending on the resistance of each heater. That is, instead of trying to regulate voltage and current simultaneously, either voltage or current were used to control the power. The corresponding voltage or current were monitored but not controlled. After multiplying currents with voltages, a plot of voltage vs. electrical power was obtained, from which the resistance of each HE could be calculated. Based on a voltage-swept temperature vs. power data for each individual heater – a portion of which is presented in Section 3.1 – three power density settings were selected: 5, 10, and 15 kW/m². The electrical power required to reach these power densities was based on the exposed surface area of each sample. Since all the samples had the same exposed surface area, the same electrical power was used irrespective of the heating material. The voltage used for each HE therefore depended on its resistance, and was determined with the aid of Figure 2-23.

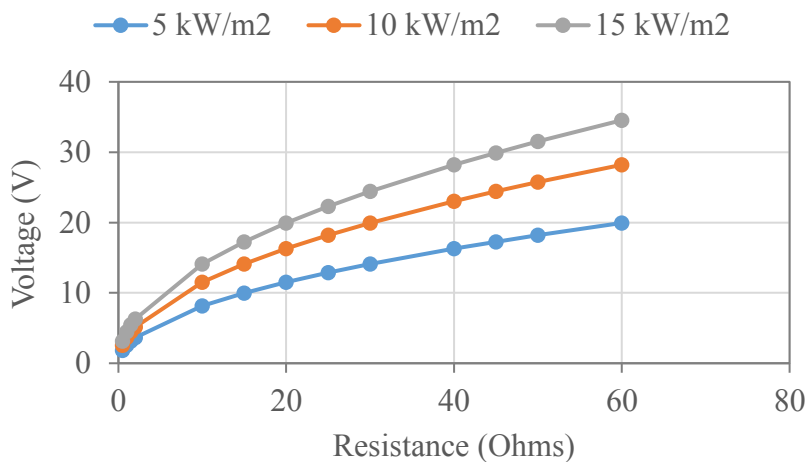


Figure 2-23: Method of voltage selection based on desired power density and heater resistance

Once installed in the IWT test section, the HE electrical resistance was measured. Then the airflow and chiller were started. As the air was cooling down, several points of voltage vs. current were recorded. Once conditions were stable, the heater was turned off. Cameras were triggered to begin recording the surface of the test specimen. Pressurized air was constantly supplied to the air-atomizing nozzle. A rocker button was pressed to activate the water spray in the IWT (activation of the button closed an electrical circuit with a solenoid valve, causing the valve to open, releasing pressurized water into the inlet of the air atomizing nozzle). At the end of the 2 minutes of spraying, the rocker switch was closed, which closed the solenoid valve and stopped the flow of water. Using the voltage set point determined prior to spraying, the heater was turned on synchronously with the cameras. The testing matrix for de-icing tests is shown in Table 2-7. A total of twelve heater samples were tested: four heating element materials, and three line-spacing for each material. Each heater was tested at three power densities: low (5 kW/m^2), medium (10 kW/m^2), and high (15 kW/m^2), for which the low was tested only once per sample, and the medium and high power settings were tested three times for each sample. The low power setting was tested only once per sample because the length of the de-icing time at that power made it impractical to repeat the condition several times.

Table 2-7: Experiment Matrix

Heating Element	LS (mm)	Set	Power Density (kW/m ²)	Number of Repetitions
Constantan (45%Ni, 55%Cu) 0.127mm diameter wire	1.5	1	5	1
		2	10	3
		3	15	3
	3	4	5	1
		5	10	3
		6	15	3
	6	7	5	1
		8	10	3
		9	15	3
Carbon Fiber PAN T300 1K Tow	1.5	10	5	1
		11	10	3
		12	15	3
	3	13	5	1
		14	10	3
		15	15	3
	6	16	5	1
		17	10	3
		18	15	3
Carbon Fiber PAN T300 3K Tow	1.5	19	5	1
		20	10	3
		21	15	3
	3	22	5	1
		23	10	3
		24	15	3
	6	25	5	1
		26	10	3
		27	15	3
Buckypaper MWCNT	0	28	5	1
		29	10	3
		30	15	3
	3	31	5	1
		32	10	3
		33	15	3
	6	34	5	1
		35	10	3
		36	15	3

2.4. Data Analysis Tools

The data collected consisted mainly of images or videos. Infrared images needed to be post-processed following some calibration of the parameters. Optical images needed to be analyzed for the presence of ice.

2.4.1. IR Images Post-Processing

FLIR Tools software was used to analyze the infrared images for data tabulation. A box was used to select the visible heated area of the heaters. Figure 2-24 illustrates the box and spot location on the IR images.

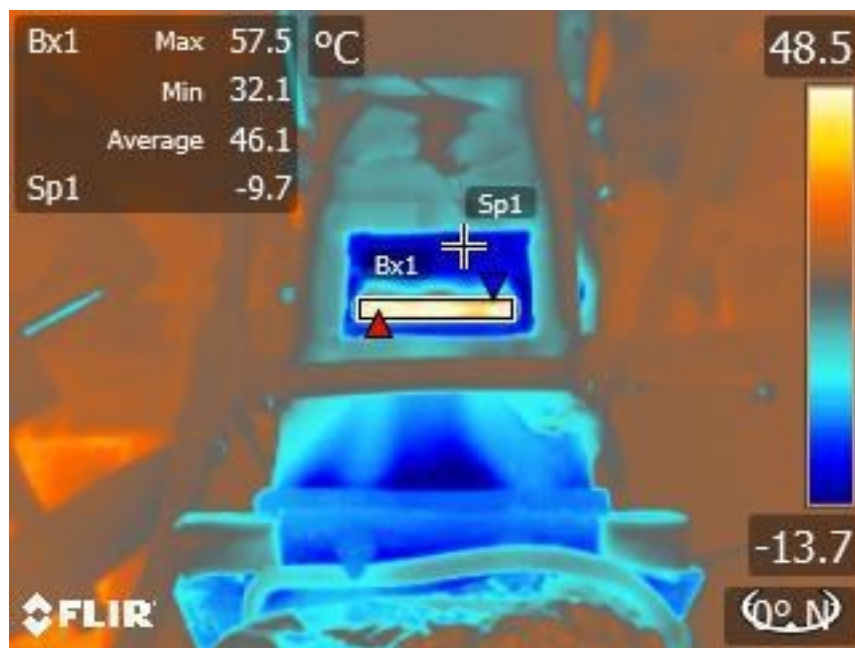


Figure 2-24: IR Image of buckypaper heater with Bx1 as the measurement box and Sp1 on the thermocouple inside the test section

The parameters used within the box are listed in Table 2-8. An emissivity of 0.97 was used for all substrates as that coming from the surface of a fiberglass/epoxy laminate. The value was in

agreement with that used by [53]. The reflected temperature had little influence on the measured temperature since the emissivity was relatively high; however, it was set to 25 °C because most surfaces in the surrounding area were approximately at that temperature. The distance used in the analysis was that of an imaginary straight line between the front of the camera lens to the surface of the substrate. The external optics temperature is the temperature of the IR polymer window. The value was monitored using a thermocouple. The external optics transmissivity was obtained by matching the temperature at one spot in the thermal image with that of a thermocouple at the same position. The relative humidity was the average relative humidity in the lab measured by a household humidity sensor.

Table 2-8: Infrared Image parameters

Parameter	Value	Unit
Emissivity	0.97	-
Reflected Temperature	25	°C
Distance	0.5	Meters
Atmospheric Temperature	23	°C
External Optics Temperature	18.0	°C
External Optics Transmissivity	0.64	-
Relative Humidity	60	%

2.4.2. De-Icing Time Measurement

The side view camera described in Section 2.3.1 captured a continuous video of each de-icing run. The front view camera captured still images every 2 seconds for 10 and 15 kW/m² runs and every 5 seconds for 5 kW/m² runs. Side view videos were used to record the time for there to be no remaining visible ice on the surface of the substrate. Front view images were processed using a threshold technique to obtain a progression of the ice remaining on the surface versus time. The two results were also compared as a sort of self-validation of the time values. The optical images will serve to determine de-icing times for each heater sample and are shown side-by-side

in Figure 2-25. Set 30 defined in Table 3-1 was an exemplary run and was used in the figure because of the clear contrast between the rime ice formation and the buckypaper film heater.

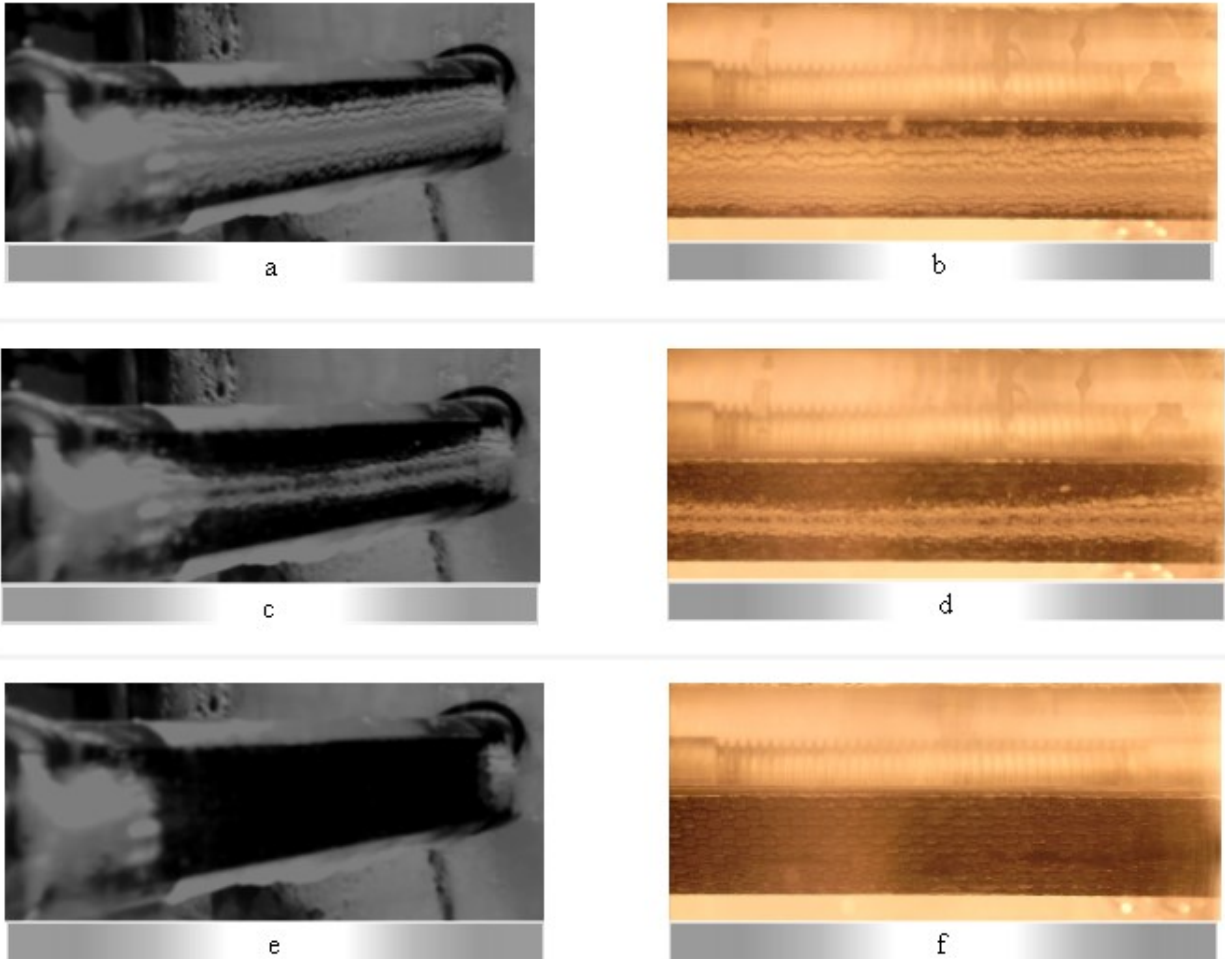


Figure 2-25: Optical camera images of Set 30 with views (a) Camera 2 at $t = 0$ seconds, (b) Camera 1 at $t = 0$ seconds, (c) Camera 2 at $t = 6$ seconds, (d) Camera 1 at $t = 6$ seconds, (e) Camera 2 at $t = 9$ seconds, and (f) Camera 1 at $t = 10$ seconds

De-icing time data will serve as an indication of the time-dependant performance of the heaters. Despite that the conditions do not represent actual in-flight icing conditions; the results of the test will serve to compare HE materials under laboratory conditions. If there is a HE material that shows a significantly superior de-icing time, the data will serve as justification for an investment into testing the heaters under more aggressive icing environments.

2.4.3. Finite Element Model

Finite element analysis was used to validate claims made to explain differences in performance of the different heaters. Specifically, the influence of the different sizes and positions of the heating elements within the laminate. COMSOL© Multiphysics Version 4.2a was used as a finite element modeling software. The Heat Transfer Through Solids module was used for simulation of two-dimensional conduction heat transfer in the heaters. The domain drawn is shown in Figure 2-26 with the boundary conditions indicated in Figure 2-27. The domain was selected as a portion of the heater such that symmetric boundary conditions could be used on either side. It represents the heat transfer that occurs near the center-width of the heater, or the middle heating wire. The internal boundaries seen in Figure 2-27 were imposed for structuring of the mesh.

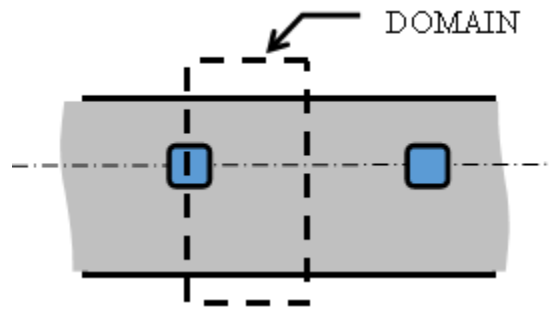


Figure 2-26: Schematic of portion of heater used as the simulation domain with glass/epoxy shown in gray and heating elements as blue-filled squares

The half-distance between the centers of two adjacent heating elements was represented by the width of the domain in Figure 2-27; thus, the LS in the simulation was controlled using the width of the domain. A convection boundary condition was imposed on the top boundary of the domain with a heat transfer coefficient of $38 \text{ W/m}^2\text{K}$ and a temperature of 263 K ($-10 \text{ }^\circ\text{C}$). The heat transfer coefficient used was that which yielded surface temperature results closest to the experimental data. A heat source condition was placed on the HE domain with the total power equal to 6.63 W , 13.26 W and 19.89 W corresponding to 5 kW/m^2 , 10 kW/m^2 , 15 kW/m^2 respectively used in experiments. An open boundary condition (Neumann or far-field boundary

condition) was imposed on the bottom boundary of the domain such that it would not influence the temperature profile in the simulation. The model did not include consideration for the thermal contact resistance between the HE and the embedding material. This simplification was made because the thermal contact resistance was not experimentally measured. The goal of the simulation was to obtain comparative temperatures of different HE geometries.

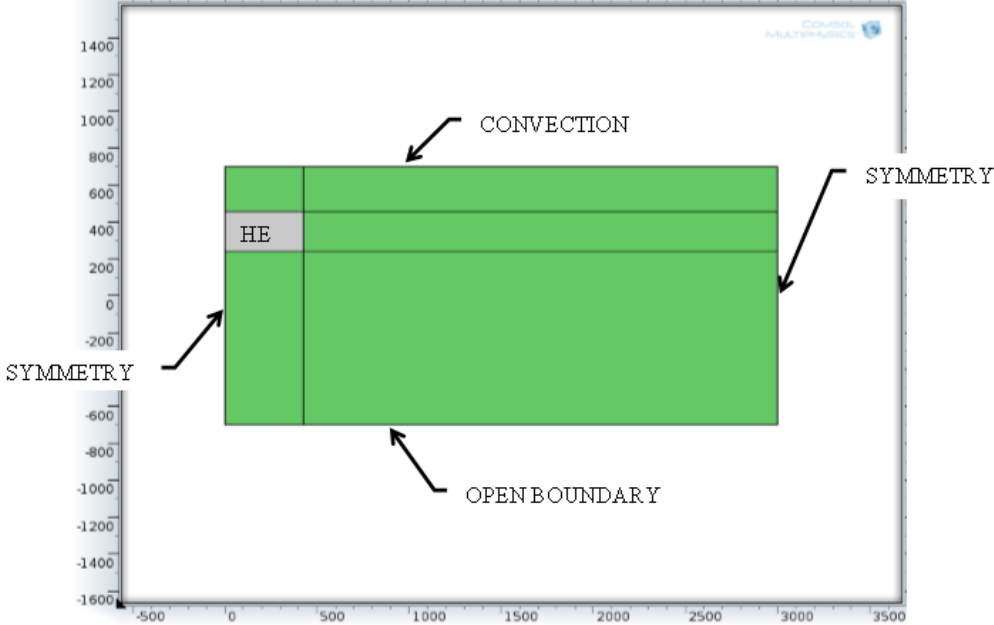


Figure 2-27: Domain used for finite element analysis showing boundary conditions used and location of HE

The mesh consisted of 34,800 elements with average dimensions of 10 μm x 10 μm . The same mesh density was used throughout the domains. An example of the mesh is shown in Figure 2-28

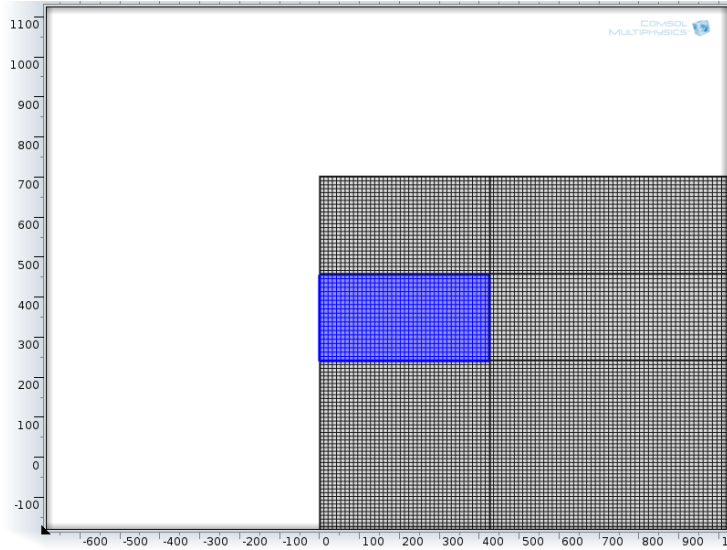


Figure 2-28: Portion of the mesh showing highlighted HE domain and with mesh density of 100 elements / mm

Materials used were from the built-in library of the software. FR4 fiberglass was used as the material for the large domain, which represents the embedding material of the heater (glass/epoxy). Specific heat, density, and thermal conductivity were 1690 J/kg-K, 1900 kg/m³, and 0.3 W/m-K respectively. The HE material thermal properties used were those listed in Table 2-3; however, changing the HE material in the simulation resulted in identical solutions. More on the lack of influence of HE physical properties is discussed in Section 4.1.

A temperature contour plot over all the domains was used to visualize the results of the simulation. Figure 2-29 shows a typical temperature contour plot of the finite element solution. Dark red shows the highest temperature and blue shows the lowest temperature. The temperature contour plot did not vary noticeably between HE sizes or LS, so measurement probes were used to extract specific temperature information; such as maximum, minimum, and average surface temperature, as well as HE surface temperature.

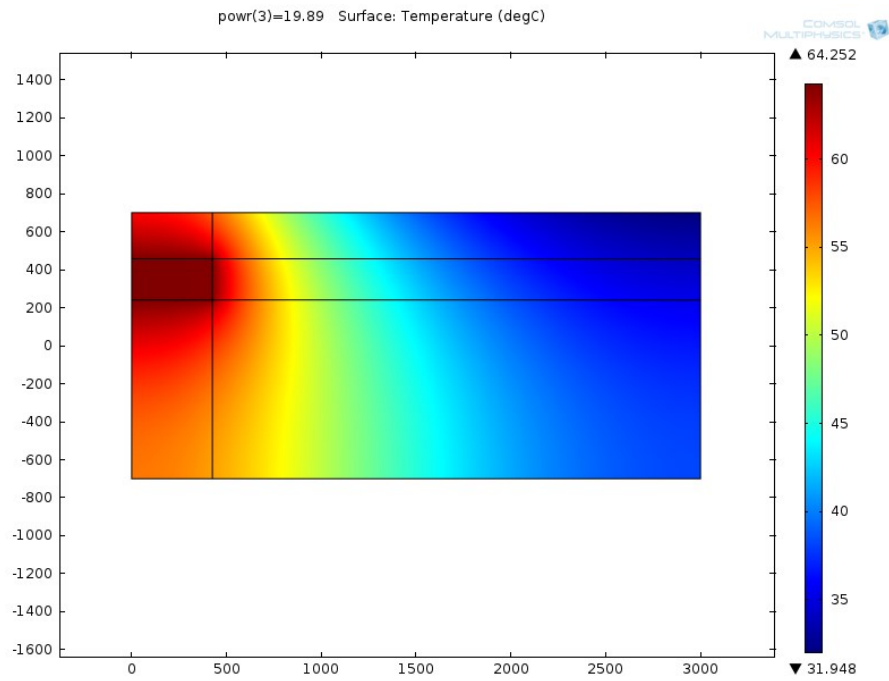


Figure 2-29: Typical finite element temperature contour plot of solution

Chapter 3 - Results

Two data sets are presented: surface temperature and de-icing time. Each set is shown in three charts: one showing the mean trend of all data for that set, one for the mean trends of the data for each heating element material, and another for the mean trends of the data with respect to LS. Trendlines are shown to demonstrate the linearity of the data or to show how it may be represented by a power function. Error bars are shown to indicate the standard deviation of the data; that is, a marker represents a mean and the error bars extend to one positive and negative standard deviation.

IWT test conditions are listed in Table 3-1 for steady-state temperature measurement and for de-icing time measurements. No icing cloud was present during the temperature measurement runs, only dry cold air.

Table 3-1: Test Conditions

Parameter	Steady Temperature Measurement	De-Icing Time
Wind Speed (m/s)	15	15
Wind Static Temperature (°C)	-10	-10
LWC (g/m ³)	-	0.5
Icing Time (minutes)	-	0.75

3.1. Dry Surface Temperature Measurements

Shown here is a chart comprised of steady-state surface temperature measurements for all samples listed in Table 2-7 and at conditions found in Table 3-1. The method of IR camera measurements and analysis are written in Sections 2.3 and 2.4 respectively. Figure 3-1 shows a strong linear relation between measured surface temperature and applied power. The chart is comprised of average values from all samples with the standard deviation marked by error bars. The standard deviations grow with the power density with the largest one at 16°C.

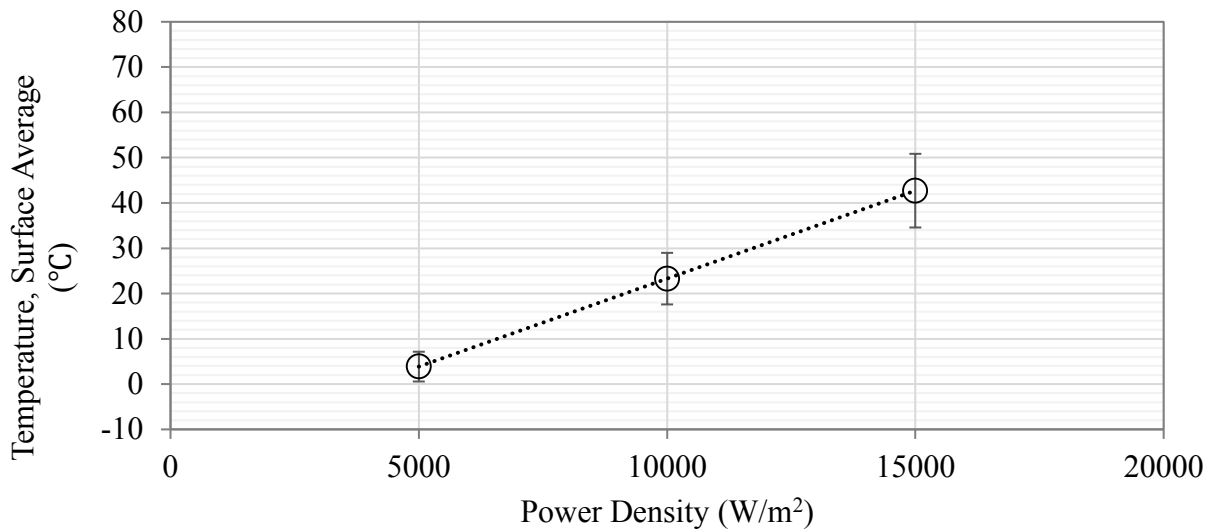


Figure 3-1: Average Temperature for all samples grouped together

3.1.1. Line Spacing Effects on Dry Surface Temperature

The average surface temperature measured by IR thermography for all heaters is shown here for the same conditions as in Table 3-1. Figure 3-2 shows average surface temperature data for all samples, grouped by common LS. The slopes of 3-mm and 6-mm LS are closer together than that of the 1.5-mm LS. The 1.5-mm LS slope is slightly steeper than that of the other two. At the highest power density, the temperatures of the 0-mm LS (continuous buckypaper film) is approximately 10°C lower than those of 6-mm and 3-mm and over 20°C lower than heaters with 1.5-mm LS.

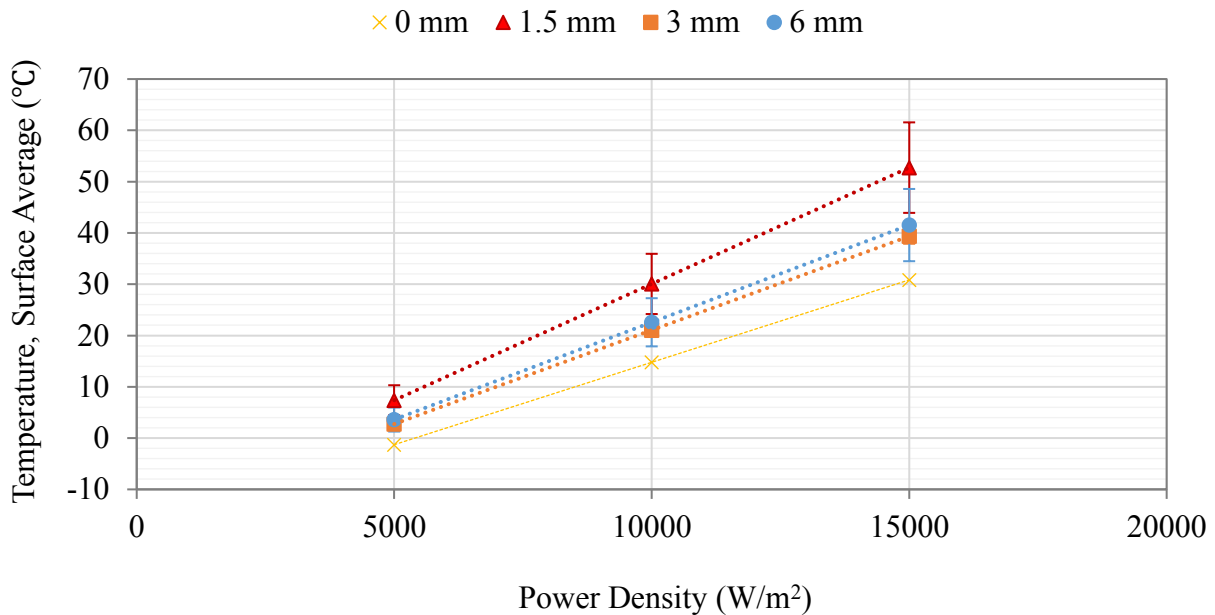


Figure 3-2: Average Temperature sorted by LS

3.1.2. Heating Element Material Effects on Dry Surface Temperature

Figure 3-3 shows the same surface temperature data as Figure 3-1 and Figure 3-2 but arranged by HE material. The spread of the averages among HE material is larger than when it was sorted by LS, which is an indication that HE material is the dominant factor in the error bar spread of Figure 3-1. Buckypaper data shows the smallest standard deviation, however it also shows the lowest slope and lowest absolute values. 1K-tow carbon fiber has the highest slope and values, followed by constantan and 3K-tow carbon fiber. If the average of the two carbon fiber samples is taken, the trend is collinear with the constantan sample. The standard deviation bars of constantan and carbon fibers are overlapping, but the buckypaper data range is outside of their range.

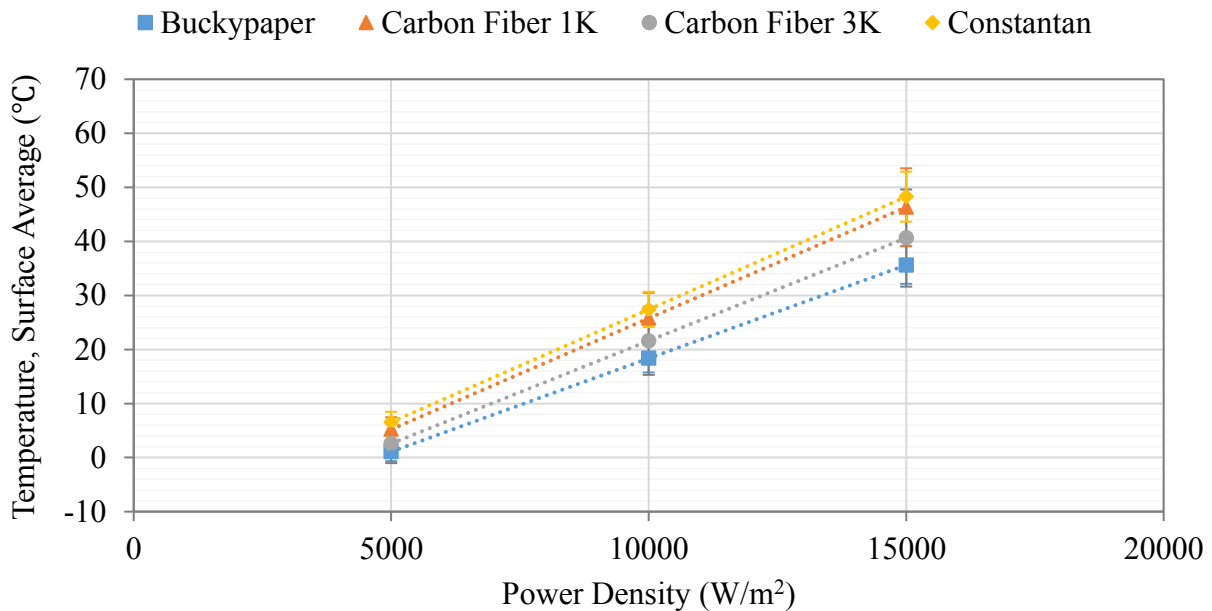


Figure 3-3: Average Temperature sorted by HE material

A 2-dimensional finite element model solved by COMSOL Multiphysics as described in Section 2.4.3 was used to model the different HE materials embedded in the glass/epoxy laminate as illustrated in Figure 2-12. Figure 3-4 shows the values of maximum temperature on the upper boundary of the finite element model domain with respect to power density supplied to the smaller domain which represented the HE. The largest difference in temperature was 10°C between constantan and buckypaper heater models at a power density of 15 kW/m².

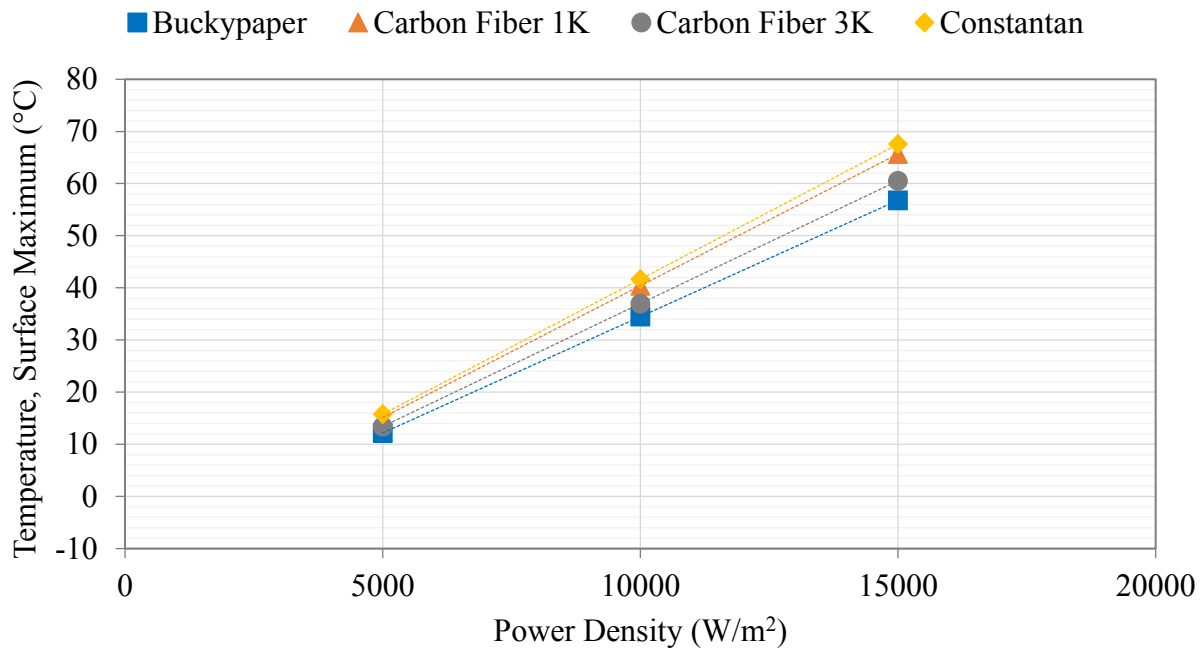


Figure 3-4: Simulation results for different material position and sizes embedded in glass/epoxy

3.1.3. Dry Surface Temperature Uniformity

Surface temperature measurements taken by IR camera while the heaters were installed in the IWT test section and subject to dry air convection at 15 m/s and -10°C show some differences in relative surface temperature uniformity. Figure 3-5 is a compilation of selected images showing the temperature uniformity of the twelve different heaters. There is a common hot-spot for all the heaters, near center-span, which is due to the magnet adhered to the back of the heater coupons for fixation to the sample holder illustrated in Figure 2-16.

Effects of Line Spacing

Comparing the columns, there is increasing temperature uniformity from left to right, that is, with decreasing LS. At the lowest line spacing (1.5 mm) the heaters with discrete lines (CF1K, CF3K, and constantan) appear to have similar uniformity to that of the continuous buckypaper film (shown at the top right of Figure 3-5). In other words, the heating lines are not distinguishable from the spacing between heating lines.

Effects of Heating Element Material

The 6-mm LS buckypaper heater appears warmer on the right side of its image. The 3-mm LS buckypaper heater has scattered cold zones. The heating lines were cut manually using scissors and their width was not completely uniform. The result of non-uniform heating line width is variable linear resistance, which results in non-uniform heating along the HE.

The CF1K HE showed no particular heating non-uniformity except for the 1.5-mm LS heater which is slightly cooler on the right side of the image. Some fiber fraying could be responsible for the slight imbalance.

The CF3K HE had more noticeable fiber fraying problems. There is a small link between the middle heating line and the bottom heating line near the mid-span of the 6-mm LS heater, which is caused by fiber fraying. Overall the impact on the 6-mm LS heater temperature uniformity was small. The problem was more noticeable in the 5-mm LS heater as the heating lines seem to

be blurred and not separate. In this case, the heating was more uniform than with the CF 1K heater.

The constantan heater showed no unexpected non-uniformity in its surface temperature. Small kinks in the HE wire are slightly visible in the 6-mm LS heater. The effect of the support magnet was more pronounced than with the other materials in the 1.5-mm LS heater.

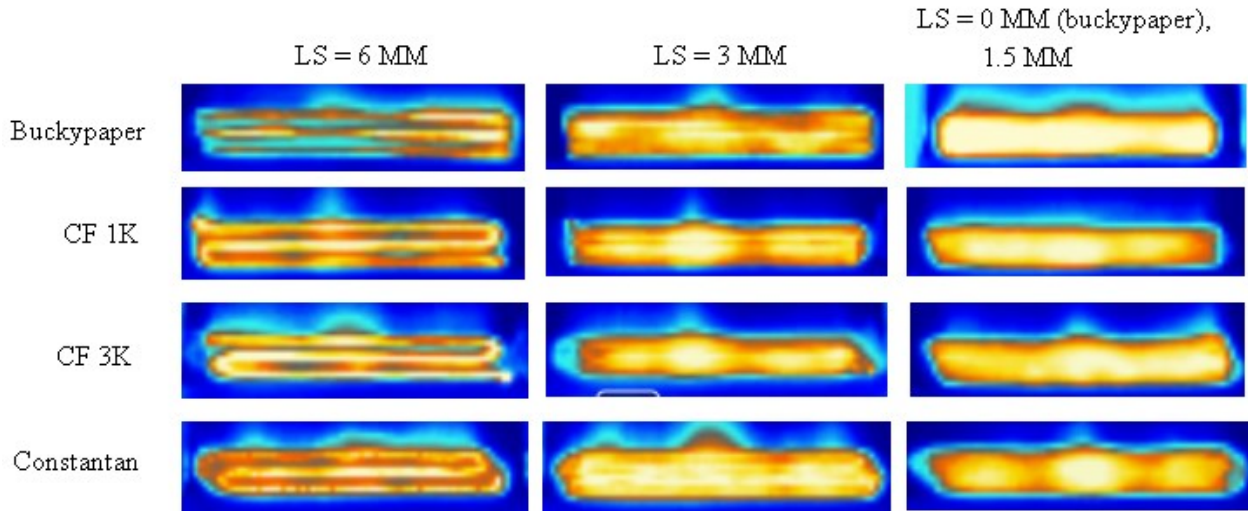


Figure 3-5: Images of energized heaters in IWT with dry wind (15 m/s, -10°C) taken by IR camera

3.2. De-Icing Time Measurements

Figure 3-6 shows that a strong correlation with a negative power function ($R^2=0.986$) exists between the de-icing time vs. electrical power curves. An almost 60% standard deviation at the low power setting suggests that the de-icing time does not only depend on applied power density, but also the material or LS of the HE.

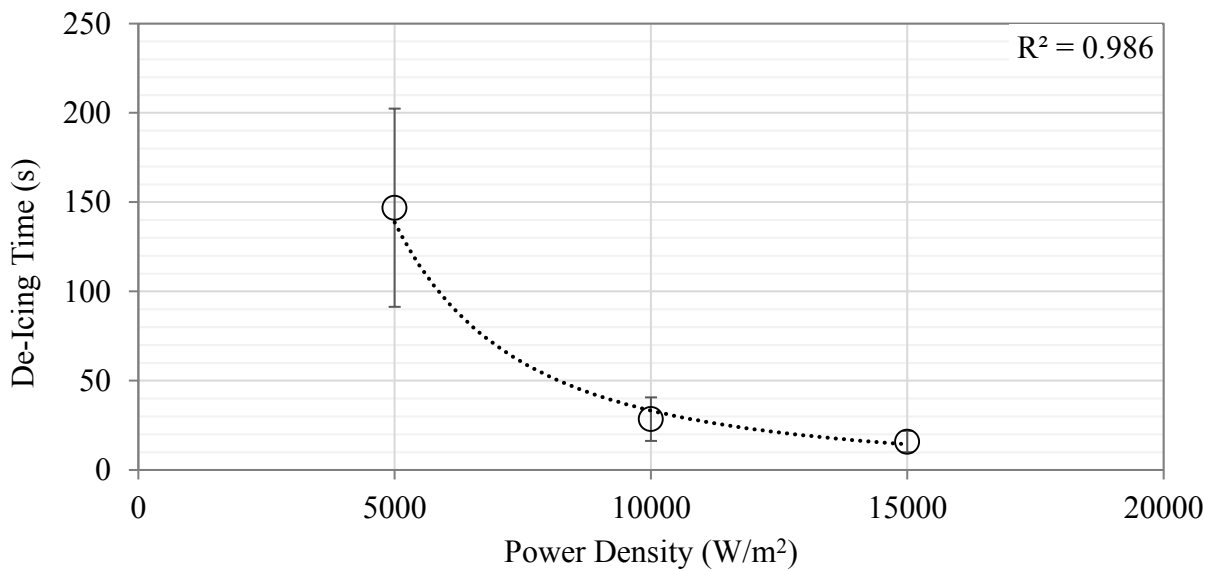


Figure 3-6: De-Icing Time for all samples grouped together

3.2.1. Line Spacing Effects on De-Icing Time

Figure 3-7 shows that for higher power densities, the practical advantage of heaters with smaller LS decreases; calling into question the importance of tight heaters for temperature uniformity. The De-icing time vs. heater power relationship depends negatively on the LS. That is, as the LS decreases, the apparent dependence of de-icing time becomes smaller. At 10 kW/m^2 , for example, the difference between 6-mm LS de-icing time and that of 3-mm LS is 15 seconds, whereas it is 10 seconds between 3-mm and 1.5-mm or 0-mm. The same is true but more pronounced for the relationship of de-icing time and power density: as the power increases, the apparent influence of density decreases. The largest difference in de-icing times between LS is 140 seconds at 5 kW/m^2 but only 12 seconds at 15 kW/m^2 . For high power settings, such as to obtain fully evaporative conditions on a slat, for example, the difference may be negligible. For low power settings, such as for running wet conditions, the difference becomes more significant. For all power densities, 1.5-mm LS can achieve a faster de-icing time than 6-mm by a factor of ~ 2 . The data for 0-mm LS and 1.5-mm LS are nearly co-linear.

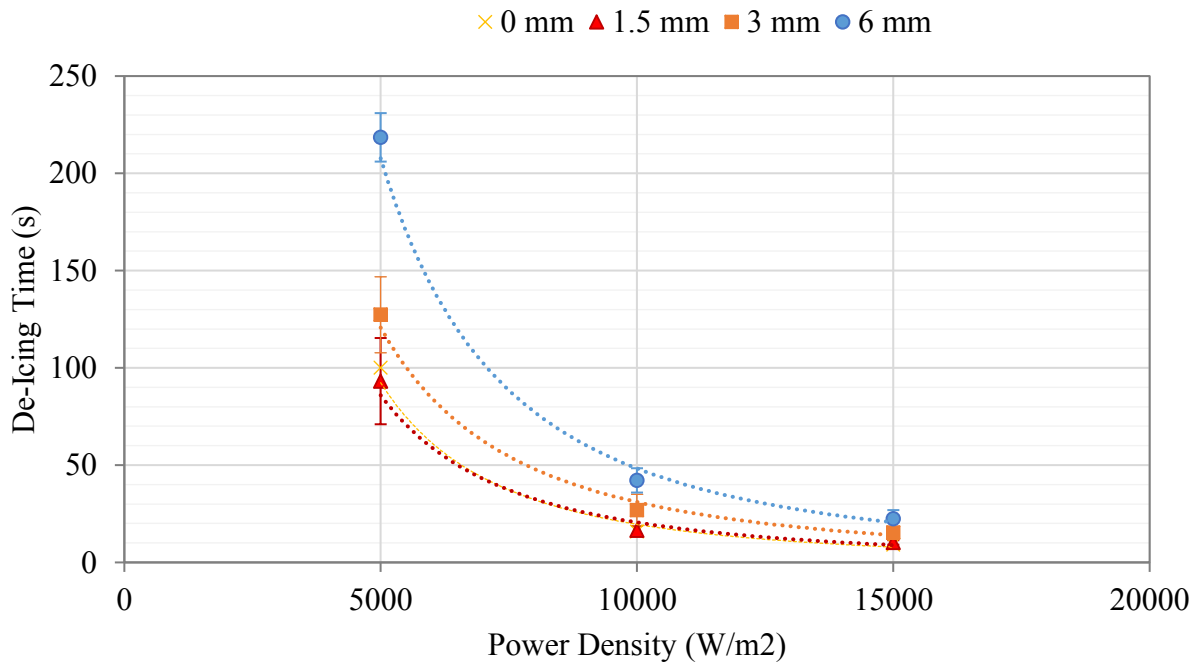


Figure 3-7: De-Icing Time grouped by LS

Finite element simulation results of the transient heat transfer problem, described in Section 2.4.3, for the heaters at different LS is shown in Figure 3-8. To obtain comparable data to that of de-icing experiments, the time for the minimum surface temperature to reach 4°C was plotted. That target temperature was chosen because it is above 0°C and because at that temperature, the time magnitudes most closely resembled that from the experiment. Differences, though, between Figure 3-7 and Figure 3-8 are in the time response of the 1.5-mm and 3-mm configurations. The simulation is almost 50 seconds faster than the experiment.

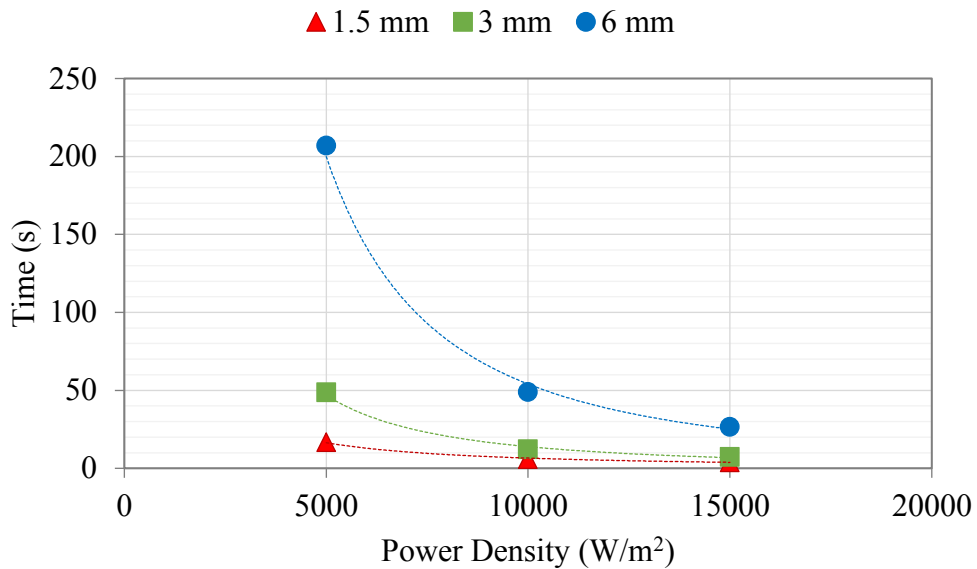


Figure 3-8: Time-dependant simulation results at different LS; times shown are the time for the minimum surface temperature to reach 4°C

3.2.2. Heating Element Material Effects on De-Icing Time

Figure 3-9 shows that HE material has little influence on de-icing time. At high and medium power densities, the 1K CF HE was the fastest, whereas the Constantan HE was fastest at 5000 W/m^2 .

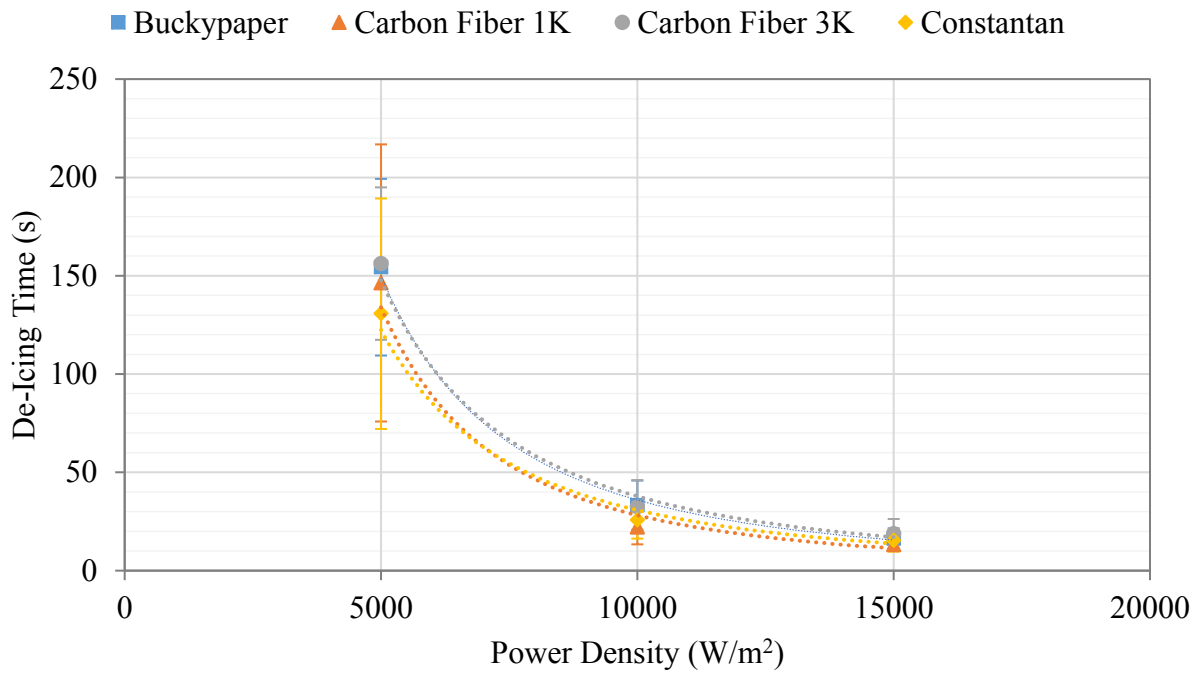


Figure 3-9: De-Icing Time vs. electrical power for the three materials used

3.2.3. De-Icing Uniformity

As heaters completed their de-icing cycle, it was apparent that the final 20% of ice would remain on specific locations of the heater surface depending on the sample itself. The locations of the 20% remaining ice were indications of cold areas on the heater surface. Figure 3-10 is a group of images organized by HE material and LS, which shows the state of the heaters with approximately 20% of the surface covered with ice. The images were taken using a portable microscope (Camera 1 from Figure 2-22 and with specifications from Table 2-6). The images presented in Figure 3-10 are those from 5 kW/m² tests because those were the slowest to complete the de-icing cycle and where temperature non-uniformity was most evident.

For buckypaper 6-mm LS, the ice present near the center heating line suggests that temperature was highest directly over the top and bottom heating line. Cold zones appeared between heating lines. The 3-mm line spacing heater also had some accumulation ice in between heating lines. Much of the ice remained on the right side of the image, meaning that there was a temperature imbalance on the heater surface. The same could be said of the continuous film heater (0-mm LS).

The 1K-tow CF heaters exhibited much of the same de-icing uniformity trends as did the buckypaper heaters. The middle line of the 6-mm LS heater was slower to melt ice than the other two lines, and the interline spacing was slowest. The slow middle line is due to thicker ice accretion near the stagnation point of the set-up, which was at the center-width of the heater. The 3-mm LS heater showed a cold region near the left side of the image, and more-so between heating lines. The 1.5-mm LS heater showed staggered cold spots which were largest near the right side of the image.

The heating uniformity 3K-tow CF heaters shown by de-icing was not far from the other HE materials. The 3-mm LS heater showed the same trend as the others with a cold region near the center-width (vertical center in the image), and between heating lines. There was no indication of span wise (horizontal in the image) bias in de-icing; apart from the center heat concentration zone where the support magnet was located. The 3-mm LS heater showed a right-side heat bias

(cold spot on the left side). The 1.5-mm LS showed a clear cold spot boundary at around 20% span length from the left of the image. This cold spot is due to fiber fraying at the left side of the heater where the tow is bent. The result is increased electrical power consumption in the frayed zone which draws heat generation away from the rest of the HE and creates surface temperature non-uniformity.

The constantan heaters generally showed span-wised uniformity except for the 3-mm LS heater, and for where the support magnet was located for all three LS. The 3-mm heater appeared to have faster de-icing on the right side of the image. Temperature imbalance on the surface of constantan heaters is believed to be due to the integration of the HE within the tows of the fiberglass fabric in which it is embedded. This concept is discussed in depth in Section 4.1.

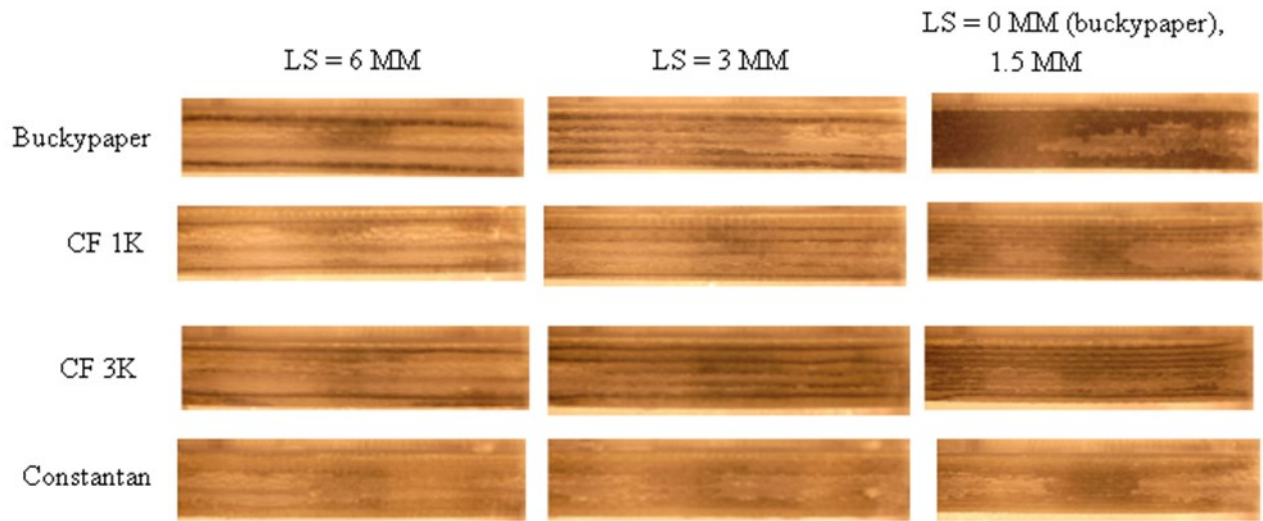


Figure 3-10: Images of heaters with approximately 20% of their original ice formation remaining (vertical dimension of heaters in images is 17 mm)

3.3. Summary of Results

Data has been presented for steady and transient behaviour of the heaters as average surface temperature and de-icing time measurements respectively. The average temperature vs. applied power density may be represented by a linear function with a positive slope, whereas the de-icing time vs. applied power density is best represented by a negative power function. Data grouped by HE material was evidence that the HE material has a stronger influence on average surface temperature than does LS. The opposite is true for de-icing time, where LS appears to have a greater influence than HE material.

Chapter 4 - Discussion

This section provides some physical interpretations of the results. The goal is to provide insight into the data shown in the previous chapter and to give some recommendations for materials selection of heating elements and for design rulers of the heaters. The results are explained in the order they were presented in the previous chapter. An analysis is then presented that takes into perspective the criteria outlined in [16].

4.1. Surface Temperature Measurements

Surface temperature measurements were performed under conditions specified in Table 3-1 by IR camera, processed using software tools described in Section 2.4.1, and presented in Figure 3-1 through Figure 3-3. The following paragraphs are explanations of the results presented in Section 3.1.

Figure 3-1 is a summary of all the average temperature data for the twelve heater samples tested (sample specifications are listed in Table 2-7), and is presented to show that the general temperature/power density relationship is linear and with a maximum standard deviation of 8 °C, or 2% of the absolute average temperature (in K). A linear relationship was expected as per Equation (2-3), which results in a constant relation between heat transfer rate, $\dot{Q}_{Convection}$, and the difference in temperature between the heater surface and that of the convective air, $T_{Surface} - T_{air}$, if the convective heat transfer coefficient, h , and surface area, A , are kept constant. In fact, the heat transfer coefficient is not exactly constant over the range of surface temperatures tested, but its variation is apparently negligible. The value of the convective heat

transfer coefficient is expected to be between that of external forced convection over a cylinder and external forced convection over a vertical flat plate, due to the aerodynamic profile over the shape shown in Figure 2-16 but with the sample surface perpendicular ($\pm 1^\circ$) to the airflow. According to the Churchill & Bernstein equations for the estimation of average convective heat transfer coefficient over a cylinder, with a diameter of 25.4 mm, air temperature of -10°C , and air speed of 15 m/s, are 443 $\text{W}/\text{m}^2\text{K}$ to 428 $\text{W}/\text{m}^2\text{K}$ for surface temperatures between -5°C and $+42^\circ\text{C}$ respectively. For a vertical flat plate of 17 mm height, those values are 2073 $\text{W}/\text{m}^2\text{K}$ to 2007 $\text{W}/\text{m}^2\text{K}$. Using Equation (4-1), which is a re-ordered version of Equation (2-3), the convective heat transfer coefficient, h , can be calculated based on the inverse of the slope of Figure 3-1 as 257 $\text{W}/\text{m}^2\text{K}$. Evidently, the analytical convective heat transfer model for this system resembles that of forced convection over a cylinder more closely than that of a vertical flat plate, however there is a difference of 41% with respect to the theoretical value. Further study would be needed to more accurately model the convective heat transfer of the system.

$$T_{surface} = \frac{1}{h}\dot{q}_{convection} + T_{air} \quad (4-1)$$

The same average surface temperature data as in Figure 3-1 is presented in Figure 3-2, but separated by LS to visualise the influence of LS on the average surface temperature of the heaters. The trendlines are all linear but not collinear, as would be expected from energy balance equations, and not parallel. The 3-mm line spacing and 6-mm are nearly collinear. The 1.5-mm LS data is at most 10°C higher than that of 3-mm and 6-mm. The reason for these higher temperature readings at lower LS is due to discretization error in the IR camera. Figure 4-1 illustrates this point by showing a comparison between the IR camera pixel resolution and the 1.5-mm heater LS as perceived by the camera at a relative angle of 40° . As viewed by the camera, 1.5-mm LS becomes 0.88 mm. With a pixel resolution of 1.69 mm/pixel, which is almost twice the size of the apparent LS, a significant amount of data, such as temperature peaks and troughs, is lost.

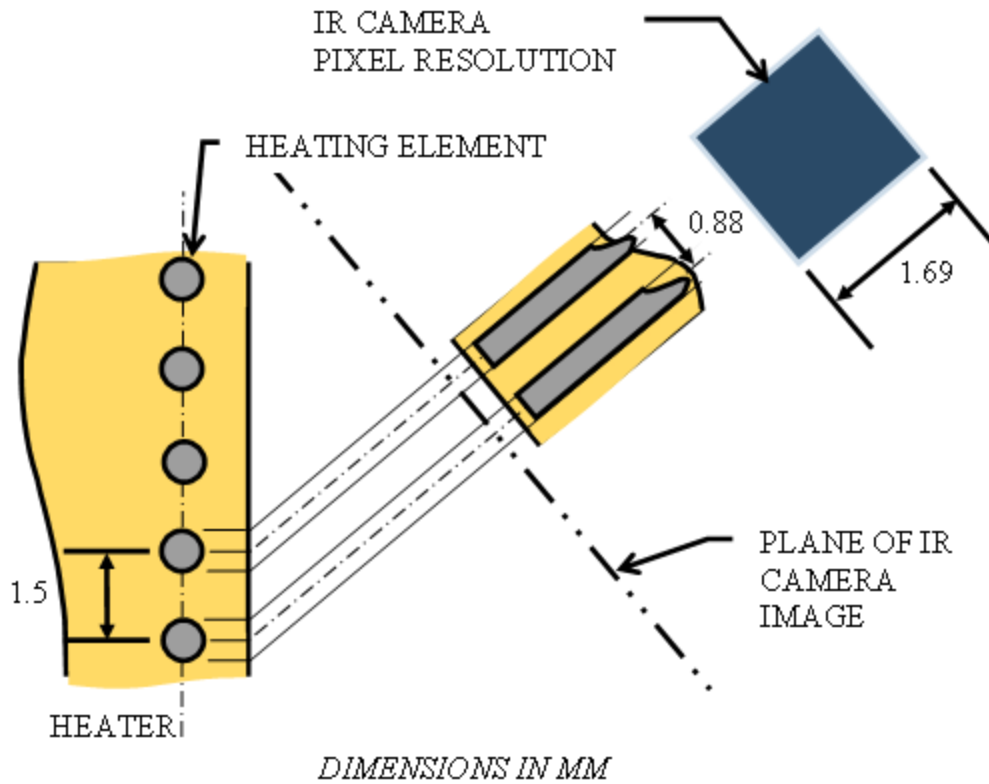


Figure 4-1: Schematic showing the apparent LS as viewed by the IR camera at an angle of 40° relative to the heater surface, and the pixel resolution size in relation to the apparent HE LS

The sensor in the IR camera is an array of uncooled microbolometers. Microbolometers are transducers whose electrical resistance changes with IR radiation absorption at a range of wavelengths. The exact response of the FLIR A320 microbolometer array is unknown but it is expected that the sensors return the maximum temperature, or close to the maximum temperature, observed in their respective resolution areas. Taking the integral average of the discretized temperature data can show a slightly higher average temperature than reality.

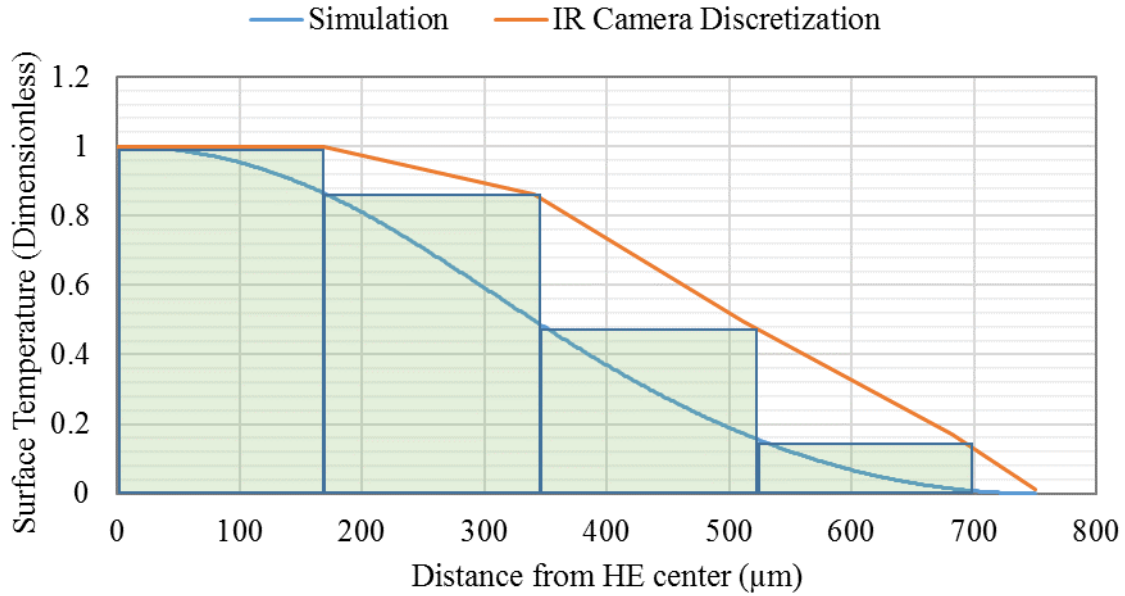


Figure 4-2: Effect of pixel discretization on average temperature measurement of 1.5-mm LS heater based on a dimensionless temperature profile from simulation data

The average temperature of the 0-mm LS heater shown in Figure 3-2 is almost 10°C lower than the 3-mm and 6-mm data at the highest power density. Pixel discretization was a concept used to explain the high temperatures observed on 1.5-mm LS heaters, but the same cannot be said of the 0-mm heater which is in fact a continuous film heater. Instead, the cause of the lower average temperatures is attributed to the cross-sectional shape and position of the heating element within the glass/epoxy composite. This concept is best described considering all the materials used in the study, and is discussed in the following paragraphs.

Although there is some overlap of the standard deviations from the average values of surface temperature in Figure 3-3, the trendlines never cross (for the range of power densities tested). The consistency of the relationship of one material to another (i.e. the 1K CF heaters always have a higher average temperature than those of the other materials over the range of power densities tested) suggests that the HE material itself has an important influence on the steady-state temperature/power relation of the heater. The question remains: what property or characteristics of the HE material affect the average temperature response. In Equation (2-2), the conduction heat transfer equation, the only material property is that of thermal conduction

coefficient, k . Heat transfer, however, happens through the surrounding structure, glass/epoxy composite, and at the interface of the structure within the HE, but not in the HE. The HE serves to generate heat, which is uniform throughout its cross-section. The HE physical properties, therefore, should not have any impact in the efficiency of steady-state heat transfer. Another difference between the heating element materials is their cross-sectional shape inside the laminate. Figure 4-3 shows optical microscope images of cross-sections of 6-mm LS heaters. Figure 4-3 (a) shows the buckypaper HE takes a rectangular shape within the laminate. Figure 4-3 (b) and (c) show the 1K and 3K CF tow HE respectively. They're cross-section shape is somewhere between oval and rectangular. Figure 4-3 (d) shows the circular cross-section of the constantan wire.

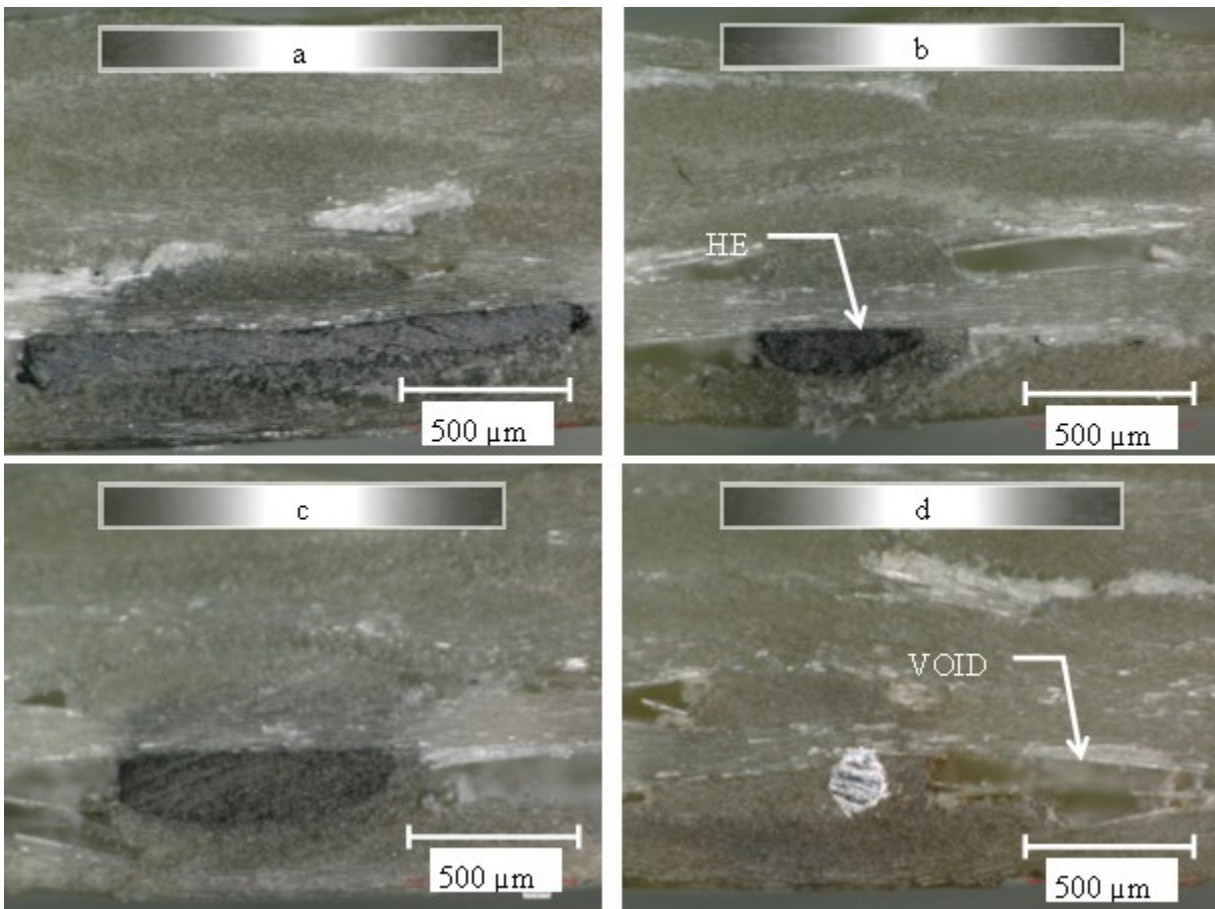


Figure 4-3: Microscope images of heater cross sections of the 6-mm LS samples with (a) buckypaper, (b) CF 1K, (c) CF 3K, and (d) constantan

The cross-section and size can also have an influence on the distance of the HE from the surface of the laminate. For example, smaller HE may penetrate between the weaves in the fiberglass fabric layers of the laminate, whereas wider HE could only sit on top of them. There also appears to be some effect on the size and distribution of voids within the laminate. Figure 4-3 (d) shows that the constantan wire, although it has penetrated the fiberglass fabric weave, has generated large voids along its length. To verify the effect of shape and position within the laminate, the cross-section images were used as input for a finite element simulation. Figure 4-4 is a schematic showing which dimensions were taken, and is shown as an aid to complement Table 4-1, which is a tabulation of the measurements. The area of the HE was measured by calculating the area of a freeform shape surrounding the HE. $D_{\text{equivalent}}$ is the diameter of a circle having the same cross-section area as what was measured for each heater. The CSF was calculated based on $D_{\text{equivalent}}$ and Z . The thermal conduction resistance, R_{thermal} , was calculated as the inverse of the product CSF and the thermal conductivity of the glass/epoxy composite.

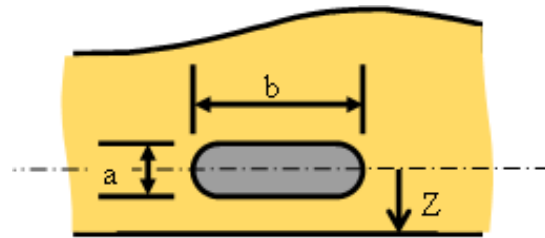


Figure 4-4: Illustration of heater cross-section optical microscope images with (a) HE thickness, (b) HE width, and (Z) distance from HE mid-thickness to surface of laminate

Table 4-1: HE measurements taken from microscope images of heater cross-sections

Parameter	Buckypaper	CF 1K	CF 3K	Constantan
a (μm)	88	127	216	170
b (μm)	1,636	484	851	182
Z (μm)	260	235	351	264
Area (μm^2)	166,753	52,298	164,284	23,773
$D_{\text{equivalent}}$ (μm)	326	182	323	123
CSF (m)	1.646	0.858	0.948	0.654
R_{thermal} ($^{\circ}\text{C}/\text{W}$)	5.416	3.837	4.276	2.922

The entries of Table 4-1 were used as input into the two-dimensional heat transfer simulation and the results are presented in Figure 3-4, which may be compared to Figure 3-3. The relative surface temperature of each material in the simulation is the same as that seen in the experiment using an IR camera; meaning that constantan wire has the highest temperature, followed by 1K CF, then 3K CF, and finally buckypaper. According to this result, it could be concluded that the influence of shape factor is responsible for the different temperature/power ratio seen in different materials in this study. As shown in Figure 4-5, the influence of shape factor or thermal conduction resistance can be modeled with reasonable accuracy. In particular, the change in slope between the two middle values is also reproducible by simulation. The change in slope is believed to be because of the rectangular HE cross-section (thickness to width aspect ratio).

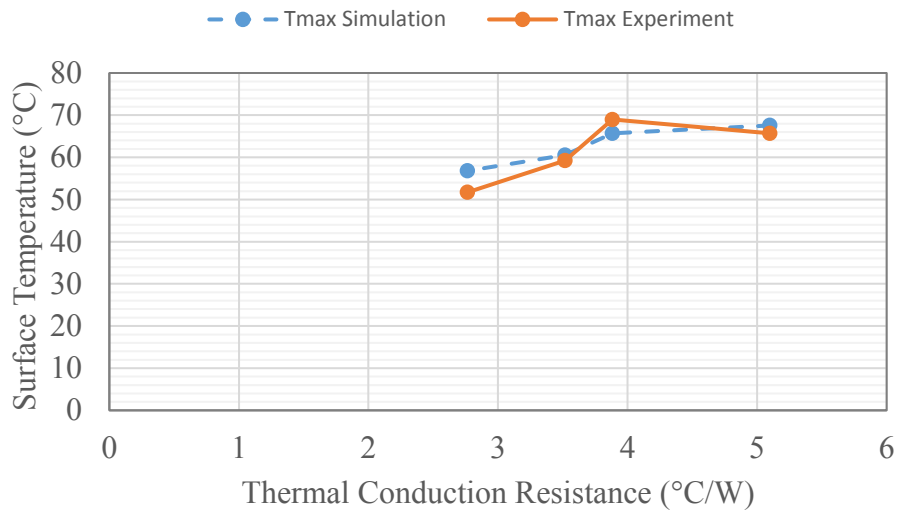


Figure 4-5: Comparison of maximum surface temperature from simulation with experimental measurements with respect to the calculated thermal conduction resistance of each HE

4.2. De-Icing Time Measurements

De-icing time measurements were performed under conditions specified in Table 3-1 with the help of optical cameras, processed using software tools described in Section 2.4.2, and presented in Figure 3-6 through Figure 3-9. The following paragraphs are explanations of the results presented in Section 3.2.

The de-icing time data for all 12 samples, shown in Figure 3-6, reveals a power function trend with an R^2 value of 0.986, with respect to electrical power density. The trend is in agreement with expected results for the time for a body to reach a certain temperature depending on the magnitude of heat generation within the body. The time dependant heat conduction equation may be solved analytically, however the temperature within the body is not uniform, nor is the heat generation, which is concentrated at the HE. Therefore, a finite element simulation is needed to solve the equation with respect to both space and time. The standard deviation decreases significantly with increasing power density; from ± 50 seconds at 5 kW/m^2 to ± 2 seconds at 15 kW/m^2 . Evidently, the de-icing time depends on more than just the power density, however, the effect of other factors becomes overshadowed by high power densities.

The difference between data series in Figure 3-7 and Figure 3-8 is evidence to suggest that LS is one of the dominant factors in de-icing time. This result can be explained by there being more thermally insulating material between HE, hence a longer distance for heat to travel before heating the surface. The maximum temperature of on the surface of the heater is always just directly above the HE, intuitively. De-icing time is more influenced by the minimum surface temperature than the maximum one. Ice located between HE was always the last to melt. The space between heating elements is also the location for which heat must travel the longest. To summarize, the reason that LS is such an important factor in de-icing time is because the minimum surface temperature evolution dictates the de-icing time. This conclusion may not be surprising to the reader, but it is useful to validate the data and to compare the influence of LS with that of HE material.

HE materials are compared in Figure 3-9. The magnitude of de-icing time difference between the different materials is less than that between different LS. These results are in agreement with those found during the surface temperature measurements shown in Figure 3-3. The heaters showing lower average temperatures in the temperature measurement experiment were the ones that showed longer de-icing times. This result is evidence to suggest that the same shape factor differences observed for temperature measurement are useful for predicting the transient response of the heaters, and hence, their effectiveness for de-icing. The results for 1K CF and constantan wire HE are spaced closely together such that they may be considered as exhibiting the same response.

4.3. Evaluation of Heating Element Materials

During the design of an advanced electrothermal IPS, criteria had been considered for a successful material selection [16]. These criteria are used here as a guideline for evaluating the different properties of the heating elements. Where possible, results generated by experiments during this thesis are used to justify the points discussed.

4.3.1. Thermal Efficiency

Results show that for a given electrical input power the heating elements reach the same average temperature, regardless of the material composition of the heating element. Thermal efficiency, as defined by [16], refers to the possibility of placing the heating elements as close to the erosion shield as possible. In the perspective of this study, thermal efficiency would refer to how close the elements may be to the surface of the supporting glass/epoxy laminate. In addition, the cross-section area of the laminate also plays a role in thermal efficiency. Even though the same fabrication process was used for all the HE materials, from pre-form fabrication to curing, Figure 4-3 and Table 4-1 illustrate how the exact configuration of the HE within the glass/epoxy laminate can vary among HE materials.

Buckypaper HE generally had a larger cross-section area than the other HE materials, with a rather large width (greater than 1 mm). This shape resulted in spreading of the heat generation, and the longest distance from the surface of the HE to the surface of the heater. CSF calculations account for the distance between the center of the HE to the surface of the embedding material, however, it is limited to cases where the Z distance is greater than 1.5 times the diameter of the HE. For the configuration used in this study, the size of the HE often exceeds the Z distance, and for this reason it is believed that the surface-to-surface distance (Z minus a from Figure 4-4) is the more important variable. Due to the buckypaper film's or strip's large width with respect to the glass fiber fabric tow, the buckypaper does not penetrate into the tow. For this reason, the thermal resistance is slightly higher than for narrower heaters and the thermal efficiency is slightly lower. Buckypaper heaters have shown slightly longer de-icing times.

Heaters made using 1K-tow CF had some of the highest thermal efficiencies. The 1K tow was smaller than the 3K fiberglass fabric tow and therefore was able to integrate into the fiberglass fabric fairly well.

Heaters made using 3K-tow CF were less efficient than those made with 1K-tow. The large tow bundles behaved more closely to buckypaper strips because of their large width.

Heaters made using constantan wire were most efficient, and were matched with 1K-tow CF HE in some cases. The diameter of the wire was less than the width of the 3K-tow fiberglass fabric. Constantan wire was fully dense and did not deform under the pressure of vacuum during curing. As such, constantan wires could partially pass through some glass filaments and sit within the fiberglass tows. The resulting distance between the surface of the constantan wire and the composite surface was less than with the other HE materials.

In summary, the order of preference of the different materials in terms of thermal efficiency of a HE inside a 3K-tow plain weave glass/epoxy composite are:

1. Constantan wire (0.127 mm diameter),
2. 1K carbon fiber tow,
3. 3K carbon fiber tow, and
4. Buckypaper (MWCNT network sheet).

4.3.2. Temperature Uniformity

Thermal efficiency effects impacted temperature uniformity. Due to vacuum pressure during curing HE would follow the physical waviness of woven fiberglass fabric. Those HE with larger widths were less susceptible to such waviness, however those with widths less than that of the fiberglass fabric tows were more sensitive to the weave pattern. Temperature non-uniformity was apparent in some heaters due to this waviness.

The best heating uniformity came from the continuous buckypaper heater. The film heater exhibited relatively uniform heating, in contrast to the periodic temperature peaks shown by wire heaters. The opposite was true for buckypaper strip heaters whose width was not as well controlled as the CF tow or constantan wire HE. The width of the buckypaper strips was not constant along the length of the strip (± 0.15 mm). Zones of smaller width had higher local electrical resistance and appeared as heat concentration zones (Figure 3-5). The difference in temperature between warm and cold zones depended on the total power delivered to the system. The temperature bias was not noticeable during de-icing tests (Figure 3-10), however.

With a smaller width than buckypaper film and strips, 1K-tow CF HE had a smaller area footprint on the surface of the heater laminate. Thus, the unprotected areas were larger and more apparent during de-icing. With smaller LS, however, the CF-1K heater's surface temperature map was not distinguishable from that of the continuous buckypaper film.

Although 3K-tow CF HE had a larger width than the 1K-tow and resembled buckypaper strips more closely, they had the problem of fiber fraying, especially at small LS. The smaller the LS, the smaller the corner radius at the borders of the heater, and therefore the higher bending stress applied to the tow. Carbon fibers are relatively brittle in bending. Their low strain to failure means that filaments on the outer radius of a tight bend may fracture and stick out. When two bends are close together, this causes electrical bridging and draws power away from the rest of the HE. Extra embroidering had been used on the bends during preform fabrication, however, some microscopic filaments had remained unconsolidated. It is therefore not recommended to use 3K-tow CF heating elements at 1.5-mm LS when a single continuous HE is required. It is

expected that an embroidered parallel circuit arrangement, where bends in the HE could be avoided, would solve the fraying problem entirely.

The most electrically stable material, in terms of diameter and electrical resistance, was the constantan wire. These metal wires typically have a precisely controlled manufacturing process with a tight tolerance on the wire diameter. Constantan is also a reputedly temperature-stable material. Constantan is the most ductile material used in this study and could bend over small radii without measurable hindrance, as opposed to 3K-tow CF. In fact, the only limitation to the minimum LS for the constantan wire was the tow size of the supporting glass fiber fabric. With a 1K fiber glass fabric as the base, it is expected that lower LS could be successfully achieved with the constantan wire used in this study. It is also expected that a smaller fiberglass fabric tow would result in reduced HE waviness, and increased temperature uniformity along the length of the HE.

4.3.3. Comments on Repairability

One of the critical criteria for a heating element, as stated by [16], is the repairability in case of localised damage or failure. An open circuit may occur in cases where the heater has sustained extensive impact from foreign objects, or if it has been bent beyond its mechanical strength.

In the present study, some of the elements were damaged during the cutting process. Three samples were cured on the same fiberglass sheet and they needed to be cut to size using a diamond circular saw (see Section 2.2). In some cases, the heating elements that extended outside the 17-mm width were cut by the saw. The areas that were most prone to this sort of damage were at the ends of the heating element, between the heated area and where it joined the copper contact. Repairability had been defined with the goal of creating a by-pass conductor of the same resistance as the heating element, such as to create an almost seamless repair. In this case, silver epoxy was used to join the two ends that were cut. The only element in this case that could be repaired homogeneously (with the same material) was the Constantan wire, in theory. Neither of the other materials, carbon fiber nor buckypaper, can be soldered or grafted together

easily. A process could be developed were carbon fibers or buckypaper were laid across the open circuit, wetted with epoxy, and cured; but it would be difficult to achieve low contact resistance. In any case the exposed area of constantan wire was so small (0.25 mm diameter cross section), soldering would have been impractical as well. The use of silver epoxy closed the circuit but created a discontinuity in the heated path. In the end, perfect repairability of a wire embedded in glass/epoxy is highly challenging, however functional repairability is feasible.

Wires embedded in glass/epoxy have the characteristic disadvantage of poor repairability. If a wire is damaged within the embedding glass/epoxy, it is impossible to reach it without causing some peripheral damage to the rest of the heater. Therein lies the practicality of coupon sized composite heaters. Consider, for example, two aircraft propeller blades each with an electrothermal ice protection system. One of the blades is equipped with a single composite heater, and the other with a series of smaller heaters connected together. Now consider the case where both the heaters sustain some localised impact damage such that the underlying HE is broken. Wire embedded in glass/epoxy heaters are virtually irreparable so therefore they must be replaced. The propeller with a single composite heater must receive an entirely new heater and will be out of service until that heater is installed. The second propeller with the modular composite heaters needs only a portion of the heater assembly replaced. The damaged coupon-sized heater may be removed and/or bypassed such that the blade will still be mostly protected.

4.4. Recommended Applications

Considering the criteria for a successful electrothermal icing protection heating element discussed in Section 4.3, some recommended applications are given specific to the heating element materials. As a metric to compare the approximate cost of each HE material, the cost of the material required to cover a 1 m x 1 m composite plate are shown below. For the buckypaper heater, a single continuous piece was assumed. The supplier used as reference produces 0.305 m x 0.305 m sheets of buckypaper. Scaling of the production process of carbon nanotube buckypaper is not trivial, and therefore it may not be realistic to expect a continuous 1 m² sheet.

With this size limitation, joining of the sheets is a necessary consideration, especially since their surface resistivity is on the order of $0.5 \Omega/\text{square}$. Care would need to be taken to ensure the interfacial resistance between buckypaper sheets and electrical joining medium is a few orders of magnitude lower than the total resistance of the sheets. The importance of electrical contact is more important for buckypaper film than for wire HE because there would be at least 11 times more contact areas in the circuit, whereas wires could continuously cover the entire span of the heater square. Epoxy with silver particles such as was used in this study would be a suitable candidate to obtain low-resistance contacts. For a wire HE, such as CF and constantan, a line spacing of 1.5 mm was assumed since it was the smallest practical line spacing achievable during this study. To cover a square of 1 m^2 , with one line spacing length between the edge of the square and the first and last HE line, a HE wire length of approximately 670 m would be required. The unit costs of CF and constantan shown in *Table 4-2* were calculated using the cost of a spool of that material divided by the length of material on that spool. The total cost is the unit cost multiplied by the length of material required, without regard for the number of spools required. For simplicity, it was assumed that there would be no high-volume discount as is often the case in practice.

Table 4-2: Estimated cost of HE made from buckypaper, CF, or constantan wire for a heater of 1 m x 1 m

Material	Unit Cost (CAD)	Quantity Required	Total Cost (CAD)	Total Mass (g)
MWCNT Buckypaper	\$1,650 / m^2 [66]	1 m^2	\$1,650	20-45
CF 1K Tow	\$0.29 / m [67]	670 m	\$262	44
CF 3K Tow	\$0.23 / m [67]	670 m	\$203	132
Constantan (0.127 mm)	\$0.83 / m [68]	670 m	\$738	75
Constantan (0.381 mm)	\$0.48 / m [68]	670 m	\$430	675

For the case of the 1 m x 1 m heater square, the costliest HE is that made from commercially available buckypaper. The least costly are the CF tows, with the 3K CF tow slightly less

expensive than the 1K. The cost of a constantan HE is closer to that of CF than to buckypaper even though it is approximately twice the cost of CF. In terms of cost, CF is the preferred HE. For low budget applications, such as hobby projects, student projects, and early prototypes, the costs quoted in Table 4-2 could be the dominant factor in a materials selection matrix. For large budget projects, such as in aircraft and wind turbine production, high costs could be justified by other factors entailed by the HE material. Such other factors are discussed below.

Chapter 5 - Conclusion and Outlook

For aerodynamic applications, such as airplanes, helicopters, and wind turbine blades, ice formation is an undesirable occurrence. Thermal ice protection systems exist for the mitigation of ice formation, and are sometimes the most reliable type of system. For composite structures, which are commonly used in aerodynamic applications because of their high strength-to-weight ratio, thermal ice protection systems must be carefully designed to remain within the structure's thermal capabilities. Part of the design is the selection of heating element material. Many studies have proposed novel heating element materials, but those materials have not been systematically compared until now.

Four heating element materials – buckypaper, 1K-tow carbon fiber, 3K-tow carbon fiber, and constantan – were embedded into a glass/epoxy laminated and tested as heaters in a small-scale icing wind tunnel. The thermal efficiency of the four heating element materials was evaluated based on infrared images and de-icing images. The most thermally efficient heating element material was constantan wire, followed closely by 1K-tow carbon fiber. The reason for their slightly superior performance was their proximity to the surface of the laminate by their integration into the embedding glass fiber fabric. This claim was validated using a two-dimensional finite element simulation where the heating element's position and size were taken from measurements of microscope images of heater cross-sections. The maximum temperature versus input power trend obtained from simulation matched that of the experimental infrared images.

Heating uniformity was also evaluated using infrared images of energized heaters and de-icing experiment images. The heaters with the best temperature uniformity were those with the lowest line spacing. The 1.5-mm line spacing heater's performance was almost identical to the

continuous buckypaper film. The significance of this result is that a continuous film is not necessarily required for uniform heating, and that for electrothermal icing protection systems, wires with small enough line spacing could yield the same uniformity.

The heaters with the shortest de-icing times were constantan and 1K carbon fiber tow, followed by 3K carbon fiber tow, and finally carbon nanotube buckypaper, however they were all within a few seconds of each other. It has therefore been determined that the development of new heating element materials should be for improved cost, corrosion properties, and mechanical properties such as impact resistance, ductility, and possibly erosion resistance.

Mechanical testing should be done to study the different impact behaviors of the laminated heaters. As reported in [16], when an electrothermal IPS' erosion shield has failed, the heating system is prone to failure soon thereafter. It is therefore desirable to have an impact-resistant heating element such that it may withstand such forces even after the erosion shield has been damaged. In addition, an investigation should be carried out into the effect of the tension applied by the sewing thread onto the heating element and the resulting void content of the laminate, and whether it has any impact on the mechanical durability of the heater. Finally, a standard method should be developed for mechanical testing of the different heating element materials.

Chapter 6 - Contributions

Testing Procedure

- Developed a process for the systematic comparison of thermal efficiency and surface temperature uniformity of wire or film heating element materials embedded in glass/epoxy.
 - Novel heating elements presented in literature have been tested under different icing conditions and embedded in different structures such that their performance was impossible to compare. In this study, various heating elements were embedded and tested using one universal procedure. They were then tested in an IWT with a set of controlled and repeatable testing conditions, making it possible to compare their de-icing performance.
 - The process parameters for repeatable rime ice formations in the Concordia University Icing Wind Tunnel are: test section air static temperature of $-10\text{ }^{\circ}\text{C}$, test section air speed of 15 m/s, nozzle air flow rate of 171317 cubic centimeters per minute (6.05 standard cubic feet per minute), and water flow rate of 10 cubic centimeters per minute. These conditions produce repeatable rime ice in the test section and without excessive ice buildup on the test section walls.

Sample Design

- For the first time, an embroidered heating element has been presented for application as an electrothermal ice protection system.
- Developed a design for durable coupon-sized flat plate glass/epoxy composite heaters for small-scale icing wind tunnel testing.

- The most basic composite structure is a coupon-size flat plate, yet the fabrication of such is not trivial when embedding foreign materials for multi-functionality. In this study, a method has been presented where an embroidered heating element preform is integrated into a plain weave fiberglass fabric layup, and where a conductor makes electrical contact with the heating element between the layers of glass fabric, and where the conductors pass through the thickness of the laminate to be soldered to larger current-carrying conductors. The durability of the flat plate coupons refers to that of the electrical contacts on the exterior surface of the composite, which are exposed to sub-zero temperatures, wind, and freezing water. The flat plate coupons in this study retained their functionality throughout testing, which had not been the case in a previous study [61].
- For the first time, the minimum line spacing of a carbon fiber tow heating element was shown to be limited because of filament bridging between heating lines.

Findings Obtained from Results of Testing Procedure

- The thermal efficiency and temperature of different heating element materials is the same.
 - This finding means that embroidering of a heating element is a viable heater fabrication process and it can be used in lieu of thermal spray or other more complex processes.
 - It also shows that low cost heating element materials can be used instead of carbon nanotube (CNT). When presented in literature, CNT/epoxy or glass/epoxy/CNT are shown to have great promise as the next-generation of heating elements. This study found that CNT prepared as a buckypaper do not show any indication of shorter de-icing time compared to other HE; in fact, the de-icing time of heaters made with a buckypaper heating element exhibited slightly longer de-icing times, and therefore less favorable performance.
 - The de-icing time was the same for constantan wire and for 1K-tow carbon fiber. These heating elements can therefore be used interchangeably.

- The shape and position that heating elements take within their embedding glass/epoxy structure can influence the overall heater performance slightly.
- The surface temperature uniformity obtained by a film heating element can be matched by a wire heating element with sufficiently small LS.
 - Theoretically the temperature uniformity of a continuous film heating element is the best achievable, however for practical ice protection purposes, it has been shown in this study that a wire heating element with sufficiently small line spacing can achieve the same temperature uniformity.

Chapter 7 - References

- [1] National Transportation Safety Board, "CHI07FA183," 2009.
- [2] Bureau d'Enquêtes et d'Analyses pour la sécurité de l'aviation civile, "Final Report," Ministère de l'Écologie, du Développement durable, des Transports et du Logement, 2012.
- [3] S. M. Jones, M. S. Reveley, J. K. Evans and A. F. Barrientos, "Subsonic Aircraft Safety Icing Study," National Aeronautics and Space Administration, Hampton, 2008.
- [4] H. J. E. Addy, M. G. Potapczuk and D. W. Sheldon, "Modern Airfoil Ice Accretions," in *35th Aerospace Sciences Meeting & Exhibit*, Reno, 1997.
- [5] H. Seifert and F. Richert, "Aerodynamics of Iced Airfoils and Their Influence on Loads and Power Production," in *European Wind Energy Conference*, Dublin, 1997.
- [6] R. J. Flemming, R. K. Britton and T. H. Bond, "Model Rotor Icing Tests in the NASA Lewis Icing Research Tunnel," National Aeronautics and Space Administration, Ohio, 1986.
- [7] H. Seifert, "Technical Requirements for Rotor Blades Operating in Cold Climate," DEWI.

- [8] A. Heinrich, R. Ross, G. Zumwalt, J. Provorse, V. Padmanabhan, J. Thompson and J. Riley, "Aircraft Icing Handbook - Volume 2 of 3," National Technical Information Service, Springfield, 1991.
- [9] Transportation Safety Board of Canada, "Aviation Investigation Report A14W0181 - Severe Icing Encounter and Forced Landing," Transportation Safety Board of Canada, Gatineau, 2016.
- [10] G. N. Labeas, I. D. Diamantakos and M. M. Sunaric, "Simulation of the Electroimpulse De-Icing Process of Aircraft Wings," *Journal of Aircraft*, vol. 43, no. 6, pp. 1876-1885, 2006.
- [11] K. Al-Khalil, "Thermo-Mechanical Expulsion Deicing System - TMEDS," in *45th AIAA Aerospace Sciences Meeting and Exhibit*, Reno, 2007.
- [12] D. L. Kohlmann, W. G. Schweikhard and P. Evanich, "Icing-Tunnel Tests of a Glycol-Exuding, Porous Leading-Edge Ice Protection System," *Journal of Aircraft*, vol. 19, no. 8, pp. 647-654, 1982.
- [13] B. E. Humphreys and K.-H. Horstman, "Flight Testing of a HLF Wing with Suction, Ice-Protection and Anti-Contamination Systems," in *Aerodynamic Drag Reduction Technologies*, Berlin, 2001.
- [14] F. Zandman, P.-R. Simon and J. Szwarc, *Resistor Theory and Technology*, Park Ridge: SciTech Pub, 2002.
- [15] Federal Aviation Administration, "Type Certificate Data Sheet Number E28NE Revision 6," U.S. Department of Transportation, 1998.

- [16] J. B. Werner, "The Development of an Advanced Anti-Icing/Deicing Capability U.S. Army Helicopters. Volume I. Design Criteria and Technology Considerations," National Technical Information Service , Springfield, 1975.
- [17] J. L. Palacios, "Design, Fabrication, and Testing of an Ultrasonic De-Icing System for Helicopter Rotor Blades," The Pennsylvania State University, State College, 2008.
- [18] P. J. Walsh, "Carbon Fibers," in *ASM Handbook, Volume 21, Composites*, ASM International, 2001, pp. 35-40.
- [19] F. T. Wallenberger, J. C. Watson and H. Li, "Glass Fibers," in *ASM Handbook, Volume 21, Composites*, ASM International, 2001, pp. 27-34.
- [20] M. A. Boyle, C. J. Martin and J. D. Neuner, "Epoxy Resins," in *ASM Handbook, Volume 21, Composites*, ASM International, 2001, pp. 78-89.
- [21] T. Pepper, "Polyester Resins," in *ASM Handbook, Volume 21, Composites*, ASM International, 2001, pp. 90-96.
- [22] D. A. Scola, "Polyimide Resins," in *ASM Handbook, Volume 21, Composites*, ASM International, 2001, pp. 105-119.
- [23] S. V. Hoa, *Principles of the Manufacturing of Composite Materials*, Lancaster: DEStech Publications, 2009.
- [24] R. D. Salway Crick and S. T. Jelly, "Electrical De-Icing or Anti-Icing Apparatus". Great Britain Patent 833,675, 27 April 1960.

- [25] A. J. Bruce, M. Cyrus and S. Frolov, "Multi-Layer De-Icing Skin for Aircraft Platforms". World Intellectual Property Organization Patent WO 2015/116265 A1, 6 August 2015.
- [26] A. G. Farries, "Improvements in or relating to Electrical Surface Heating Apparatus". Great Britain Patent 740,551, 16 November 1955.
- [27] M. J. Heseltine, "Aircraft De-Icing Apparatus". United Kingdom Patent GB 2 121 745 A, 17 June 1984.
- [28] C. D. Lawson and G. E. Wiese, "An Electrically Conductive Composite Heater and Method of Manufacture". World Intellectual Property Organization Patent WO 95/15670, 8 June 1995.
- [29] R. B. Rutherford, "De-ice and anti-ice system and method for aircraft surfaces". United States of America Patent 6,194,685 B1, 27 February 2001.
- [30] A. E. Bardwell, M. E. Brown and P. Nicklin, "Heating System for Leading Edge of Aircraft". Great Britain Patent GB 2 438 389 A, 28 November 2007.
- [31] A. Bardwell, "A Method of Making a Heater Structure and a Heater Structure". World Intellectual Property Organization Patent WO 2007/107713 A1, 27 September 2007.
- [32] J. W. Atkinson, "Mounting an Aircraft Leading Edge Ice Protection System". Great Britain Patent GB 2 453 769 A, 22 April 2009.
- [33] D. J. Armstrong, G. R. Pringle and M. E. Brown, "Aircraft Wing Slat". Europe Patent EP 1 757 519 B1, 10 March 2010.

- [34] P. Ténèbre, M. Dieudonne and C. Ross, "Système d'antigivrage/dégivrage, son procédé de fabrication et structure d'aéronef l'incorporant". European Patent Patent 2 196 393 A1, 16 June 2010.
- [35] D. P. Calder, J. A. Opificius, E. Pederson and D. C. Flosdorf, "Aircraft Ice Protection System and Method". Great Britain Patent 2505994 A, 19 March 2014.
- [36] D. Aliaga, M.-P. Guillou, E. Campazzi and T. Navarre, "Nappe de protection de bords d'attaque d'éléments de voilures d'aéronefs". Europe Patent 2 915 743 A1, 9 September 2015.
- [37] D. Janas and K. K. Koziol, "Rapid Electrothermal Response of High-Temperature Carbon Nanotube Film Heaters," *Carbon*, vol. 59, pp. 457-463, 2013.
- [38] C.-C. Hung, M. E. Dillehay and M. Stahl, "A Heater Made from Graphite Composite Material for Potential Deicing Application," *Journal of Aircraft*, vol. 24, no. 10, pp. 725-730, 1987.
- [39] T. Kim and D. Chung, "Carbon Fiber Mats as Resistive Heating Elements," *Carbon*, vol. 41, pp. 2427-2451, 2003.
- [40] D. Chung, "Self-Heating Structural Materials," *Smart Materials and Structures*, vol. 13, pp. 562-565, 2004.
- [41] C. Chang, "Multifunctional Carbon-Polymer Composites for Temperature Sensing and De-Icing," University of Houston, Houston, 2013.
- [42] A. Maheri, "Utilising Implanted Carbon Fibre as a Resistive Heating Element in Wind

- Turbine Blade Anti-Icing Systems," *Wessex Institute of Technology Transactions on Engineering Sciences*, vol. 77, no. Materials Characterisation VI, pp. 297-308, 2013.
- [43] W. M. Alvino, "Ultraviolet Stability of Polyimides and Polyamide-imides," *Applied Polymer Science*, vol. 15, no. 9, pp. 2123-2140, 1971.
- [44] N. Huonnic, M. Abdelghani, P. Mertiny and A. McDonald, "Deposition and characterization of flame-sprayed aluminum on cured glass and basalt fiber-reinforced epoxy tubes," *Surface & Coating Technology*, vol. 205, pp. 867-873, 2010.
- [45] A. Lopera-Valle and A. McDonald, "Application of Flame-Sprayed Coatings as Heating Elements for Polymer-Based Composite Structures," *Journal of Thermal Spray Technology*, vol. 24, no. 7, pp. 1289-1301, 2015.
- [46] A. Lopera-Valle and A. McDonald, "Flame-sprayed coatings as de-icing elements for fiber-reinforced polymer composite structures: Modeling and experimentation," *International Journal of Heat and Mass Transfer*, vol. 97, pp. 56-65, 2016.
- [47] B. Rooks, "Robot spraying of helicopter rotor blade ice protection system," *Industrial Robot: An International Journal*, vol. 28, no. 4, pp. 313-317, 2001.
- [48] W. Zhao, M. Li, Z. Zhang and H. Peng, "Carbon Nanotube Based Composite Film Heater for De-Icing Application," in *14th European Conference on Composite Materials*, Budapest, 2010.
- [49] C. Barone, D. Imperato, S. Pagano, L. Vertuccio, A. Sorrentino and H. C. Neitzert, "Electrical Noise Characterization of Epoxy/MWCNT Composites," in *Sensors and Microsystems*, Springer Science+Business Media, 2011, pp. 49-53.

- [50] C. Barone, S. Pagano and H. C. Neitzert , "Transport and Noise Spectroscopy of MWCNT/HDPE Composites with Different Nanotube Concentrations," *Journal of Applied Physics*, vol. 110, p. 113716, 2011.
- [51] H. C. Neitzert and G. Landi, "Influence of the Contact Metallization on the Characteristics of Resistive Temperature Sensors Based on EPOXY/MWCNT Composites," in *Sensors*, Springer International Publishing Switzerland, 2015, pp. 333-337.
- [52] Y. A. Çengel and A. J. Ghajar, *Heat and Mass Transfer*, McGraw Hill Education, 2015.
- [53] M. Mohseni, "Development of a Novel Electro-thermal Anti-icing System for Fiber-reinforced Polymer Composite Airfoils," University of Alberta, Edmonton, 2012.
- [54] O. Gohardani, M. C. Elola and C. Elizetxea, "Potential and prospective implementation of carbon nanotubes on next generation aircraft and space vehicles: A review of current and expected applications in aerospace sciences," *Progress in Aerospace Sciences*, vol. 70, pp. 42-68, 2014.
- [55] S. T. Buschhorn, N. Lachman, J. Gavin, B. L. Wardle, S. S. Kessler and G. Thomas, "Electrothermal Icing Protection of Aerosurfaces Using Conductive Polymer Nanocomposites," in *54th AIAA/ASME/ASCE/AHS/ASC Structures, Structural Dynamics, and Materials Conference*, Boston, 2013.
- [56] S. S. Wicks, R. G. de Villoria, B. L. Wardle, S. S. Kessler and C. T. Dunn, "Carbon Nanotube (CNT) Enhancements for Aerosurface State Awareness," in *Proceedings of the Eighth International Workshop on Structural Health Monitoring*, Stanford, 2011.
- [57] R. A. Watson, G. A. Fielding, D. V. Cunningham and C. D. Starr, "Electrical Resistance Alloys," in *ASM Handbook, Volume 2, Properties and Selection: Nonferrous Alloys and*

Special-Purpose Materials, ASM International, 1990, pp. 822-839.

- [58] D. Vennerberg and M. R. Kessler, "Anisotropic buckypaper through shear-induced mechanical alignment of carbon nanotubes in water," *Carbon*, vol. 80, pp. 433-439, 2014.
- [59] M.-F. Yu, B. S. Files, S. Arepalli and R. S. Ruoff, "Tensile Loading of Ropes of Single Wall Carbon Nanotubes and their Mechanical Properties," *Physical Review Letters*, vol. 84, no. 24, pp. 5552-5555, 2000.
- [60] A. Laroche, A. Dolatabadi and S. V. Hoa, "Low-Cost Electrothermal Icing Protection System for Composite Materials," in *Canadian Society of Mechanical Engineers*, Kelowna, 2016.
- [61] A. Laroche, A. Dolatabadi and S. V. Hoa, "Icing Protection System for Composite Structures Using Carbon Fiber Heating Elements," in *American Society for Composites Thirty-First Technical Conference*, Williamsburg, 2016.
- [62] Resolution Performance Products LLC, "Epikote Resin 862/ Epikure Curing Agent W System," Resolution Performance Products LLC, USA, 2001.
- [63] D. C. De Pauw, "Effect of a Superhydrophobic Coating on the Anti-Icing and De-Icing of an Airfoil," Delft University of Technology, Delft, 2013.
- [64] Celestron, "Handheld Digital Microscope Pro - Instruction Manual Model #44308," Celestron, Torrance, 2013.
- [65] Logitech, "Specifications," 2017. [Online]. Available: http://support.logitech.com/en_ca/product/hd-pro-webcam-c920/specs. [Accessed 23 May 2017].

- [66] NanoTechLabs Inc., "High Conductivity MWNT Blend Buckypaper 12" X 12" 60 GSM," Edge, 2012. [Online]. Available: [http://www.nanotechlabs.com/MWNT Blend Buckypaper 12 x 12 60gsm.html](http://www.nanotechlabs.com/MWNT%20Blend%20Buckypaper%2012%20x%2012%2060gsm.html). [Accessed 24 June 2017].
- [67] CST - The Composites Store Inc., "Carbon Fiber Tows," [Online]. Available: http://www.cstsales.com/carbon_tow.html. [Accessed 24 June 2017].
- [68] OMEGA Engineering Inc., "Fine Diameter Thermocouple Wire," 2017. [Online]. Available: <http://www.omega.com/pptst/SPIR.html#nav>. [Accessed 24 June 2017].
- [69] Y. Cao and K. Chen, "Helicopter Icing," *The Aeronautical Journal*, vol. 13, no. 1152, 2010.
- [70] N. Athanasopoulos, D. Sikoutris, T. Panidis and V. Kostopoulos, "Numerical investigation and experimental verification of the Joule heating effect of polyacrylonitrile-based carbon fiber tows under high vacuum conditions," *Journal of Composite Materials*, vol. 46, no. 18, pp. 2153-2165, 2011.
- [71] P. Suke, "Analysis of Heating Systems to Mitigate Ice Accretions on Wind Turbine Blades," McMaster University, Hamilton, 2014.
- [72] D. B. Cox and M. Schuyler, "Strain-Resistant Heated Helicopter Rotor Blade". United States Patent 4,841,124, 20 June 1989.
- [73] B. G. Falzon, P. Robinson, S. Frenz and B. Gilbert, "Development and Evaluation of a Novel Integrated Anti-Icing/De-Icing Technology for Carbon Fibre Composite Aerostructures using an Electro-Conductive Textile," *Composites: Part A*, vol. 68, pp. 323-335, 2015.

- [74] N. Athanasopoulos and V. Kostopoulos, "Resistive Heating of Multidirectional and Unidirectional Dry Carbon Fiber Preforms," *Composites Science and Technology*, vol. 72, pp. 1273-1282, 2012.
- [75] R. Chugh and D. Chung, "Flexible Graphite as a Heating Element," *Carbon*, vol. 40, pp. 2285-2289, 2002.
- [76] V. Volman, Y. Zhu, A.-R. O. Raji, B. Genorio, W. Lu, C. Xiang, C. Kittrell and J. M. Tour, "Radio-Frequency-Transparent, Electrically Conductive Graphene Nanoribbon Thin Films as Deicing Heating Layers," *Applied Materials and Interfaces*, vol. 6, pp. 298-304, 2013.
- [77] F. De Rosa, "Electrically Heated Composite Leading Edges for Aircraft Anti-Icing Applications," University of Naples Federico II, Naples, 2010.
- [78] H. Chu, Z. Zhang, Y. Liu and J. Leng, "Self-Heating Fiber Reinforced Polymer Composite Using Meso/Macropore Carbon Nanotube Paper and its Application in Deicing," *Carbon*, vol. 66, pp. 154-163, 2014.
- [79] A. Fosbury, S. Wang, Y. F. Pin and D. Chung, "The Interlaminar Interface of a Carbon Fiber Polymer-Matrix Composite as a Resistance Heating Element," *Composites: Part A*, vol. 34, pp. 933-940, 2003.